This is to certify that the

dissertation entitled

The Effect of Columnar Defects on the Vortex Melting Transition in $YBa_2Cu_3O_{7-\delta}$

presented by

Robert James Olsson

has been accepted towards fulfillment
of the requirements for

Ph.D. degree in Physics

Major professor

Date 5/5/2000

The Effec

The Effect of Columnar Defects on the Vortex Melting Transition in $YBa_2Cu_3O_{7-\delta}$

By

Robert James Olsson

A DISSERTATION

Submitted to
Michigan State University
in partial fulfillment of the requirements
for the degree of

DOCTOR OF PHILOSOPHY

Department of Physics and Astronomy

2000

The Effect

The

crystals is i

crystals. A

confirmed i

critical poir

melting tra

irradiation

results in a

samples.

a continuo

fluctuation

non-ohmic

The evolut

investigate

like defects

point a Bos

crystals. W

ABSTRACT

The Effect of Columnar Defects on the Vortex Melting Transition in $YBa_2Cu_3O_{7-\delta}$

By

Robert James Olsson

The vortex melting transition in high quality, untwinned $YBa_2Cu_3O_{7-\delta}$ single crystals is investigated in the presence of columnar defect tracks imbedded in the crystals. A first order melting transition from a vortex lattice to liquid has been confirmed in clean samples, with the melting line ending at an upper and lower critical point, beyond which a continuous transition is presumed. In this work the melting transition and associated critical points are altered by the controlled irradiation of the samples by high energy uranium and lead ions. The irradiation results in a random distribution of straight, continuous defect tracks in the samples. For high defect densities the first order melting transition is replaced by a continuous Bose glass phase transition. The transition is described by a critical fluctuation regime. Current-voltage measurements were obtained within this non-ohmic regime, and successfully scaled according to the Bose glass model. The evolution of the melting from a first order to continuous transition is investigated by the introduction of low densities of columnar defects and point-like defects created by proton irradiation. At low magnetic fields below the critical point a Bose glass transition is confirmed from the data from the columnar defect crystals. With increasing field the lower critical point is crossed and the vortex

lattice is re

solid-to-ord

from the pr

increasing

columnar d

suggests th

resulting in

induce wan

lattice is reestablished. Thus, this implies the possible existence of a disordered solid-to-ordered vortex lattice phase transition within the solid state. The data from the proton irradiation shows a decrease in the upper critical field with increasing point disorder, whereas the opposite is found in a crystal with columnar defects, irradiated at a dose matching field of 1000 Gauss. This suggests that columnar defects tend to restrain the meandering of vortices resulting in a higher upper critical point, whereas the point defect pinning sites induce wandering and possible vortex entanglement.

This thesis

This thesis is lovingly dedicated to Kristy Olsson. Thanks! Without your help and strength, this work would never have been completed.

The

profession

National S

Supercond

through th

This work i

taught me

colleagues

Mazilu, Go

Reginald R

Michigan S

Stump, and

position of

constant su

Alan Meltze

ACKNOWLEDGMENTS

There are many who have been helpful, directly and indirectly, in my professional development. The funding for my research was provided by the National Science Foundation Science and Technology Center for Superconductivity, under contract #DMR91-20000, and also from Harold Myron through the Division of Educational Programs at Argonne National Laboratory. This work is a continuation of the overall work of Wai-Kwong Kwok, who has taught me a level of thoroughness I had not previously known. The other major colleagues in this effort are Lisa Paulius and Andra Petrean, with help from Ana Mazilu, Goran Karapetrov, Valentina Tobos, David Hofman, Bruce Glagola, Reginald Ronningen, and George Crabtree. Thanks to my committee at Michigan State University: Simon Billinge, Mark Dykman, Wayne Repko, Daniel Stump, and especially to Phillip Duxbury, who was kind enough to take on the position of major advisor. Thanks also to the Argonne Soccer Club, for their constant support. Finally, a special thanks to Jerry Cowen (posthumously) and Alan Meltzer, *for noticing.*

TABLE OF CONTENTS

Table 5.1

Table 7.1

LIST OF TABLES

LIST OF FIGURES

In th

there is a w

and solids.

field, known

associated

of a crystal

present. Fu

ice-like melt

Vortic

The density

They can be

They may be

even be drive

Although vor

in the absenc

by freezing th

environment

may even be

number of exp

atomic solids.

Chapter 1

INTRODUCTION

In the magnetic phase diagram of high temperature superconductors, there is a wide field and temperature regime in which there exists novel liquids and solids, consisting entirely of magnetic field lines. These lines of magnetic field, known as flux lines or vortices, possess many of the characteristics associated with normal matter. Like solids, these flux lines can acquire the form of a crystal with a lattice structure, or form a disordered glass when defects are present. Furthermore at high temperatures the vortices are even capable of an ice-like melting transition to a vortex liquid state.

Vortices interact with the environment in a number of controllable ways. The density of vortices can be varied by an external applied magnetic field. They can be localized or 'pinned' in place by defects in the underlying crystal. They may be thermally set in motion about their equilibrium position by heat, and even be driven to move in a preferential direction by an applied current. Although vortices freeze via a first order transition from a liquid to a lattice state in the absence of disorder, several novel vortex glassy phases can be obtained by freezing the vortex liquid in a variety of defect environments. The environment may be a random set of weak/strong point defects, line defects, or may even be a periodic defect array. Thus *vortex matter* can be studied in a number of experimentally controllable ways which may not all be possible in atomic solids. One such problem in atomic solids is the transformation of a first

order trans

disorder.

systems, h

in introduci

study of vo

provide a p

transitions.

The

of the first o

crystals in th

observed to

order melting

critical point,

evolution of t

respect to the

heavy ion irra

First, t

vortex melting

phase is found

and the critica

glass and a la

from a first ord

line defects wi

order transition into a second order or continuous transition in the presence of disorder. This problem has theoretically been studied extensively in magnetic systems, however, related experiments have been hampered due to the difficulty in introducing quenched disorder into the system in a controlled way. Thus, the study of vortex matter can be a powerful tool for the study of real matter, and also provide a platform to investigate fundamental problems in the physics of phase transitions.

The focus of this thesis is on the fundamental issue of the transformation of the first order vortex melting transition in superconducting $YBa_2Cu_3O_{7-\delta}$ crystals in the presence of disorder. In the absence of disorder, this transition is observed to be first order, as in the case of very high quality samples. The first order melting transition line terminates at both ends at an upper and a lower critical point, whereby the transition becomes continuous in nature. The evolution of the first order solid to liquid vortex transition will be investigated with respect to the introduction of line defects into the superconductor via high energy heavy ion irradiation.

First, the case for a high density of defects will be studied, where the vortex melting transition is continuous at all investigated fields, and the solid phase is found to be a disordered glassy state. Second, the melting transition and the critical points are studied in the dilute line defect limit. Here both a vortex glass and a lattice state are observed, and a defect density-dependent evolution from a first order to a continuous melting transition is found. Finally, results from line defects will be compared with results from point defects. Hopefully this work

will shed l

of phase t

The

framework

transition c

growth and

samples. T

of both high

phase trans

with that of p

line in the vc

will shed light not only on vortex physics, but also aid in a broader understanding of phase transitions.

The first part of this thesis provides a theoretical and experimental framework of the physics of vortex matter, focusing especially on the melting transition observed in $YBa_2Cu_3O_{7-\delta}$. The second part describes the crystal growth and preparation processes and the details of line defect creation in these samples. The main part of the thesis details the melting transition as a function of both high and low densities of line defects and analyzes each of the novel phase transition lines and their evolution. The final section compares the results with that of point defects and proposes the existence of a new phase transition line in the vortex solid.

2.1 Intro

The phenc

Onnes in 1

observed a

properties c

From meas

constant wa

essentially

supercondu

from the sa

Meissner e

observed ir

supercondu

external fie

zero by set

applied fiel

a magnetic

becomes g

normal sta

energy H_c^2

Chapter 2

VORTEX STATES

2.1 Introduction to superconductivity

The phenomenon of superconductivity was discovered by H. Kammerlingh Onnes in 1911[1] in mercury, in which a sudden drop to zero resistivity was observed at a critical transition temperature T_c = 4.1 K. In order to gauge the properties of this state, a persistent current was set up in a superconducting ring. From measurements of the field induced by this current, the current decay time constant was extrapolated to be greater than 100,000 years, thus establishing essentially lossless current flow in the ring. It was later recognized that the superconducting state is also characterized by the expulsion of magnetic field from the sample, a phenomena akin to perfect diamagnetism, called the Meissner effect[2]. This phenomena of diamagnetism in superconductors is observed in magnetization measurements at temperatures below the superconducting transition temperature, as shown in Figure 2.1(a). As an external field H is applied, the superconducting material keeps the internal field at zero by setting up a diamagetic field with a circulating current to offset the applied field. Thus there is negative bulk magnetization. Upon the application of a magnetic field above a critical field H_c, the energy necessary to expel the field becomes greater than the condensation energy, and the sample returns to the normal state. The shaded region in Figure 2.1(a) is equal to the condensation energy $H_c^2 / 8\pi$, which represents the lower energy of the superconducting state

(a) Magnetization curve for type I superconductor

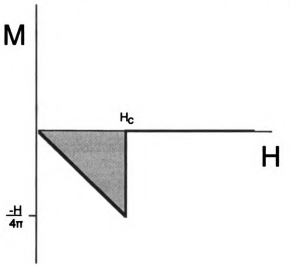

(b) Phase diagram for type I superconductor

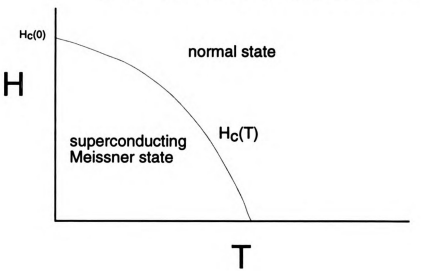

Figure 2.1 Type I superconductors.

as compa

and repres

field at zer

the norma

at $T = 0$ an

The

established

thin layer fr

supercondu

maximum c

results are

where E is

local magn

nonzero m

density (eq

a change i

Mat

normal sta

supercond

intermedia

as compared to the normal state. The critical field is temperature dependent, and represented empirically by $H_c=H_c(0)\cdot(1-(T/T_c)^2)$, where $H_c(0)$ is the critical field at zero temperature, as shown in Figure 2.1(b). In type I superconductors, the normal to superconducting state transition is of first order everywhere except at $T = 0$ and $T = T_C(H=0)$, where the transition is continuous.

The zero magnetic field within the bulk of the superconductor is established by a counterflowing circulating supercurrent j_s, which flows within a thin layer from the surface, producing a magnetic field which shields the superconductor from the applied field. Thus a critical field is equivalent to a maximum critical current j_c, beyond which the sample is driven normal. These results are described within the two London equations for superconductivity[3]:

$$E = \frac{4\pi\lambda^2}{c^2}\frac{\partial}{\partial t}(j_s) \tag{2.1}$$

$$h = -\frac{4\pi\lambda^2}{c}\nabla\times(j_s) \tag{2.2}$$

where E is the electric field induced by the superconducting current j_s, h is the local magnetic field, λ is the field penetration depth and c is the speed of light. A nonzero magnetic field exists only where there is a gradient in the supercurrent density (eqn. (2.2)), and an electric field (and thus loss) exists only where there is a change in the supercurrent density in time (eqn. (2.1)).

Materials that display a single transition from the diamagnetic to the normal state are known as type I superconductors. However, most commercial superconductors used today are type II superconductors, which have an intermediate mixed state distinguished by the absence of total flux expulsion, as

shown by

usually ch

critical fie

penetrates

containing

described a

supercondu

maximum a

core the ma

from the co

Vorti

supercurrer

Abrikosov v

theoretically

for close to

$a = (\Phi_o / B)$

via ferroma

scanning tu

vortices inc

the normal

conventiona

For p

usually betv

shown by the magnetization curve in Figure 2.2(a). Type II superconductors are usually characterized by a low field Meissner state which terminates at a lower critical field H_{c1}, and by an intermediate or mixed state where the magnetic field penetrates the superconductor in tubes of quantized flux known as vortices, each containing one flux quantum Φ_0. The vortices (Figure 2.3(a)) can be qualitatively described as containing a core region of radius ξ, where the density of superconducting quasiparticles is zero at the center and increases sharply to a maximum across the distance ξ described as a coherence length. Within the core the magnetic field is at its maximum value and decays over a distance λ from the core center.

Vortices repel one another via the Lorentz interaction between the supercurrents and the extended field, forming a lattice structure known as the Abrikosov vortex lattice (Figure 2.3(b)), named after Alexei Abrikosov, who theoretically predicted its existence in Type II superconductors in 1957. Except for close to H_{c1} the intervortex spacing a can be approximately given by $a = (\Phi_o / B)^{1/2}$, with $B \approx H$. This triangular lattice configuration has been observed via ferromagnetic filament surface decoration[4], neutron diffraction[5], and scanning tunneling microscopy[6]. As the applied field is increased the density of vortices increases, until overlap of the normal core drives the superconductor into the normal state at an upper critical field H_{c2}. The phase diagram for conventional type II superconductors is shown in Figure 2.2(b).

For pure type I superconductors, $H_c(0)$ and T_c are quite low, with $H_c(0)$ usually between 200 – 800 Gauss, and T_c < 10 K, resulting in a rather small

(a) Magnetization curve for a type II superconductor

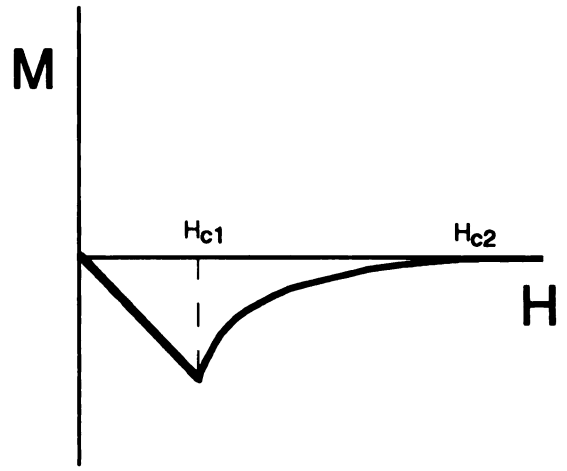

(b) Phase diagram for a type II superconductor

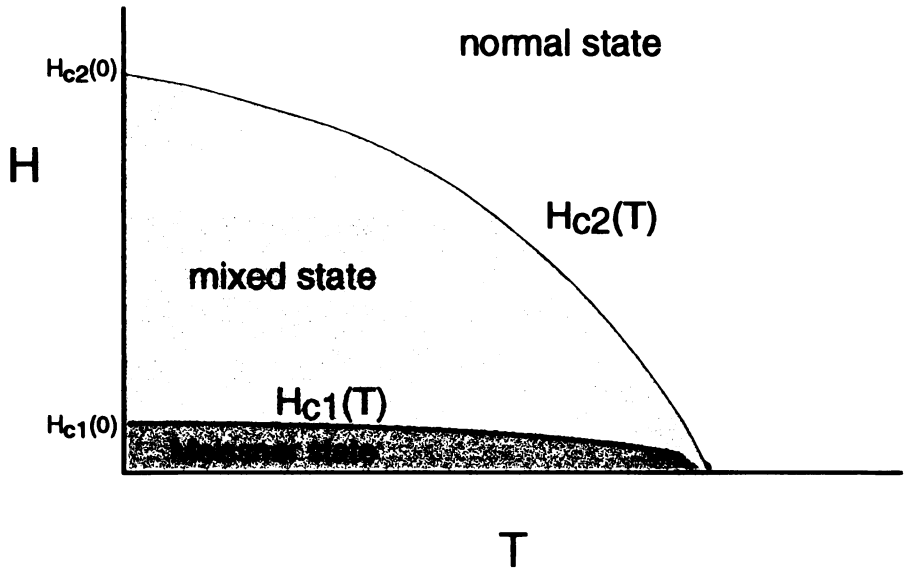

Figure 2.2 Type II superconductors.

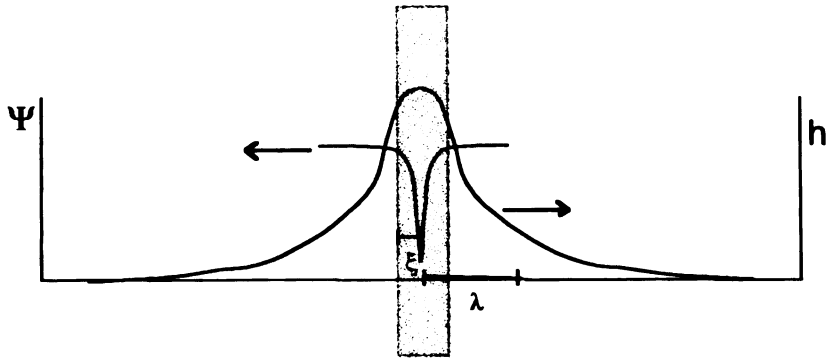

Vortex line, with nonsuperconducting core, radius ξ

(a) Profiles of the field and order parameter of a vortex line.

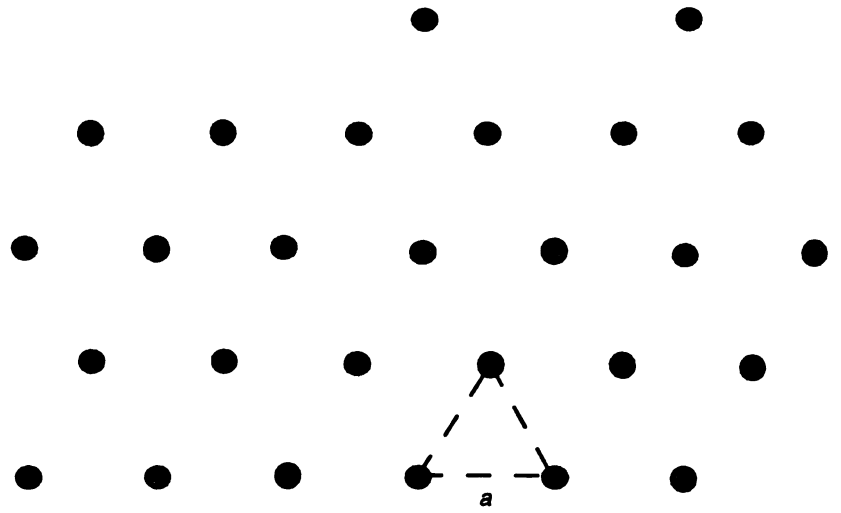

triangular vortex lattice, spacing $a = \left(\frac{\Phi_0}{B}\right)^{1/2}$

(b) Vortices forming a vortex lattice solid state. View is along the vortex lines.

Figure 2.3 Vortex lines.

supercon

much hig

material u

approxima

superconc

useful for p

2.2 Ginz

The superc

h, can be d

theory of se

of the syste

transition te

order param

parameter is

electrons, n

free energy

Where F_s is

magnetic fie

phenomenol

equation with

the above eq

superconducting phase space. On the other hand, type II superconductors have much higher upper critical fields $H_{c2}(0)$. For Nb_3Ti wire, a low temperature type II material used in windings of superconducting magnets, T_c is ~9.7 K, but $H_{c2}(0)$ is approximately 100,000 Gauss (10 Tesla). Correspondingly, type II superconductors exhibit significantly higher critical currents, thus making them useful for practical applications.

2.2 Ginzburg-Landau theory

The superconducting transition, in the presence of a local magnetic field density h, can be described by the phenomenological Ginzburg-Landau theory[7]. This theory of second-order phase transitions describes a gradual change in the state of the system followed by a discontinuity in the symmetry of the system at the transition temperature. It describes the process by using an expansion of an order parameter near the transition temperature. For superconductors, the order parameter is a wavefunction ψ defined by the local density of superconducting electrons, $n_s = |\psi|^2$ which exists below the transition temperature at $T < T_c$. The free energy density in the presence of zero field is given by

$$F_s = F_n + \alpha|\Psi|^2 + \frac{\beta}{2}|\Psi|^4 \qquad (2.3)$$

Where F_s is the free energy density of the superconductor in the absence of a magnetic field, F_n is its free energy in the normal state and α and β are phenomenological material dependent expansion coefficients. Minimizing the equation with respect to $|\psi|^2$ yields $|\psi|^2 = -\alpha/\beta$. Substituting this expression into the above equation yields $F_n - F_s = \alpha^2/2\beta \equiv H_c^2/8\pi$, establishing a lower free

energy in

given by

the transi

α β that

positive a

temperatu

$(T/T_c)^2$) ne

For

field, the G

$$G_{}$$

where the fo

e* moving in

of the Coope

is the applie

variations of

$$\frac{}{4}$$

The first differ

superconduct

evaluating (2.

Ψ varies:

energy in the superconducting state than in the normal state, with the difference given by the condensation energy. Since the order parameter must be zero at the transition temperature $T = T_c$ and nonzero below T_c, it follows from $|\psi|^2 = -\alpha/\beta$ that $\alpha(T = T_c) = 0$ and $\alpha(T < T_c) < 0$. Thus to first order, $\alpha \sim (T-T_c)$ and β is positive and temperature independent. Furthermore, since $H_c^2 = 4\pi\alpha^2/\beta$, the temperature dependence of α correlates with the empirical formula $H_c^2=H_c(0)(1-(T/T_c)^2)$ near T_c.

For an inhomogeneous superconductor in a uniform external magnetic field, the Gibbs free energy near T_c can be written as:

$$G_s = G_n + \alpha|\psi|^2 + \frac{\beta}{2}|\psi|^4 + \frac{1}{2m^*}\left|\left(\frac{\hbar}{i}\nabla - \frac{e^*}{c}\mathrm{A}\right)\psi\right|^2 + \frac{h^2}{8\pi} - \frac{h\cdot H_0}{4\pi} \qquad (2.4)$$

where the fourth term describes the kinetic energy density for a particle of charge e^* moving in the field with a vector potential $\mathbf{A}$, m^* is the superconducting mass of the Cooper pair (charge 2e), G_n is the normal state Gibbs free energy, and H_o is the applied external magnetic field. Evaluation of eqn. (2.4) with respect to variations of ψ, ψ^*, and $\mathbf{A}$, yields the Ginzburg-Landau differential equations:

$$\alpha\psi + \beta|\psi|^2\psi + \frac{1}{2m^*}\left(\frac{\hbar}{i}\nabla - \frac{e^*}{c}\mathbf{A}\right)^2\psi = 0 \qquad (2.5)$$

$$\frac{c}{4\pi}\nabla\times\mathbf{h} = \frac{e^*\hbar}{2m^*c}(\psi^*\nabla\psi - \psi\nabla\psi^*) - \frac{e^{*2}}{m^*c}\psi^*\psi\mathbf{A} = \mathbf{J} \qquad (2.6)$$

The first differential equation provides the first characteristic length scale for superconductors: the coherence length ξ. The coherence length is obtained by evaluating (2.5) in zero field, and provides a measure of the length over which ψ varies:

The cons

made clea

imaginary

equation b

This is the

little variatio

along the ve

a simple bou

choosing the

where λ des

penetration

Eqns. (2.8) a

shows that o

as given by (

Note that sinc

$T \to T_c$. Final

the Ginzburg-

$$\xi^2 = \frac{\hbar^2}{2m^*|\alpha(T)|} \tag{2.7}$$

The consequences of the second Ginzburg-Landau differential equation can be made clear by the substitution of $\psi(\mathbf{r}) = |\psi(\mathbf{r})|e^{i\varphi(\mathbf{r})}$, thus separating the real and imaginary parts of the order parameter. With this substitution in (2.6), the equation becomes

$$\mathbf{J} = \frac{e^*}{m^*}|\psi|^2\left(\hbar\nabla\varphi - \frac{e^*}{c}\mathbf{A}\right) \tag{2.8}$$

This is the equation for the supercurrent density. Within a region where φ has little variation, the supercurrent density J is then proportional to, and directed along the vector potential $\mathbf{A}$, i.e. perpendicular to the field direction. By applying a simple boundary condition for a superconducting boundary (J=0 across), and choosing the London gauge as $\nabla \cdot \mathbf{A} = 0$, then eqn. (2.8) can be rewritten as

$$\nabla^2\mathbf{A} + \frac{\mathbf{A}}{\lambda} = 0 \tag{2.9}$$

where λ describes the penetration depth of the vector potential, and thus the field penetration length:

$$\lambda^2 = \frac{m^*c^2}{4\pi|\psi|^2 e^{*2}} \tag{2.10}$$

Eqns. (2.8) and (2.9) can be used to describe the Meissner effect: Eqn. (2.9) shows that over a characteristic length λ, the field is screened by supercurrents as given by (2.8), beyond which the material superconducts in a zero field state. Note that since both λ^2 and ξ^2 are proportional to $1/|\alpha|$, they both diverge as $T \rightarrow T_c$. Finally, one other important parameter in evaluating superconductors is the Ginzburg-Landau parameter κ:

It is the m

type I or t

The

considerin

I supercon

minimum s

for type I su

as $(H_c^2/8\pi$

material sup

depth (Meis

extends bey

surface is ne

to maximize

the magnetic

possible tota

The G

and provides

an applied fie

consideration

$$\kappa = \frac{\lambda}{\xi} \tag{2.11}$$

It is the magnitude of this parameter which defines a material as being either a type I or type II superconductor.

The criterion for a type I versus a type II superconductor is established by considering an interface between normal and superconducting regions. For type I superconductors, the total energy of the boundary is positive, so that a minimum surface area is the energetically favorable condition. This is because, for type I superconductors, $\lambda < \xi$. Since the surface energy can be approximated as $(H_c^2/8\pi)(\xi - \lambda)$, this results in a positive surface energy. Thus the bulk of the material superconducts, with no internal magnetic field beyond the penetration depth (Meissner state). For type II superconductors the penetration length extends beyond the coherence length. In this case the energy of the boundary surface is negative, specifically for $\kappa > 1/\sqrt{2}$ [8]. Thus it is energetically favorable to maximize the total surface energy, which is accomplished by the localization of the magnetic flux into single, quantized flux lines, each equaling the lowest possible total flux, $\Phi_0 = hc/2e = 2.1 \times 10^{-11} G \cdot m^2$.

The Ginzburg-Landau theory describes the region close to the transition and provides a framework and valid predictions for the superconducting state in an applied field, including the Meissner and mixed states, from simple energy considerations.

2.3 Hi

High tem

Müller[9].

high supe

superconc

characteris

superconc

have result

conventiona

One

low T_c and

as the squa

high T_c sup

and large a

For example

H_{c2} ~ 120 T,

compared to

large differe

The h

short cohere

naturally-occ

2.3 High temperature superconductors

High temperature superconductivity was discovered in 1987 by Bednorz and Müller[9]. High temperature superconducting materials are characterized by their high superconducting temperatures, very short coherence length, and a large superconducting anisotropy owing to their layered structure. These characteristic features have led to a new understanding of type II superconductors and furthermore, with the addition of disorder into the system, have resulted in a wealth of new vortex phases which were unobservable in conventional lower temperature superconductors.

One of the characteristic parameters used in discerning the difference in low T_c and high T_c superconductors is the Ginzburg number *Gi*, which is defined as the squared ratio of the thermal energy k_BT and the condensation energy. In high T_c superconductors, the high transition temperature, small coherence length and large anisotropy leads to a large Ginzburg number *Gi*

$$Gi = \frac{1}{8}\left[\frac{\gamma T_c}{H_{c2}^2(0)\kappa^2\xi^3(0)}\right]^2 \tag{2.12}$$

For example, for $YBa_2Cu_3O_{7-\delta}$ (YBCO) with H || c, $T_c \sim 90$ K, $\xi \sim 16$ Å, $H_{c2} \sim 120$ T, $\gamma \sim 7$, and $\kappa \sim 60$, yielding a Ginzburg number of $Gi \approx 10^{-2}$ compared to $Gi \sim 10^{-8}$ for conventional low temperature superconductors. This large difference leads to many novel phenomena.

The higher temperatures result in large thermal fluctuations, while the very short coherence length dramatically reduces the effective pinning strength of naturally-occurring defects. The large anisotropy weakens the correlation of the

vortex alc

effective r

This paran

superconc

$\xi_c \approx 2$ Å a

line is stron

most circun

anisotropy

behave mor

In va

energy, the

compete in v

vortex syste

laboratory.

energy can b

careful introd

force to depi

transport curr

Figure

resistivity in th

vortex along the length of the line. The anisotropy parameter γ, is defined by the effective mass ratio m_c/m_{ab}

$$\gamma = \left(\frac{m_c}{m_{ab}}\right)^{1/2} = \frac{\lambda_c}{\lambda_{ab}} = \frac{\xi_{ab}}{\xi_c} \tag{2.13}$$

This parameter is a reflection of the planar structure of the high temperature superconductors. For YBCO ($\kappa \approx 60$), $\lambda_{ab}(0) \approx 1000$ Å, $\xi_{ab} \approx 16$ Å, $\gamma \sim 7$, and $\xi_c \approx 2$ Å and $\lambda_c(0) \approx 7000$ Å. For this material, the correlation along the vortex line is strong enough to still be considered a three-dimensional elastic line in most circumstances; however for $Bi_2Sr_2CaCu_2O_8$ (BSCCO), due to its extreme anisotropy $\gamma \sim 150$, the c-axis vortex correlation is very weak, making the vortices behave more like 2 dimensional objects, called pancake vortices.

In various parts of the phase diagram, the vortex-vortex interaction energy, the thermal energy, and the pinning energy can be comparable and compete in ways to produce new transitions and phases. One advantage of the vortex system is that all the relevant parameters can be carefully controlled in the laboratory. The vortex density can be varied by the magnetic field, the thermal energy can be varied with temperature, the pinning energy can be varied by careful introduction of pinning sites via irradiation, and furthermore, the driving force to depin the vortices from the pinning sites can be controlled with the transport current.

Figure 2.4 presents a comparison of the temperature dependence of the resistivity in the superconducting state for a Nb_3Ti wire and an untwinned YBCO

(a) Resista

2

1

R (mΩ)

1

5

0

(b) Re
crystal

6

5

ρ (μΩ-cm)

4

3

2

1

0

Fi
Su
Su

(a) Resistance vs. temperature for low temperature type II superconductor.

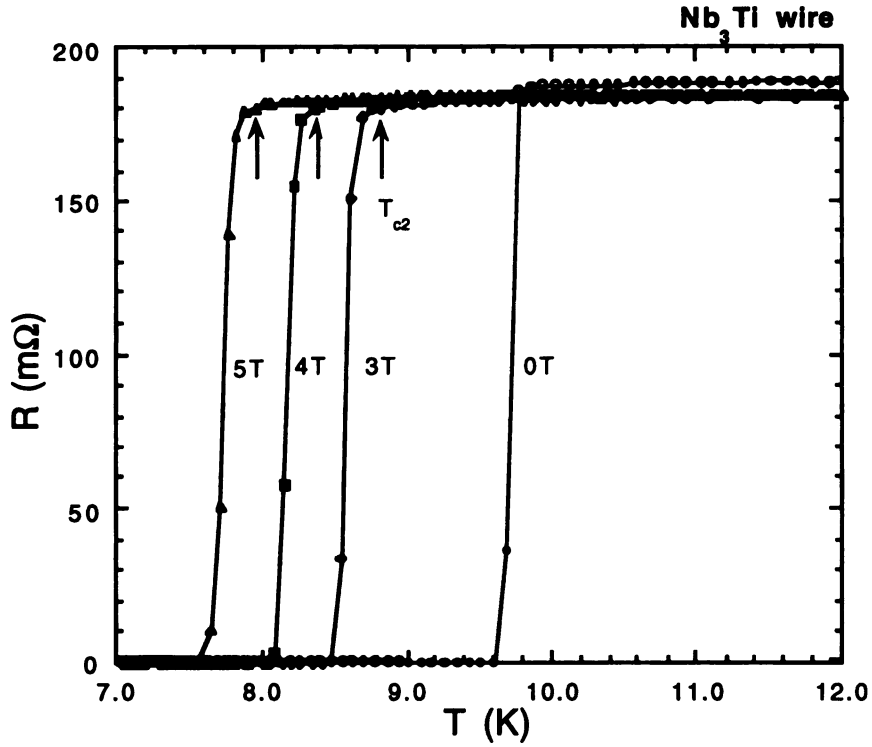

(b) Resistivity vs. temperature for high temperature type II YBCO crystal. The kink in the resistivity is marked by the arrow.

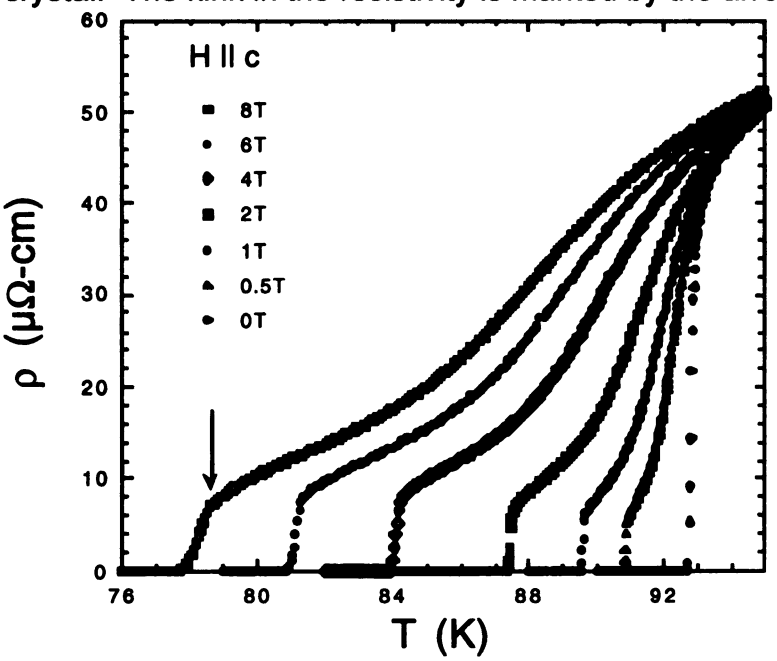

Figure 2.4 Resistivity measurements of the normal to superconducting state transition of low and high T_C superconductors in various magnetic fields.

crystal at various applied magnetic fields. While both are type II superconductors, the behavior is dramatically different. In Nb_3Ti, a sharp transition is seen at T_{c2}, which corresponds to the upper critical field H_{c2}, marked by a sharp drop in resistivity to zero. For YBCO, the transition at T_{c2} is characterized by a broadening of the resistive transition with increasing applied field, with a large temperature span between the onset of superconductivity where the resistivity initially drops and the zero resistivity temperature. For a high quality, relatively defect free YBCO crystal as the one represented here, a sharp drop in the resistivity is observed near the zero resistivity temperature. This sudden drop or 'kink' in resistivity is a new feature associated with some high temperature superconductors and reflects a vortex phase transition from a vortex liquid state to a vortex solid state with lowering temperatures. It is observed in high temperature superconductors due to their large characteristic superconducting critical temperature and large Ginzburg number which promotes the 'melting' of the vortex lattice, leading to the existence of a vortex liquid state over a large portion of the phase diagram. The vortex liquid state is sandwiched between the upper critical field line $H_{c2}(T)$ and the vortex lattice melting line $H_m(T)$. In conventional low temperature type II superconductors, $H_m(T)$ is believed to be very close to H_{c2} and thus experimentally very difficult to discern[10].

3.1 Lorentz

Although supe

is not the case

presence of a

force is induce

where **n** is the

result, the vort

electric field le

the motion of v

vortices. For e

the sample wh

case, the vorte

its condensatio

unseat or 'depi

referred to as a

wires and mag

resistance, effe

vortex motion.

or even mecha

Chapter 3

VORTEX MOTION AND VORTEX PINNING

3.1 Lorentz force and dissipation

Although superconductivity is usually associated with the loss of resistance, this is not the case in the vortex state of defect free type II superconductors. In the presence of a transport current and a perpendicular magnetic field, a Lorentz force is induced on the vortices given by:

$$\mathbf{f_L} = \boldsymbol{J} \times \mathbf{n}\, \Phi_o / c \qquad (3.1)$$

where **n** is the unit vector in the direction of the vortices, see Figure 3.1. As a result, the vortices are set in motion by the Lorentz force, inducing a transverse electric field leading to the observation of a finite resistance. In order to prevent the motion of vortices, one needs to introduce effective defect sites to 'pin' the vortices. For example, pinning can be initiated in a small microscopic region of the sample which is non-superconducting due to a crystalline defect. In this case, the vortex core would naturally sit on the normal state defect site to lower its condensation energy, and a finite level of Lorentz force will be required to unseat or 'depin' the vortex. The applied current required to depin the vortices is referred to as a critical current j_c. Thus for applications such as superconducting wires and magnets where large amount of currents are required to flow without resistance, effective pinning sites must be fabricated into the material to prevent vortex motion. Such defects sites can be made through substitution, irradiation, or even mechanical damage inflicted upon the material.

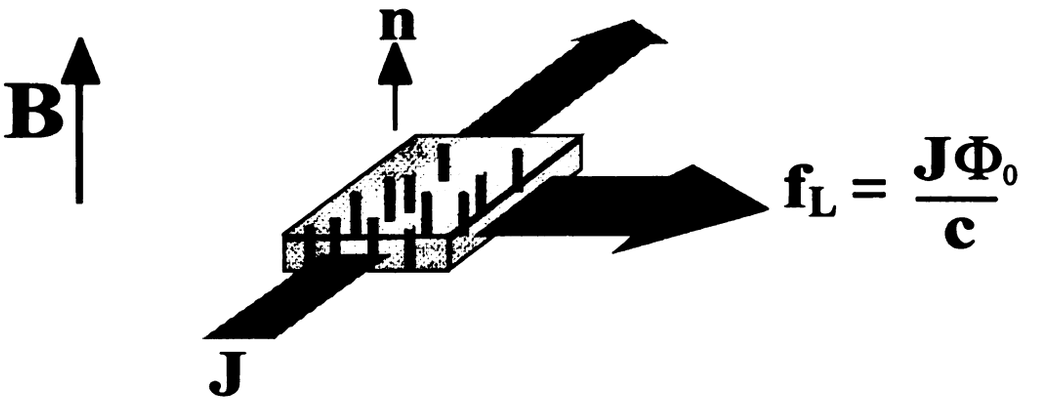

Figure 3.1 Lorentz force due to a current J applied perpendicular to the field B.

The pinning strength of a superconductor is dependent upon defects within the underlying crystal structure, and hence a perfect crystal would not be able to pin vortices. However, even the highest quality YBCO crystals yet produced contain enough 'point' defects to be able to pin the vortices. Point defects in $YBa_2Cu_3O_{7-\delta}$ are typically oxygen vacancies in the copper-oxygen chains or interstitials, usually less than 10 Å in effective radius, which act as weak pinning sites. For low defect density crystals, the vortex solid crosses from a weakly-pinned vortex lattice to an unpinned, moving vortex solid as the current density is increased beyond the critical current j_c.

Resistivity measurements represent a dynamic non-equilibrium vortex environment, and therefore cannot extract any thermodynamic quantities. However, it will be shown in later chapters that the location of different vortex thermodynamic transitions can be determined from such measurements.

3.2 Dynam

For an applie

on an isolated

where $\gamma(t)$ des

the underlying

the applied cu

$E = v \times B/c$, is

the applied cur

motion. The d

If the drag forc

then current in

state resistivity

motion of a vo

radius ξ, and

drag force is d

induced by the

$H_{c2} = \Phi_0/2\pi\xi^2$

$\rho_f \approx \rho_n B/H_{c2}$

response to th

3.2 Dynamics of vortex motion

For an applied current in the presence of a perpendicular applied field, the forces on an isolated vortex in a type II superconductor can be given by:

$$\frac{J\Phi_o}{c} - \gamma(t)v_o = 0 \tag{3.2}$$

where γ(t) describes the frictional drag force coefficient between the vortex and the underlying sample. In this simple model, the vortex velocity is proportional to the applied current density. The induced electric field, given by Faraday's law $\boldsymbol{E} = v \times \boldsymbol{B}/c$, is perpendicular to the Lorentz force but parallel to the direction of the applied current, thus generating a finite voltage drop transverse to the vortex motion. The dissipative flux flow resistivity is given by:

$$\rho_{ff} = \frac{v_o B}{Jc} = \frac{B\Phi_o}{\gamma c^2} \tag{3.3}$$

If the drag force is independent of the Lorentz force, the resultant resistivity is then current independent, i.e. ohmic. This resistivity can be related to the normal state resistivity ρ_n via the Bardeen-Stephen model[11]. In this approach, the motion of a vortex results in an electric field existing within the vortex core with radius ξ, and directed along the direction of the applied current. The resultant drag force is due to current moving within the 'normal' core. This current is induced by the electric field, with γ given by $\gamma = \Phi_o^2/(2\pi\xi^2 c^2 \rho_n)$. Since $H_{c2} = \Phi_o/2\pi\xi^2$, the Barden-Stephen model approximates the resistivity by $\rho_{ff} \approx \rho_n B/H_{c2}$. Ignoring any intervortex interactions, this model predicts an ohmic response to the applied current.

3.3 Therm

Vortices are

for the vortex

currents, the

no longer vali

regime is desc

can be repres

vortices[13].

energy barrier

The vortex mo

where the frac

densities such

model assume

$/k_BT$), where A

At low current

resistivity $\rho <<$

pinning force s

The sch

temperatures w

energy, the vort

3.3 Thermally-activated flux flow

Vortices are also affected by defects within the crystal, which act as pinning sites for the vortex lines, tending to arrest the vortex motion. For low transport currents, the Lorentz force may approach the pinning strength, and eqn. (3.2) is no longer valid since the pinning force must now be included. The low current regime is described by the thermally-activated flux flow (TAFF) model[12], which can be represented in terms of a perturbation to the flow velocity of the vortices[13]. In this model, the retardation of vortex motion is described by an energy barrier to motion U_p, which is large compared to the thermal energy $k_B T$. The vortex motion is retarded by an amount $\delta v << v$, reducing the resistivity,

$$\rho = \frac{\rho_{ff}}{1 + \frac{\delta v}{v}} \tag{3.4}$$

where the fraction $\delta v/v$ depends on the applied current density. At low current densities such that the Lorentz force is less than the pinning force, the TAFF model assumes a thermally-activated vortex motion described by $\delta v/v \approx A \exp(U_p / k_B T)$, where $A >> 1$, and eqn. (3.4) becomes

$$\rho \approx \frac{\rho_{ff}}{A} e^{-U_p / k_B T} \tag{3.5}$$

At low current densities the TAFF model predicts ohmic behavior, with a small resistivity $\rho << \rho_{ff}$. For large current densities the Lorentz force overwhelms the pinning force such that $\delta v/v \rightarrow 0$ and flux flow resistivity is recovered.

The schematic shown in Figure 3.2 describes this behavior. At high temperatures where the thermal energy is always greater than the vortex pinning energy, the vortex is in the flux flow state, and the Bardeen-Stephen model

predicts ohm

the temperat

pinning ener

TAFF flow at

Previous wor

measuremen

transition. It

a temperature

vortices are w

Figure
shows
represe
to a liq

predicts ohmic behavior, represented by a linear *E*-*J* curve with a slope of 1. As the temperature is lowered and the thermal energy becomes comparable with the pinning energy U_p, the *E*-*J* curves develops an S shape, as the flow crosses from TAFF flow at low currents to Bardeen-Stephen type flow at high currents. Previous work[14-16] has observed an S shape in current-voltage measurements, in a very narrow temperature window close to the melting transition. It has been suggested[15] that the S shape appears below the kink, in a temperature window just below the vortex melting temperature where the vortices are weakly pinned and can be easily thermally depinned, i.e. $U_p = k_B T$.

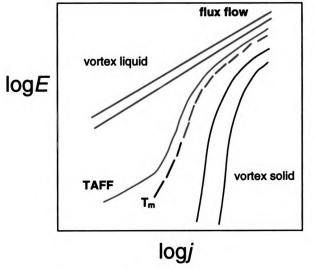

Figure 3.2 Transport measurments in YBCO. The schematic shows current-voltage behavior on a log-log plot. T_m represents a melting or crossover transition from a vortex solid to a liquid state.

3.4 Ander

Vortex motio

investigated

vortex hoppi

the Lorentz fo

is the Lorentz

of the vortex

vortices, hopp

force, the resu

In order to rel

estimated as

and the argu

current densi

Thus the theo

nonzero temp

barrier, energ

vortex motion

temperature.

temperature t

polycrystalline

the E-J curves

3.4 Anderson-Kim vortex creep model

Vortex motion for the case of strong pinning (pinning energy $U_p >> kT$) has been investigated via the flux creep model[17, 18], which describes thermally-activated vortex hopping over the pinning barriers. Again, for low enough current densities the Lorentz force is less than the pinning force, and so $U_p > U_l$, where $U_l = jBV_c r_p$ is the Lorentz force energy due to a displacement r_p, which is the pinning radius of the vortex volume. In the presence of an applied current, a net hopping of vortices, hopping rate v_0, would produce a flow in the direction of the Lorentz force, the resultant resistivity given by

$$\rho = (2v_0 B/j)e^{-U_p/kT}\sinh(jBV_c r_p/kT) \tag{3.6}$$

In order to relate the pinning energy with the critical current, the pinning energy is estimated as $U_p = U_o \cdot (1 - j/j_c)$. Thus at low current densities U_p is constant, and the argument of the hyperbolic function replaces the function, and the current density cancels out, leading to an ohmic resistivity:

$$\rho_{creep} \approx (2v_0 B^2 V_c r_p/kT)e^{-U_0/kT} \tag{3.7}$$

Thus the theory predicts a finite linear resistivity $\rho \sim e^{-U_o/kT}$ for low currents at any nonzero temperature T, due to the vortex hopping over the constant pinning barrier, energy U_o. This prediction that any Lorentz force would produce some vortex motion would imply that there is no true critical current except at zero temperature. Evidence of this vortex creep has been obtained for low temperature type II superconductors[18]. However, measurements of YBCO polycrystalline[19]and thin films[20] find no evidence of vortex creep. Instead, the *E-J* curves drop off dramatically below the transition temperature, providing

evidence tha

force. This h

measuremer

3.5 Vortex

An explanati

solid, where

applied curre

where $\mu \sim 1$ i

decreases the

a vanishingly

existence of a

resistivity at lo

evidence that the effective pinning energy *diverges* in the limit of small Lorentz force. This has also been confirmed in high resolution contactless measurements of a twinned sample[21], at temperatures further below T_m.

3.5 Vortex glass transition

An explanation for this behavior was proposed by Fisher for a disordered vortex solid, where he predicted the dependence of the effective pinning energy with the applied current to be[22]

$$U \approx U_0 e^{(j_c/j)^{\mu}} \tag{3.8}$$

where $\mu \sim 1$ is called the glassy exponent. Thus as the current density j decreases the pinning energy diverges. Assuming $\rho \sim e^{-U/kT}$, eqn. (3.8) leads to a vanishingly small resistivity at low currents and finite temperatures, and the existence of a true superconducting state, defined by the absence of linear resistivity at low currents.

THE VO

4.1 First o

One of the m
superconduct
Abrikosov latt
transition to a
recently Brézi
condensate d
of first order ju
the high temp
length ξ, and
Much theoreti
of a Lindeman
melted when t
a fraction c_L of

The brackets <
directions. The
within the vorte

Chapter 4

THE VORTEX PHASE DIAGRAM OF CLEAN $YBa_2Cu_3O_{7-\delta}$ CRYSTALS

4.1 First order vortex solid to liquid melting transition

One of the most salient characteristics of the vortex state in high temperature superconductors is the existence of a first order melting transition of the Abrikosov lattice in clean single crystals. Although a continuous freezing transition to a vortex lattice state at H_{c2} was predicted by Abrikosov, more recently Brézin, Nelson, and Thiaville have shown that when fluctuations in the condensate density are taken into account, the freezing transition at H_{c2} can be of first order just below H_{c2} in low temperature type II superconductors[23]. For the high temperature superconductors, due to their high T_c, small coherence length ξ, and large anisotropic mass ratio, the melting line can be far from H_{c2}. Much theoretical work has been conducted to investigate this transition in terms of a Lindemann criterion for melting[24], where the vortex lattice is considered melted when the mean-square vortex line thermal displacement $\langle u^2 \rangle$ is equal to a fraction c_L of the lattice spacing a, similar to the melting of solids[25-27]:

$$\left\langle \mathbf{u}^2 \right\rangle = c_L^{\,2} a^2 \tag{4.1}$$

The brackets <....> represent integration over the wavevectors k, and in all directions. The vortex is expressed as an elastic object with elastic deformations within the vortex lattice, described by a Hamiltonian which includes the vortex

bulk modulus

applied along

By investigati

vortex displac

criterion, the r

where Gi is the

parameter ε_θ =

crystallographi

predicted at ve

vortex interacti

shear and bulk

strength weake

fraction from th

are expected to

The first

temperature su

untwinned, sing

resistivity was c

resistive transiti

crystallographic

bulk modulus c_{11}, tilt modulus c_{44}, and shear modulus c_{66} [26, 28] (here for a field applied along the c axis):

$$H = \frac{1}{2}\sum_{\mathbf{k}} \mathbf{u}_a(-\mathbf{k})[c_{11}(k)k_a k_b + \delta_{ab}\{c_{66}(k)[k_a^2 + k_b^2] + c_{44}k_c^2\}]u_b(k) \qquad (4.2)$$

By investigating positional fluctuations of this Hamiltonian with temperature, the vortex displacement is obtained. From these calculations, and the Lindemann criterion, the melting line has been estimated to be

$$B_m(T,\theta) \approx \frac{5.6}{\varepsilon_\theta}\frac{c_L^4}{Gi}H_{c2}(0)\left[1 - T/T_c\right]^\beta \qquad (4.3)$$

where Gi is the Ginzburg number, ε_θ is the superconducting anisotropy parameter $\varepsilon_\theta = \frac{1}{\gamma}\sqrt{\gamma^2\cos^2\theta + \sin^2\theta}$, θ is the angle between the field and the crystallographic c-axis, and $\beta \approx 1$–2[27, 29]. A melting transition has also been predicted at very low fields near $H_{c1}(T)$. In this dilute vortex limit the vortex-vortex interaction becomes exponentially small, substantially decreasing the shear and bulk moduli[25, 30]. As the field is decreased the lattice interaction strength weakens exponentially, allowing the vortex lines to wander a substantial fraction from their equilibrium positions and finally melt. The two melting lines are expected to meet at a temperature below T_C, as shown in Figure 4.1(b).

The first experimental indication of a vortex melting transition in high temperature superconductors was observed in resistivity measurements on untwinned, single crystals of YBCO[31, 32]. An extremely sharp drop in the resistivity was observed in the tail of the temperature dependent superconducting resistive transition in the presence of a magnetic field applied along the crystallographic c-axis. A typical example is shown in Figure 4.2(a). A kink, or

Figure 4
superco

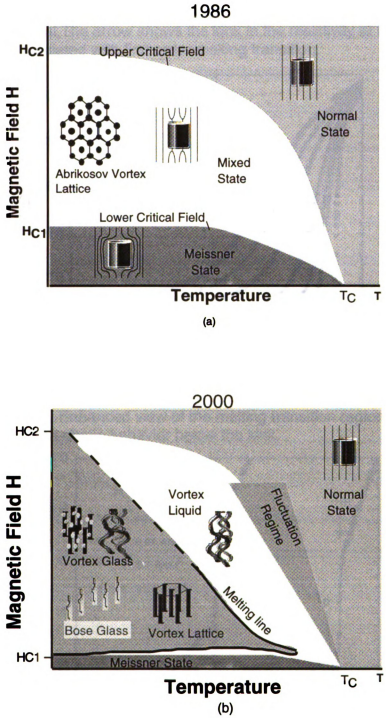

Figure 4.1 Phase diagram (a) for low temperature type II superconductors, and (b) for high temperature type II superconductors.

(a)
cry
ass

ρ (μΩ-cm)

(b
no

ρ (μΩ-cm)

Figur
YBCO

(a) Resistivity vs. temperature for high quality, untwinned YBCO crystal.The arrow shows the kink in the resistivity at H=4T, associated with first order melting transition.

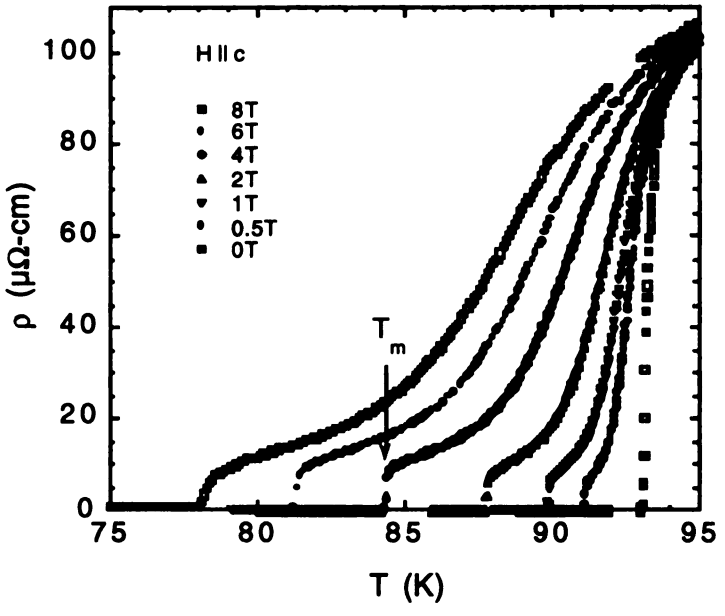

(b) Enhanced view of the melting transition region, showing non-ohmic behavior below the kink.

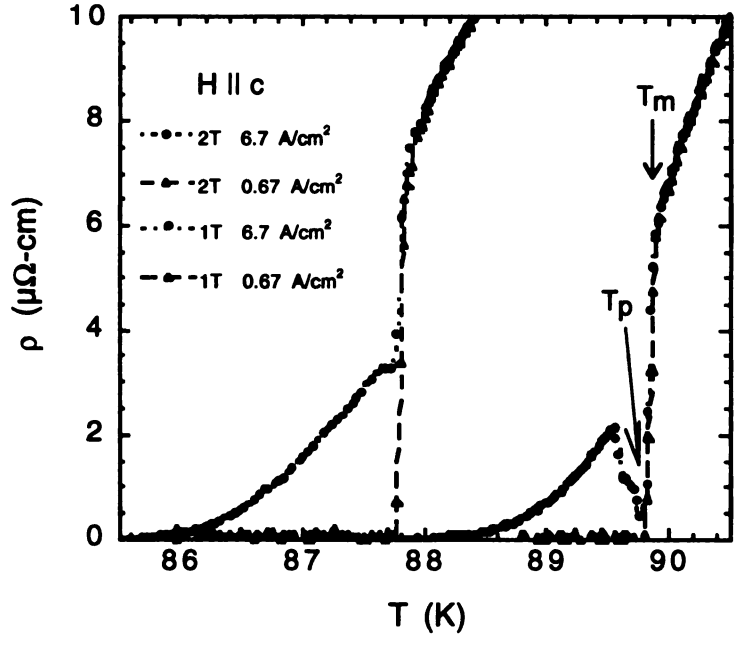

Figure 4.2 Resistivity versus temperature of an untwinned YBCO single crystal.

sharp drop ir

arrow). Alth

unusual aspe

superconduc

behavior abo

the splitting o

different mea

linked to a lat

field sweeps c

transition fro

One as

a peak effect

narrow tempe

a softening o

temperature

lattice to dist

critical curre

lattice are de

zero as the v

observed in

order melting

measuring c

increase in t

sharp drop in resistivity, is observed at T_m ~ 84 K for H = 4T (indicated by an arrow). Although a drop in resistivity can also be attributed to pinning, the unusual aspect of the sharp drop is that it is typically narrower than the zero field superconducting transition. Furthermore, the resistivity is characterized by ohmic behavior above the kink and non-ohmic behavior below the kink as indicated by the splitting of the two resistivity curves shown in Figure 4.2(b), obtained with two different measuring currents for H =1 and 2T. In addition, hysteretic behavior linked to a latent heat has also been observed in both temperature and magnetic field sweeps of the resistivity near the melting temperature, suggesting that the transition from vortex solid to liquid is of first order.

One aspect of pinning near a vortex melting transition is the occurrence of a peak effect in the critical current, where the critical current is enhanced within a narrow temperature window. The enhancement in critical current is attributed to a softening of the vortex shear modulus as one approaches the melting temperature from below. This relaxation of the shear modulus allows for the lattice to distort and accommodate nearby pinning sites, thus increasing the critical current[33]. Above the peak effect temperature T_p, the shear bonds of the lattice are destroyed due to vortex melting and the critical current plummets to zero as the vortex solid is transformed to a liquid. This peak effect has been observed in untwinned and weakly twinned single crystals of YBCO near the first order melting transition. In Figure 4.2(b), the resistivity curve obtained with a measuring current density of 6.7 A/cm^2 for H = 1T demonstrates a sharp increase in the resistivity with increasing temperature as one approaches the

'kink' associa

increasing th

However, jus

decreases to

temperature

lattice are des

softening of th

effect is seen

the *E-J* curves

curves. Below

sudden increa

shear modulus

of temperature

10^{-6} V / cm.

The vo

studied using

usual four pro

a crystal, for a

and the top ar

Since the curr

than at the bot

is established.

length can be

'kink' associated with the first order melting transition. This is expected since increasing thermal energy would tend to decrease the effectiveness of pinning. However, just below the transition temperature T_m, the resistivity rapidly decreases to nearly zero indicating that pinning is enhanced within this narrow temperature region. At T_m, the resistivity rises sharply as the shear bonds of the lattice are destroyed. Thus the peak effect in YBCO is associated with a softening of the vortex lattice shear modulus prior to melting[34-36]. The peak effect is seen as a crossing in the *E-J* curves as shown in Figure 4.3. For $T > T_m$, the *E-J* curves show ohmic behavior as indicated by the linear behavior of the curves. Below T_m, a sharp downturn in the *E-J* curves is obtained, indicating a sudden increase in vortex pinning associated with the appearance of a finite shear modulus. The inset of Figure 4.3 shows the critical current j_c as a function of temperature, obtained from the *E-J* curves using a voltage criterion of 10^{-6} V / cm.

The vortex melting transition for an untwinned YBCO sample was also studied using a flux transformer geometry. Four contacts are attached in the usual four probe geometry, but symmetrically to the top and bottom a-b plane of a crystal, for a total of eight contacts. The current is passed on the top surface, and the top and bottom voltages V_{top} and V_{bottom} are measured simultaneously. Since the current density is larger at the top surface where the current is injected than at the bottom surface, a gradient in the Lorentz force along the vortex lines is established. Information about the correlation of the vortex structure along its length can be obtained by monitoring the temperature dependence of the

E (V/cm)

dissipative

axis. It wa

defined by

establishir

Measurem

no c-axis c

transition,

the field dir

Thes

order vortex

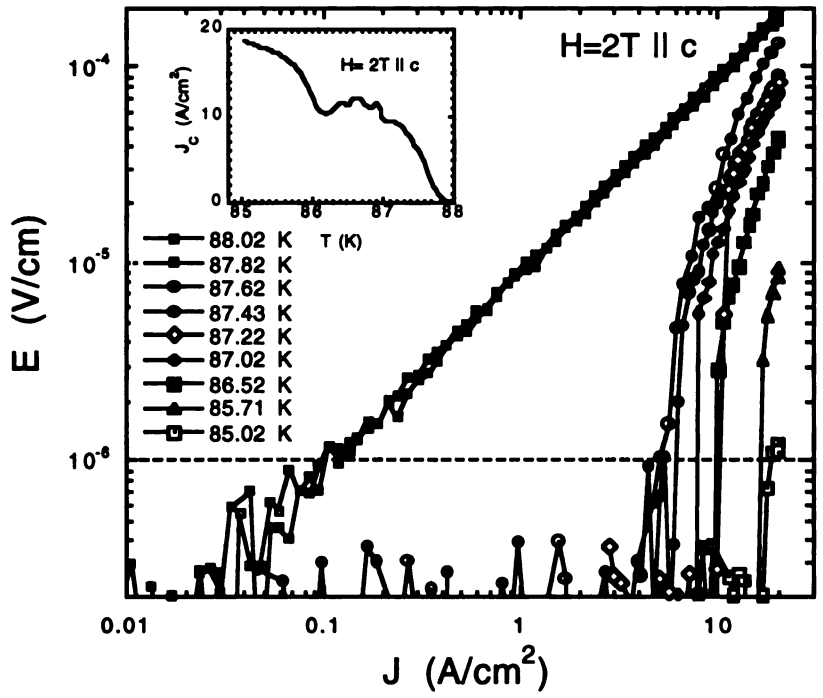

Figure 4.3 Current-voltage curves showing ohmic behavior above, and sharply non-ohmic behavior below the melting transition. The data is from the same sample as measured in Figure 4.2.

dissipative voltage near the melting temperature for an applied field along the c-axis. It was reported[37] that the correlation of the vortex line along the c-axis, defined by $V_{top} = V_{bottom}$, appears just below the melting temperature, establishing a three-dimensional vortex configuration within the solid. Measurements of the c-axis resistivity for samples from 15 to 100 μm thick found no c-axis coherence in the liquid state, and coherence just below the melting transition, providing evidence of a simultaneous loss of vortex correlation along the field direction at the melting transition for clean, untwinned samples.

These earlier transport measurements established the location of the first order vortex melting transition on the H–T phase diagram. However, since these

were non-equ

thermodynam

Accord

magnetic syst

derivative of th

The res

S correspondir

Thermodynam

in magnetizati

magnetization

vs. T measure

(i.e., $M_{liquid} >$

similar to mel

transition fron

vortex per do

where d=11.7

H_m, dH_m/dT a

melting transi

were non-equilibrium measurements no further information of equilibrium thermodynamic state could be obtained.

According to thermodynamics, for a first order phase transition of a magnetic system to occur, there must be a discontinuity of the first partial derivative of the Gibbs free energy G

$$G(T,H) = U - TS - MH \tag{4.4}$$

The resultant Clausius-Clapeyron equation predicts a jump in the entropy S corresponding to a discontinuity in the magnetization at the transition:

$$\Delta M \frac{\mathbf{d}H_m}{\mathbf{d}T} = -\Delta S \tag{4.5}$$

Thermodynamic evidence of a first order phase transition in YBCO was obtained in magnetization measurements[38, 39]. For H = 4T, a jump was found in the magnetization $4\pi\Delta M = 4\pi\left(M_{liquid} - M_{solid}\right)$≈0.3 Gauss[39] in both M vs. H and M vs. T measurements. The increase in magnetization in the liquid state (i.e., $M_{liquid} > M_{solid}$) indicates that the vortex density is lower in the solid state, similar to melting of ice. A convenient way to compare the entropy of the transition from one sample to another is to calculate the entropy increase per vortex per double Cu-O plane using the Clausius-Clapeyron equation

$$\Delta S_v = -\frac{\Delta M}{H_m}\frac{\mathbf{d}H_m}{\mathbf{d}T}\frac{\Phi_o d}{k_B} \tag{4.6}$$

where d=11.7 Å, the c axis parameter for YBCO, k_B is Boltzmann's constant, and H_m, dH_m/dT are obtained from $H_m = 99.7(1-T/T_c)^{1.36}$, which is the best fit of the melting transition data[39], obtaining a value of ΔS_v = 0.65–0.7 k_B for YBCO.

A dire

thermodyna

simultaneou

untwinned Y

coincided wit

were also pe

measured fro

wide range o

measuremen

More r

vortex melting

measuremen

one crystal. I

onset of the k

two crystals c

in the resistiv

and torque da

curves first ex

melting transi

power law dep

$\beta = 1.34 \pm .04$

crystals[32, 4

A direct correlation between the kink in the resistivity and the thermodynamic first order vortex melting transition was obtained through a simultaneous measurement of the resistivity and the magnetization on an untwinned YBCO crystal[40], confirming that the jump in the magnetization coincided with the onset of the kink in the resistivity. Calorimetric measurements were also performed on the same untwinned sample[41]. The entropy was measured from the latent heat of melting $\mathbf{L} = \mathbf{T}\Delta\mathbf{S}$, yielding $\Delta S_v \sim 0.45 k_B$ for a wide range of fields, from 1 to 8 Tesla in good agreement with the magnetization measurements.

More recently, in an experimental collaboration with ETH, the first order vortex melting transition was observed in high-resolution torque-magnetometry measurements[42, 43], which extended the melting line down to 0.09 Tesla in one crystal. In this collaboration, the melting transition was determined from the onset of the kink in the resistivity and torque magnetometry measurements on two crystals cleaved from the same parent piece. Figure 4.4 shows (a) the peak in the resistivity data and (b) the resultant melting transition from the resistivity and torque data. Also shown is the temperature where DC current-voltage curves first exhibit non-ohmic behavior. All three methods of establishing the melting transition are in good agreement with each other, and exhibit the same power law dependence with temperature, as given by eqn. (4.3). For this data $\beta = 1.34 \pm .04$, in agreement with data from other high quality untwinned YBCO crystals[32, 44].

(b)
10
8
6
4
2
0
H_{ir} (T)
0.8

(a) Resistivity and the derivative of the resistivity data.

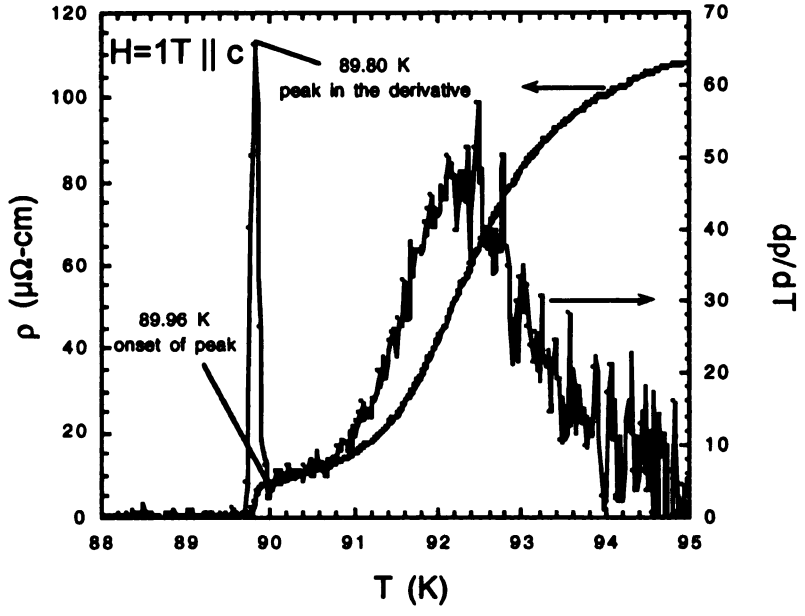

(b) Melting line from resistivity and torque measurements.

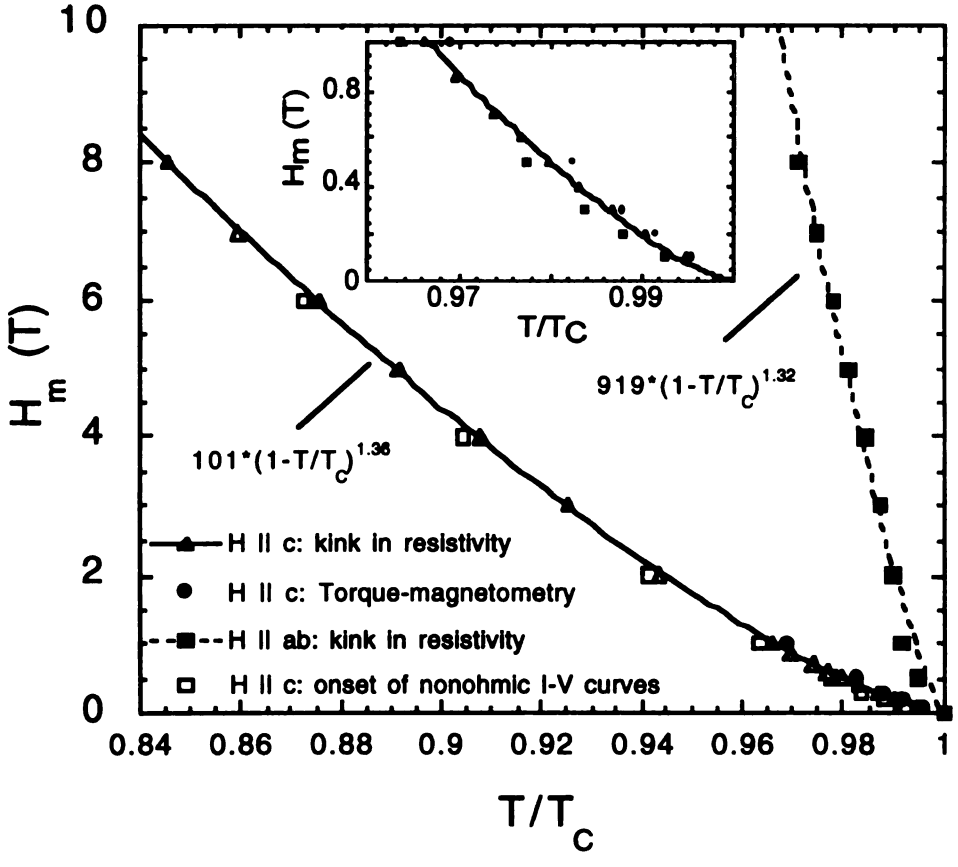

Figure 4.4

The order o

simulations

entropy jum

the latent he

the jump[47]

4.2 Critica

Recent trans

first order tra

magnetic fiel

point H_{ucp}, se

order melting

the 'kink' in t

magnetizatio

the peak in t

at H_{ucp}. Furt

point can va

optimally d

crystals[51, 5

can be dram

is dependent

The te

can be qualit

The order of the melting transition has been investigated using Monte Carlo simulations. Although earlier work predicted somewhat smaller values in the entropy jump[45, 46], more recent work has found a somewhat higher value of the latent heat ≈ 0.4 k_BT, as well as the temperature dependence for the size of the jump[47], and is seen as confirmation of the experimental results.

4.2 Critical points

Recent transport, magnetization, and calorimetry measurements indicate that the first order transition in some clean untwinned YBCO crystals terminates at high magnetic fields, giving way to a continuous transition above an upper critical point H_{ucp}, see Figure 4.5. In transport measurements, the termination of the first order melting transition at high fields is demonstrated by the disappearance of the 'kink' in the resistive transition at an upper critical point, H_{ucp}. Similarly, in magnetization and calorimetry measurements, the jump in the magnetization and the peak in the specific heat denoting the first order transition is also suppressed at H_{ucp}. Furthermore, it has been shown that the magnitude of this upper critical point can vary widely from sample to sample ranging from ~5-12 Tesla in ~optimally doped YBCO[48-50] to beyond 30 Tesla in overdoped YBCO crystals[51, 52], whereas in underdoped YBCO crystals the upper critical point can be dramatically reduced[53]. These results imply that the upper critical point is dependent upon the density of point defects within a sample.

The termination of the first order phase transition at the upper critical point can be qualitatively explained by considering the competition between the vortex

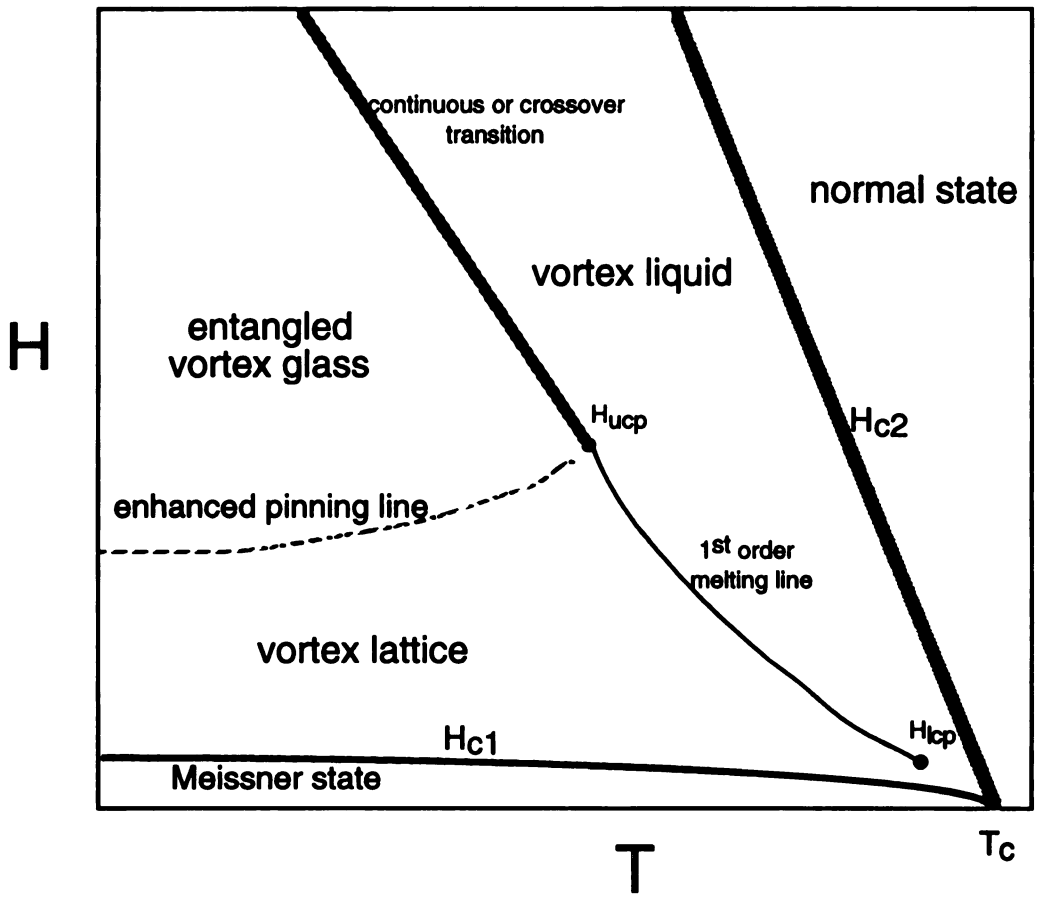

Figure 4.5 Possible three phases in the mixed state: Vortex liquid, lattice, and glass, in clean YBCO crystals.

elastic energy, the pinning energy, and the thermal energy[54, 55]. Along the first order vortex lattice melting line, the elastic energy of the vortex structure E_{el} can be described by a cage potential:

$$E_{el} = C_{66}u^2L + \varepsilon_1(u^2/L) \qquad (4.7)$$

where C_{66} is the shear modulus, u is the displacement of a vortex line from its equilibrium position, L is the length of the vortex and $\varepsilon_1 = \gamma^2/\varepsilon_o$ is the vortex line tension with $\gamma = m/M$ and $\varepsilon_o = (\Phi_o/4\pi\lambda^2)^2$. Along the melting line, we can use the Lindemann criterion $u^2 = c_L^2a^2$ to obtain $E_{el} = \gamma\varepsilon_o c_L^2a$, where a is the vortex

spacing. Th

$(L_o/L_c)^{1/5}[54$

$L_o \sim 2\gamma a$ is t

by minimizin

upper critica

energy, lead

$E_{pin} \sim B^{-1/10}$ a

energy of the

neighboring

energy E_{pin} ,

The e

the vortex so

vortex solid

lattice to an

of weak poi

simplified ca

which inves

lattice of lin

configuratio

sum of the

keep the vo

point defect

vortex solid

spacing. The pinning energy can be estimated by $E_{pin} = (\gamma \varepsilon_l c_L^2 \xi^2)^{1/3}$ $(L_o / L_c)^{1/5}$[54, 56] where the first term represents the depinning temperature, $L_o \sim 2\gamma a$ is the characteristic size of the longitudinal vortex fluctuation obtained by minimizing eqn. (4.7) with respect to L, and L_c is the pinning length. At the upper critical point, $E_l = E_{pin}$ and the pinning energy overcomes the vortex lattice energy, leading to the loss of the first order transition. Basically, $E_l \sim B^{-1/2}$ and $E_{pin} \sim B^{-1/10}$ and thus E_{pin} dominates at high fields. In this scenario, the elastic energy of the vortex E_{el}, tries to keep the vortex approximately aligned with its neighboring vortices while the isotropic point defects, with effective pinning energy E_{pin} , promote line wandering.

The existence of an upper critical point suggests a transformation within the vortex solid phase from an ordered lattice state below H_{ucp} to a disordered vortex solid state above H_{ucp}. Indeed, a field-driven transition from a vortex lattice to an entangled disordered solid has been predicted, due to the presence of weak point disorder[54, 56-60]. The transition can be described using a simplified cage potential description of the vortex lattice[54, 55] (see Figure 4.6), which investigates the energetics for a fluctuation $u(z)$ of a vortex line within a lattice of lines, and the influence of point pinning centers on the line configuration. For this model the elastic energy of the vortex E_{el}, which is the sum of the single vortex tilt energy and the vortex-vortex interactions, tries to keep the vortex approximately aligned within the cage. However, the isotropic point defects, with effective pinning energy E_{pin}, promote line wandering. The vortex solid is expected to transform from a lattice to an entangled vortex

vortex line

disc
d

F

Elastic energy of the vortex:

E_{el} = intervortex energy + tilt energy

$= c_{66} u^2 L + c_{44} u^2 / L$

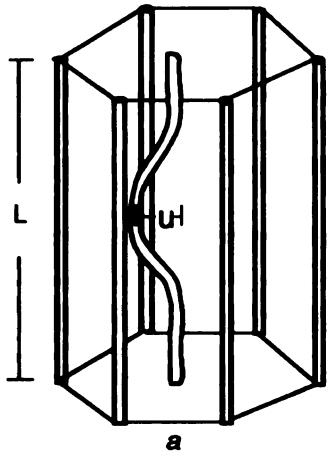

vortex line caged by 6 vortices

Vortex lattice:

$E_{el} > E_{pin}$

$u << a$

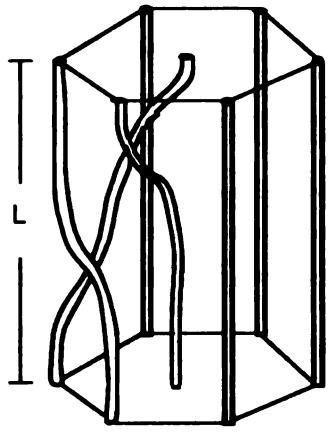

disorder-induced dislocations

Entangled vortex glass:

$E_{el} < E_{pin}$

$u \sim a$

Figure 4.6 Vortex line fluctuation **u** in a vortex lattice.

solid[57] when $E_{el} = E_{pin}$. At this point the transverse wandering length is of the order of the lattice spacing, and so dislocations can proliferate, leading to entanglement (see Figure 4.6). This entanglement transition line is expected to be marked by a sharp increase in the measured critical current[59]. Above this line the vortices are no longer tightly bound as a lattice, and so adjust to the local pinning potential, becoming more effectively pinned by the defects. The fact that entangled vortex lines would have to be cut in order to move independently, results in the increase in pinning efficiency and critical current. For this new state, an increase in temperature may produce a second-order transition[29] from a vortex glass to a liquid.

Evidence of a phase transition from a vortex lattice to a disordered solid has been obtained from neutron diffraction data on BSCCO[61]. Measurements at low fields and temperatures show the expected diffraction peaks for a hexagonal lattice. The peaks disappeared with increasing temperature (vortex lattice melting) as well as with increasing field (vortex lattice to disordered solid). Magnetization measurements in BSCCO[62, 63] and YBCO[53, 64-67] samples also show a sharp increase in the critical currents represented as the onset of a second magnetization peak as the magnetic field is raised within the solid-solid transition is crossed, as expected for a transition from a weakly pinned lattice to strongly pinned glass. This transition is shown as an enhanced pinning line in Figure 4.5. It is an open question whether this ordered-disordered transition line meets the melting line at H_{ucp}, which would then suggest H_{ucp}, to be a multicritical point. At higher fields the magnetization reaches a maximum, known as the 2^{nd}

magnetization peak, and then decreases monotonically with increasing field. Recent measurements[50, 67, 68] suggest that the 2nd magnetization peak line may be related to the critical current peak effect seen in YBCO crystals. In this scenario the upper critical point would not be a multicritical point, and the disordered solid state would also exist in the region where the peak effect is seen, which is close to but just below the first-order melting line. As the temperature or field is lowered, the vortex lattice would then be established.

In the transformer configuration measurements[49], the data suggests strong evidence of flux line cutting in the solid phase above H_{ucp}, where $V_{bottom} = 0$ Volts, while $V_{top} \neq 0$. This suggests that the part of the vortex lines near the top are in motion, while the part near the bottom are in a strongly pinned solid phase, with vortex cutting occurring within the bulk of the sample. This work also finds evidence of an entangled state above H_{ucp} from c-axis resistivity measurements. The data show dissipation in the c-axis resistivity at temperatures where the transverse resistivity has dropped to zero, implying the existence of vortex loops and entanglement above H_{ucp}.

With increasing temperature, in the region above H_{ucp} thermal fluctuations induce a transition from the entangled solid state to the liquid state. The vortex glass theory[22] predicts a continuous transition in the case of isotropic disorder, with the current-voltage curves obeying critical scaling rules within the critical fluctuation regime[29]. Measurements on clean untwinned YBCO have yet to produce this scaling, however the vortex-glass theory also predicts a power law behavior for relatively strong driving currents near the transition:

$$\rho \sim (T - T_{VG})^{s} \tag{4.8}$$

By evaluating the ohmic tail of the resistivity above H_{ucp}, a power s = 5–7 has been found[48, 64], with good agreement between T_{VG}, obtained by a fit of the measured resistivity[48] to eqn. (4.8), and T_{irr}, which is defined as the onset of irreversibility in the magnetization measurements[64]. Nevertheless, since no critical fluctuation regime is observed, then the above data cannot clearly be associated with a phase transition, and thus no definitive observation of the vortex glass transition has been found.

More recently, analogous to the upper critical point, a lower critical point has been identified in YBCO single crystals. For example, in both the resistivity and magnetometry data in Figure 4.4(b) inset, the melting line appears to terminate at a lower critical point H_{lcp} = 0.1 Tesla. Similar to the upper critical point, this point is defined by the field below which the kink in the resistivity, jump in magnetization, or peak in the specific heat is no longer seen in the data. There is a wide variation of the location of this point[14, 16, 43, 69-72], but for high quality untwinned samples the lower critical field is consistently below 0.5T, with the lowest measured at 0.09T. The lack of a measurable kink at lower fields may be due to its close proximity to the critical fluctuation regime of the superconducting order parameter within 1 K of T_C, or simply due to a lack of resolution of the experimental techniques at very low fields. Also, if the sample is not perfectly homogeneous, the position of the melting transition may be smeared due to a distributed melting temperature. Thus a true lower critical point may not exist in very high purity, low point defect crystals.

A lower critical point would possibly mark the onset of a higher order liquid-to-glass transition below H_{lcp}. If a glass state does exist below H_{lcp}, thermodynamics demands that there be yet *another* solid-solid phase transition, from a disordered glass to an ordered lattice. (For an alternative view, which predicts a liquid-liquid transition below a critical end point and no first-order melting line, see[73].) The existence of the new lower critical point and the vortex phase transition below H_{ucp} will be discussed in Chapter 9.

In summary, the first order vortex lattice melting transition in clean untwinned crystals of YBCO has been firmly established via dynamic and thermodynamic measurements. This first order line is shown to terminate at both high and low magnetic fields. Above and below the upper and lower critical points, the first order transition transforms into a continuous higher order transition. A consequence of the critical points is that novel vortex phases may exist within the vortex solid state at high and low magnetic fields. Some of the novel phases, such as an entangled vortex solid phase at high fields, has been the focus of extensive experimental and theoretical research. On the other hand, not much is known about the vortex solid state below the lower critical point at low fields.

In order to shed light on this interesting regime of the vortex phase diagram, we examine the effect of induced columnar defects on the first order vortex melting transition. The advantage over point defects is that the density of columnar defects can be carefully controlled and monitored experimentally. Furthermore, being line defects, these defects are dimensionally well matched

with vortex

temperatur

a fundamer

transition ca

defects. Th

on induced

with vortex lines and have been proven to be strong pinning sites at high temperatures near the melting transition. In addition, this study will shed light on a fundamental issue in the physics of phase transitions, namely how a first order transition can transform into a second or higher transition with the introduction of defects. These results will be discussed and compared with collaborative work on induced point defects in YBCO via electron and proton irradiation.

Chapter 5

VORTEX PINNING BY DEFECTS IN $YBa_2Cu_3O_{7-\delta}$ SINGLE CRYSTALS

5.1 Pinning in the vortex liquid state by twin boundaries

As discussed in Chapter 4, in transport measurements on untwinned, clean YBCO crystals, strong pinning and non-ohmic behavior was only seen below the melting transition. However, interesting behavior in the liquid state has been found in as-grown YBCO crystals with twin boundaries. Twin boundaries are strain fields along the <100> and <110> which occur during the growth process of YBCO when the crystal undergoes a tetragonal to orthorhombic transition. To the left and right of a twin plane, the basal structure of the crystal is rotated by ninety degrees. These planar objects, are of the order of 10 Å wide, and contain atomic scale defects such as oxygen vacancies and atomic scale ion displacements. These twin boundaries can be spaced from anywhere between 1000 Å and several microns apart and, in homogenous crystals, extend throughout the thickness of the sample, hence serving as intrinsic pinning sites in as-grown YBCO crystals prior to detwinning[74].

The viscosity of the vortex liquid state in the presence of twin boundaries has been studied by Marchetti and Nelson using a hydrodynamic approach[75]. The model describes the flow of vortices confined in channels made of parallel twin boundaries as shown in Figure 5.1. The viscosity of the vortex liquid within the channels is described in terms of a healing length extending from the twin boundaries where the vortices are localized, to the center of the channel where

Fig
the

the vortices

velocity is

walls, loca

contained

described

Lorentz f

interactic

Here the

model,

possibi

accour

as the

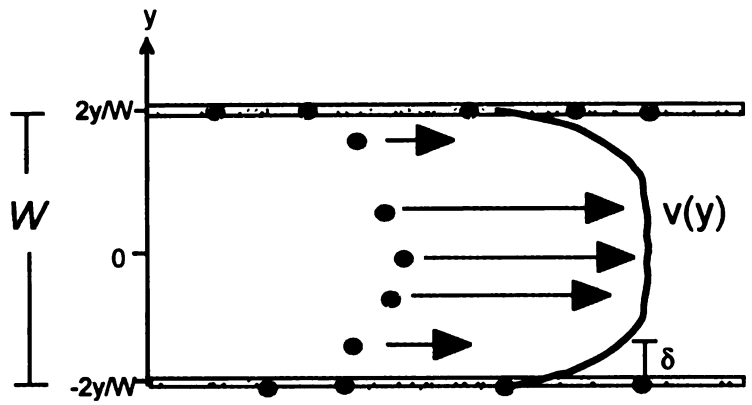

Figure 5.1 Viscous damping due to twin boundaries. The curve in the figure shows the velocity distribution, given by eqn. (5.1).

the vortices are less restricted. For a twin boundary spacing *W*, the vortex velocity is predicted to depend on the position y with respect to the twin boundary walls, located at $y = \pm W/2$, see Figure 5.1. The viscous damping coefficient is contained in a characteristic healing length $\delta = \sqrt{\eta/\gamma}$, where γ is the previously described single vortex frictional drag, η is the intervortex viscosity, and v_o is the Lorentz force dependent single vortex velocity in the absence of intervortex interactions (recall eqn. (3.3)). The resultant velocity profile is predicted to be:

$$v(y) = v_o\left[1 - \frac{\cosh(y/\delta)}{\cosh(W/2\delta)}\right] \tag{5.1}$$

Here the vortices in the twin boundaries are assumed to be stationary. In this model, the viscosity η is large enough to effect the vortex flow only when the possibility of vortex entanglement (i.e. crossing along the lines) is taken into account. This is seen as an increase in the viscosity at T_{TB}, becoming very large as the temperature is decreased.

The interplay between the first order vortex melting transition discussed in Chapter 4 and twin boundary pinning in the liquid state mentioned above is shown in a YBCO crystal with only two twin boundaries space 140μm apart[34], as shown in Figure 5.2. When the field was applied parallel to the twin boundary planes, a 'shoulder' appeared at T_{TB}, where the resistivity starts to drop rapidly. Below T_{TB} the current-voltage measurements were found to be weakly non-ohmic. By rotating the field with respect to the twin boundaries and thereby weakening the effect of twin boundary pinning on the vortices[74], the sharp melting transition T_m was reestablished at a temperature below T_{TB}. In this case, the resistivity is non-ohmic only below T_m. This is strong evidence that there is significant intervortex viscosity in the liquid state: When individual vortex lines become pinned by the twin boundary planes, the motion of vortices between the planes is reduced by viscous damping.

The twin boundary shoulder has also been investigated in a heavily twinned crystal, using the flux transformer configuration[31, 76]. In this work, evidence of c-axis vortex correlation is first seen in the liquid state at $T_{Th} \sim T_{TB}$. Below T_{Th} and at low currents $V_{top} = V_{bottom}$, implying either a disentangled vortex liquid state or a topologically entangled liquid where the vortex cutting energy is large. The T_{Th} transition also marks the disappearance of linear c-axis resistivity, providing evidence of vortex correlation along its entire length in the liquid state below T_{Th}[77]. For high applied transport currents however, $V_{top} > V_{bottom}$, indicating evidence of vortex line cutting[30, 78-80]. In this model the force necessary to cut the vortex lines[80] becomes less than the Lorentz force, and so

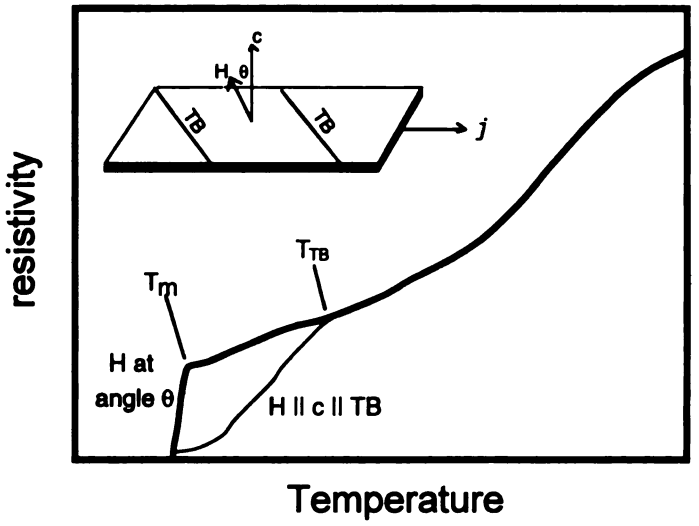

Figure 5.2 Angular dependence in resistivity vs temperature data, H=4T. After W. Kwok, *et al.*, *Peak Effect as a Precursor to Vortex Lattice Melting in Single Crystal* $YBa_2Cu_3O_{7-\partial}$, Physical Review Letters **73**, 2614 (1994).

vortex cutting occurs, with the vortex motion faster at the top surface than the bottom, resulting in a higher voltage at the top surface of the crystal. The temperature dependence of T_{Th} for the establishment of c-axis correlation is also found to be thickness dependent in these twinned samples, as expected since the energy to drag the vortices should increase with line length[77]. Both the two twin and multiple twin studies above provide evidence that the extended twin planes enhance the vortex coherence along the c-axis, and thus vortex line straightening.

5.2 Point defects and the Vortex Glass theory

The effect of isotropic point defects on the melting transition has been studied theoretically[22, 29]. The transition is predicted to be a continuous phase transition to a glass state known as the Vortex Glass (VG) phase, with a critical

fluctuation regime close to the Vortex Glass transition temperature T_{VG}. Within this regime fluctuations in the vortex line correlation length l_{VG} are expected to scale as

$$l_{VG} \sim | T - T_{VG} |^{-\nu'} \tag{5.2}$$

where ν' is the Vortex Glass static critical exponent. (For the Vortex Glass model, the critical exponents are primed in this thesis, in order to distinguish between this model and the Bose Glass model described below.) In this isotropic model the vortex correlation lengths both parallel and perpendicular to the applied field are expected to diverge at the glass transition temperature, following eqn. (5.2). The relaxation time of a fluctuation is expected to scale with the dynamic scaling exponent z', as $\tau \sim {l_{VG}}^{z'}$. The fluctuation regime is characterized by a non-ohmic current-voltage (E-j) behavior close to the transition, which scales both above and below T_{VG} according to:

$$E\ell_{VG}^{1+z'} = e_{\pm}(j\ell_{VG}^{2}) \tag{5.3}$$

Using eqn. (5.3), the E-j curves collapse onto the smooth functions $e_{\pm}$ for temperatures above and below T_{VG}. In addition, for $T > T_{VG}$, and within the critical temperature regime but at low current densities, ohmic behavior is expected. Here the resistivity scales as

$$\rho(T \to T_{VG}^{+}, j \to 0) \sim (T - T_{VG})^{\nu'(z'-1)} \tag{5.4}$$

At temperatures above the critical regime, a relatively free vortex liquid is predicted, characterized by ohmic behavior for all currents. Below T_{VG} for low current densities, the theory predicts diverging barriers to vortex motion, resulting in a true superconducting state, defined here as $\rho(j \to 0) \to 0$. In terms of a

measured electric field, the theory predicts a sharp decrease with decreasing current: $E \propto e^{-c(j_c/j)^{\mu}}$, where μ is the glassy exponent, predicted to lie between 0.25 and 1[22, 36].

Although a number of earlier papers claimed to experimentally observe a Vortex Glass transition, all of them involved YBCO samples with correlated disorder in the form of twin boundaries. Transport measurements on untwinned YBCO single crystals with point defects created by electron[16] and proton[81, 82] irradiation have so far failed to observe the nonohmic *E-j* curves predicted by the Vortex Glass theory. For all these measurements on irradiation induced disordered crystals, the kink in the resistivity is replaced by a monotonically decreasing ohmic resistivity. However, the tail of the resistivite transition has successfully been scaled to eqn. (5.4) in the case of a high density of defects induced by proton irradiation[82], with the resultant resistive scaling exponent $z'(\upsilon'-1)$ being independent of the field and field direction, in agreement with the isotropic Vortex Glass model. The determination of the non-linear E-J behavior above and below the critical regime has so far eluded measurements, probably due to the high voltage sensitivity needed to probe the vortex glass state at the transition. Apparently, point defects shift the melting transition to lower temperatures in a monotonic fashion, whereby the resistivity gradually decays to zero value but at temperatures where the measured voltage signal becomes immeasurably small.

5.3 Hig

Transport

produced b

the expect

Glass theo

glass trans

overdampe

equation fo

divergence

from above

This equatio

solid transiti

diverging co

the effects o

However, it i

measureme

simple visco

transition is

5.4 Bose

Columnar de

temperature

5.3 Highly viscous Vortex Molasses model

Transport measurements on untwinned YBCO single crystals with point defects produced by proton irradiation have shown purely linear E-J curves, in contrast to the expected nonohmic behavior for diverging barriers as predicted by the Vortex Glass theory. An alternative theory[83], based on the general theories of liquid-glass transitions, has recently been introduced. It describes a highly viscous, overdamped "Vortex Molasses" model, characterized by a Vogel-Fulcher equation for the liquid relaxation time $\tau \sim \exp[1/(T - T_g)]$. This exponential divergence leads to a rapidly decreasing resistivity as the glass is approached from above:

$$\rho(t) = \rho_o e^{-[1/(T-T_g)]} \tag{5.5}$$

This equation describes ohmic behavior of the viscous liquid, near the liquid to solid transition. The general theory is independent of whether there is any diverging coherence length scale, because measurements are overshadowed by the effects of the rapidly increasing viscosity, resulting in purely ohmic resistivity. However, it is difficult to discern between eqns. (5.4) and (5.5) from resistivity measurements[83]. Thus at this time it is an open question as to whether a simple viscous vortex liquid akin to a window glass or a true Vortex Glass transition is occurring in the case of point defect pinning.

5.4 Bose Glass theory

Columnar defects provide one of the most efficient vortex pin sites in high temperature superconductors[84, 85]. These straight cylindrical defect tracks,

consisting of a normal core approximately 40 to 100 Å in diameter and up to 50 μm long, can be created by the impingement of high energy, heavy ions upon a YBCO sample. Since the defect diameter is comparable to that of the core radius of the vortex lines, these defect tracks are highly suitable as anisotropic pinning sites. The density of columnar defect sites is usually defined by the equivalent dose matching field B_Φ necessary to produce the same vortex line density as columnar defects: $n_{defects} = B_\Phi / \Phi_o$, resulting in a mean defect spacing $d = 1/\sqrt{n} = \sqrt{\Phi_o / B_\Phi}$.

Columnar defects have significant affect on the vortex motion, which are strongly correlated with the ratio of the vortex to columnar defect density. For applied fields *H* on the order of the defect matching field B_Φ and parallel to the defects, the vortex lines are strongly localized to the columnar defects for temperatures well below the melting transition. The random defect sites act to destroy the long-range order of the vortex lattice, producing a glassy state known as the Bose glass phase[86, 87]. This solid state is characterized by localization of vortex lines on the individual columnar defects, resulting in a disentangled vortex phase with the vortices randomly positioned transverse to the applied field. With increasing temperature the lines become progressively delocalized from the defects, and above the Bose glass melting temperature an entangled vortex liquid is predicted. The transition from glass to liquid is continuous, and from the theory of critical phenomena[88, 89] it is predicted that there exists a critical fluctuation region located close to, and both above and below T_{BG}. Within

this critical region it is possible to collapse *E-j* curves by scaling the data with appropriate diverging coherence lengths.

The vortex free energy of a system of vortices in a random configuration of straight columnar defects is presented for a system of N vortex lines, length L, aligned along the z = c axis = defect direction, in terms of transverse (ab plane) fluctuations in position $\mathbf{R}_\mu(z)$, subject to a Lorentz force $\mathbf{f}_L$[87]:

$$\mathcal{H} = \int_0^L dz \left\{ \sum_\mu^N \frac{\varepsilon_1}{2} \left[\frac{d\mathbf{R}_\mu(z)}{dz} \right]^2 + \frac{1}{2} \sum_{\mu \neq \nu} V^{\text{int}}\left[\mathbf{R}_\mu(z) - \mathbf{R}_\nu(z)\right] \right.$$

$$\left. + \sum_\mu^N U_r\left[\mathbf{R}_\mu(z)\right] - \mathbf{f}_L \cdot \sum_\mu^N \mathbf{R}_\mu(z) \right\} \qquad (5.6)$$

The first term includes the vortex tilt energy, where $\varepsilon_1 \approx (1/\gamma)^2 (\Phi_o / 4\pi\lambda_{ab})^2 \ln(\kappa)$is the line energy. The intervortex pair interactions are given by V^{int}, which decays logarithmically at short distances r < λ_{ab}, and exponentially for r > λ_{ab}. The columnar defect interaction is given by the z-independent potential U_r, which is approximated by a cylindrical potential constant well depth U_o, radius b. The term Bose glass arises because eqn. (5.6) is analogous to a system of N charged bosons in a 2 dimensional space, with randomly distributed defects acting as local pinning sites[86, 87]. A vortex line 'wandering' along the length L of the vortices, given by the thickness of the crystal corresponds to a boson wandering in time. A strongly pinned vortex line can then be described as a boson localized (in space and time) to a defect. The boson/vortex mapping is given in Table 5.1.

Bosons	mass	$\hbar$	$\hbar/kT$	Pair potential	Charge	Electric field	Current
Vortices	ε_1	T	L	$2\varepsilon_o K_o(r/\lambda)$	ϕ_o	zxJ/c	E

Table 5.1 Charged bosons-vortex lines analogy. After D. R. Nelson, V. M. Vinokur, *Boson localization and correlated pinning of superconducting vortex arrays*, Physical Revew B **48**, 13060 (1993).

The melting transition may be evaluated within the Bose glass theory. As the temperature increases, thermal fluctuations tend to promote vortex wandering via the creation of vortex kinks, see Figure 5.3. The theory predicts a wandering length from the original pin center, called the transverse wandering length $l_\perp(T)$. The 'time' scale for a boson to wander a distance $l_\perp(T)$ is given by the longitudinal wandering length along z, $l_\parallel(T)$. Close to the transition these two lengths diverge as T_{BG} is approached from both above and below the transition:

$$\ell_\perp \sim 1/|T_{BG} - T|^\nu \tag{5.7}$$

and the characteristic length of a fluctuation, along the vortex line,

$$\ell_\parallel \sim \ell_\perp^2 \tag{5.8}$$

where T_{BG} is the Bose glass transition temperature, defined as the temperature where the transverse fluctuation $l_\perp(T)$ is approximately equal to the intervortex distance d, and ν is the critical scaling exponent. By this definition, at the Bose glass melting transition the vortices become entangled, leading to extended wandering. The relationship in eqn. (5.8) is due to the anisotropic length scales

of a fluctuation[90], and has been confirmed using Monte Carlo simulations[91].

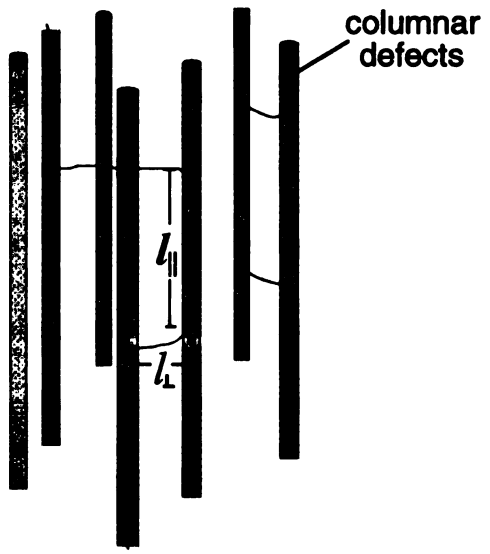

Figure 5.3 Vortex lines in the presence of columnar defects.

The relaxation time of a fluctuation is expected to diverge at T_{BG}, with a dynamic scaling exponent z:

$$\tau \sim \ell_\perp^z \tag{5.9}$$

From the diverging relations given in eqns. (5.7-5.9), it is possible to scale both *E* and *j*. The appropriate scaling relations are obtained via the anisotropic Ginzburg-Landau free energy, eqn. (2.4): $j \propto \partial f / \partial \mathbf{A}_\perp$, $E \propto \partial \mathbf{A}_\perp / \partial t$, with *H* || c, $\mathbf{A}_\perp$ is the vector potential in the ab plane, and $\mathbf{A}_\perp \sim 1/l_\perp(T)$. The current density is then found to scale as $j \sim 1/\ell_\perp \ell_\parallel$, while the resultant electric field produced by vortex motion scales as $E \sim 1/\ell_\perp \tau$, leading to the scaling hypothesis describing the critical regime:

$$E\ell_\perp^{1+z} = F_\pm(\ell_\perp \ell_\parallel J \Phi_0 / cT) \tag{5.10}$$

where $F_{\pm}$ is the universal scaling function. While F_{+} and F_{-} are unknown, the scaling hypothesis allows current-voltage data for different temperatures to be collapsed onto F_{+} above, and F_{-} below T_{BG}. Since the response is finite at the transition, the two divergent lengths must cancel there, giving a power law dependence $E \sim J^{(z+1)/3}$ when $T = T_{BG}$. For temperatures near but just above T_{BG}, in the limit of very low current density, the resistivity is expected to be ohmic, in agreement with the TAFF model. Thus in this limit the function $F_{+}(x) \sim x$. From eqn. (5.10) the resistivity should then vanish as

$$\rho(T \to T_{BG}^{+}, J \to 0) \sim (T - T_{BG})^{\nu(z-2)} \tag{5.10}$$

The Bose glass theory differs dramatically from the Vortex Glass theory for fields applied at an angle θ from the c-axis. Specifically, the Bose glass theory predicts anisotropic pinning, as opposed to the isotropic pinning characteristics of the Vortex Glass theory. This difference is inherent in the two diverging length scales (eqns. (5.7) and (5.8)) in the Bose glass model, which predicts a maximum in pinning strength for a field applied along the columnar defect direction, and thus a cusp in the transition temperature, see Figure 5.4. Because of this, for $T=T_{BG}(\theta=0^{o})$ the constant current angular resistivity (i.e. along the line marked A in Figure 5.4) is expected to decrease with decreasing tilt as $\rho \sim H_{\perp}^{(z-2)}$[87, 92]. Within the Bose glass phase an infinite tilt modulus is expected[87]. In this 'transverse Meissner phase', the application of a small perpendicular field $H_{\perp}$ will not affect the vortex system, as the vortices remain localized along the defect tracks. At some finite, temperature dependent $H_{\perp}^{c}(T)$, a lock-in transition occurs, where the strongly pinned Bose glass state is

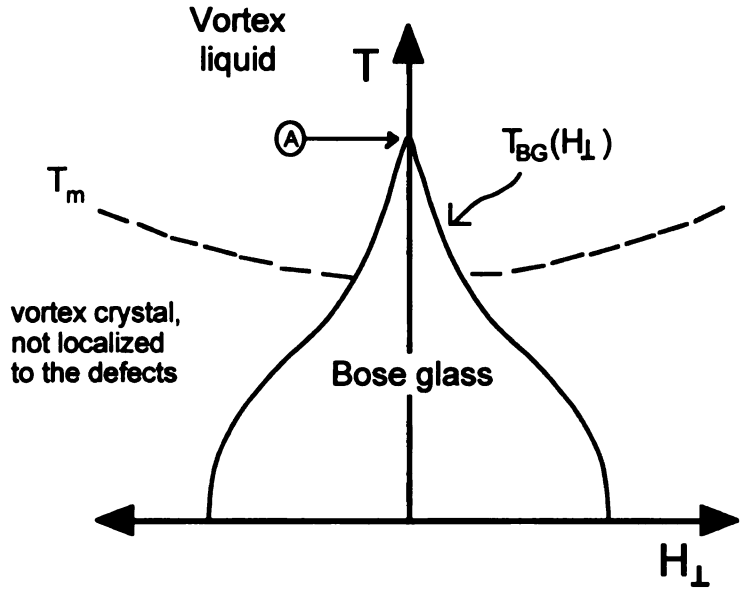

Figure 5.4 The Bose glass transition in a constant applied field H aligned with the columnar defects, as a function of a perpendicular applied field $H_\perp$. After D.R. Nelson and V.M. Vinokur, *Boson localization and correlated pinning of superconducting vortex arrays*, Physical Review B **48**, 13060 (1993).

transformed continuously into a kinked vortex configuration[93]. The transition is characterized by a sharp increase in the measured resistivity, due to the relatively free motion of the kinks as they move along the columnar defects, producing a net vortex flow in the Lorentz force direction. The lock-in transition is expected to scale from above as[92]

$$T_{BG}(0) - T_{BG}(\theta) \sim | H_\perp^c |^{1/\upsilon} \qquad (5.12)$$

The transition cannot be scaled from below, since $l_{||}$ is essentially infinite (equal to the sample thickness) below the transition. For large angles, the vortices are not expected to remain localized to the defects at low temperatures, leading to a vortex crystal state with different characteristics than the Bose glass, but this state is not investigated. In Chapter 8, the Bose glass theory is studied via

transport measurements of YBCO crystals containing columnar defects. Both the non-ohmic critical regime as well as the lock-in transition are investigated.

Chapter 6

CRYSTAL GROWTH AND PREPARATION

The crystal structure of $YBa_2Cu_3O_{7-\delta}$ with $\delta=0$ is shown in Figure 6.1. $YBa_2Cu_3O_7$ belongs to the ABO_3 (A=Yttrium; B=Barium; C=Copper; O=Oxygen) structure of the perovskite family. The unit cell is constructed of a simple stacking of the ABO_3 perovskite structure with some missing oxygen atoms. The oxygen atom vacancies are located around the Yttrium site and in the basal plane along the a direction. A structure without oxygen deficiency will have the formula $YBa_2Cu_3O_9$, while the structure with the missing oxygen gives $YBa_2Cu_3O_7$. The missing oxygen atoms surrounding the Yttrium atom are responsible for the layered structure of the buckled two dimensional Cu(2)-O(2)/O(3) planes sandwiching the Y site. An interesting unique feature is the square planar two dimensional chains along the basal **b** direction and the missing oxygen atoms along the **a** direction which are responsible for the orthorhombic structure in this compound.

The superconducting state is dependent on the hole concentration[94, 95] in the CuO_2 planes (see Figure 6.2). As the density of holes increases, the system transforms from an insulating anti-ferromagnetic state to the superconducting paired state, both states characterized by long-range interactions. For $YBa_2Cu_3O_{7-\delta}$, the hole concentration is controlled by the oxygen stoichiometry, as shown in the phase diagram for YBCO[96], see Figure 6.3. According to the charge transfer model[97], the CuO chains act as charge

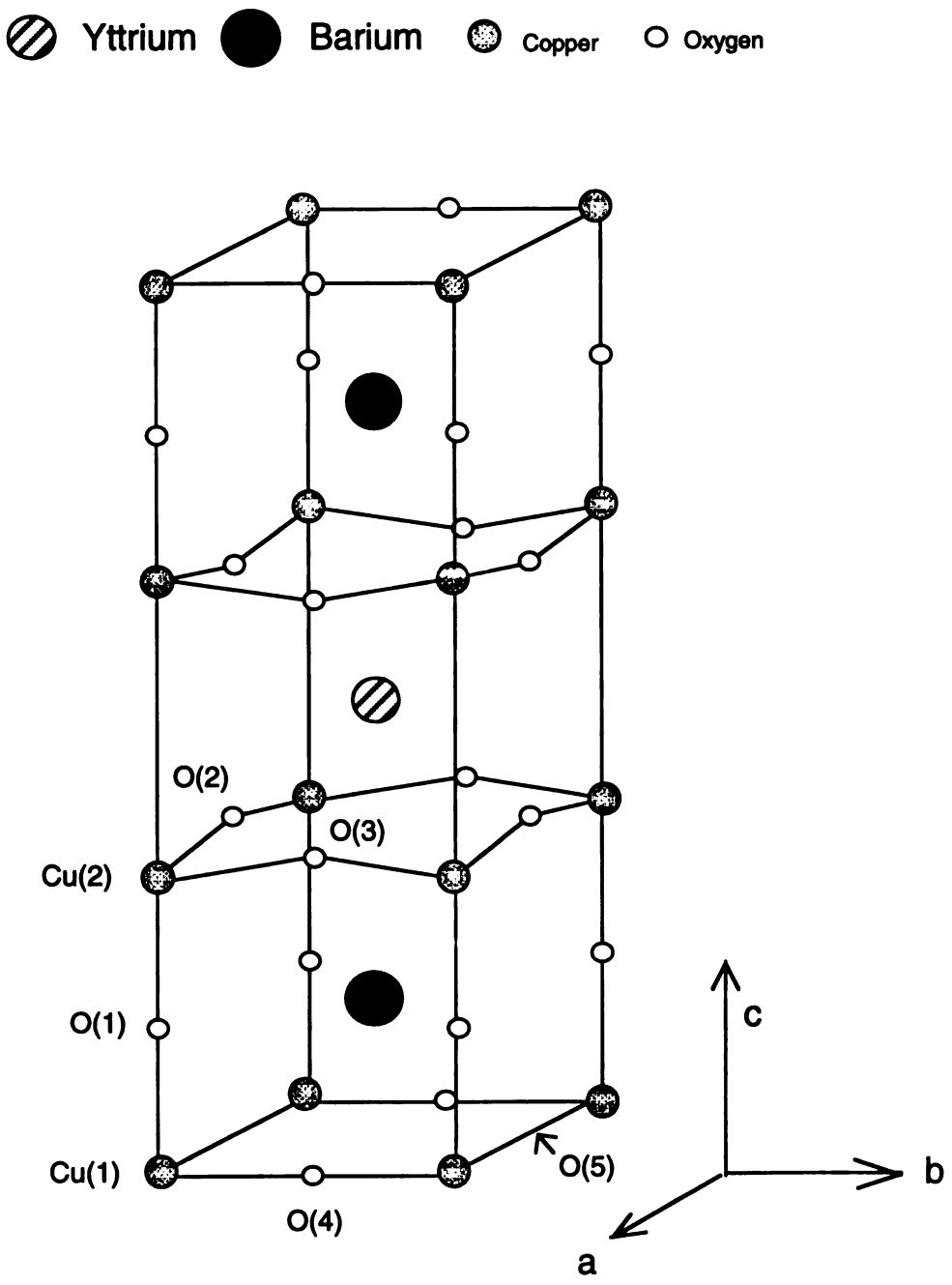

Figure 6.1 $YBa_2C_3O_{7-\delta}$ unit cell shown here for $\delta=0$.

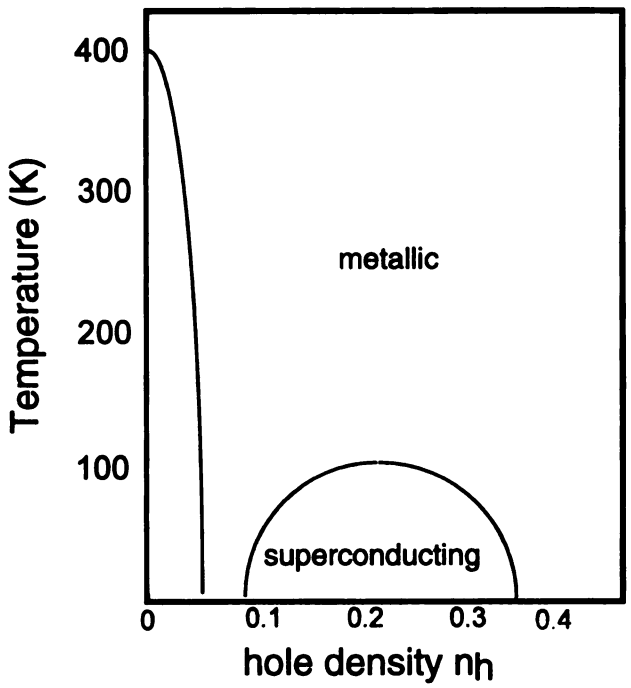

Figure 6.2 High temperature phase diagram.

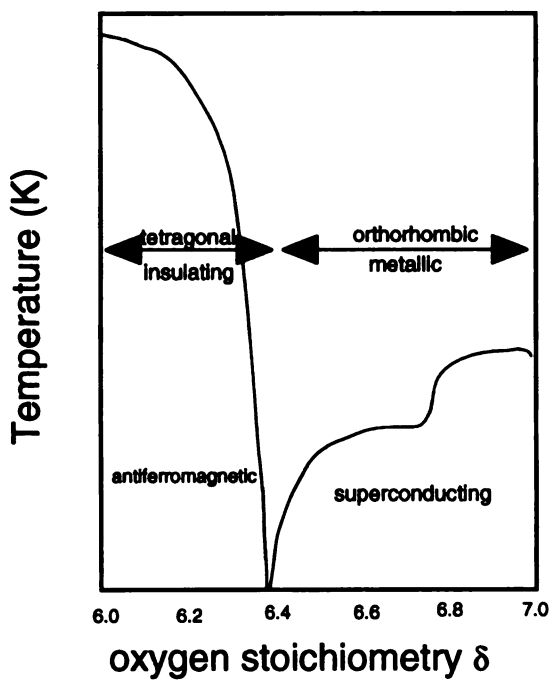

Figure 6.3 Phase diagram for YBCO as a function of oxygen stoichiometry.

reservoirs for the CuO_4 planes. The initial development of the chains, which occurs at the tetragonal-orthorhombic transition at ~680° C[98] ($\delta \approx 6.4$ in the figure), produces a sharp increase in the hole concentration and the superconducting state at low temperatures. The hole density is strongly dependent upon the Cu-O bond lengths of the system, both in the CuO_4 plane[95] and perpendicular to them[99]. As the O(4) atom sites become progressively filled up with increasing δ, the Cu(1)-O(1) bond length increases. The net effect is a change in the Cu(1) coordination[97]. This lowers the Cu(1) charge state, with the charge transferred from the CuO_4 planes. The increase in oxygen also leads to a shortening in the length between the planes and chains, allowing for more charge transfer between them. The hole concentration, or hole doping, reaches an optimum value given by the maximum transition temperature T_C, at δ=6.94. For $\delta > 6.94$, the hole concentration becomes overdoped, characterized by a small drop in T_C.

The occupancy of the O(4) and O(5) sites, as well as the superconducting transition T_C, depend critically on the oxygen content of the crystal[100-102]. The oxygen concentration varies widely in YBCO samples, and can be adjusted by annealing the sample in an oxygen environment. As noted in Figure 6.3, there is a tetragonal to orthorhombic transition as a function of oxygen concentration. For $\delta<0.1$, the O(5) site is vacant and O(4) is fully occupied. For this stoichiometry, the unit cell dimensions are a=3.8227(1) Å, b=3.8872(2) Å, and c=11.6802(2) Å[102]. For a lower oxygen content, the O(4) occupancy decreases and O(5) increases, until both reach an equivalent 20% occupancy at

δ=0.65, wherein the crystal becomes tetragonal[102]. As the oxygen content is decreased further, the occupancy of the now equivalent O(4) and O(5) sites drop, and for δ=1.0, both positions are unoccupied.

Single crystals of $YBa_2Cu_3O_{7-\delta}$ were grown using the self-flux method[103]. The process begins with the mixing of 99.99% Y_2O_3, 99.99% $BaCO_3$, and 99.99% CuO to a ratio of 1.00:9.59:9.45, which is equivalent to a Y:Ba:Cu ratio of 5:27:68. The mixture is pulverized for approximately an hour, using an agate mortar and pestle, achieving a fine gray mixture. Small pellets of diameter ~1/2" and mass ~7 grams are formed by pressing the material under a pressure of 3000 lbs. A single pellet is placed in the center of a gold boat, which has a raised center to enhance the flow of the mixture, which exists in a partial liquid form between 935 and 1000° C. The pellet and boat are then heated, in air and at atmospheric pressure, in temperature steps of 120° C/hr to a maximum temperature of 985° C. The furnace is maintained at this temperature for 1 1/2 hours, and then the temperature is lowered at a rate of 1° C/hour, down to 880° C. The cooling rate is a critical feature in the growth of the crystals[104]. The crystals are formed during this slow-cooling stage, with some of the crystals forming at the surface of the pellet, and others forming in the liquid which has puddled in the bottom edges of the boat.

After cooling to room temperature, the crystals are harvested from the flux. The best crystals, identified by their clean rectangular platelet shapes are usually found in the corners and edges of the boat, and also in proximity to the melted pellet. The resultant batch usually contains 5-10 rectangular single crystals on

the order of 1(w) x 1(l) mm in the ab plane, and a thickness ranging from 20-200μm, as well as 20-30 smaller crystals. In order to achieve optimally high superconducting transition, the crystals undergo a post anneal in flowing oxygen (at 1 atm) at 410° C for ten days. This elevated temperature enables oxygen diffusion into the crystal.

After annealing the crystals typically display a T_C ~93 K, but contain planar defects in the form of twin boundaries (see Figure 6.4). These naturally occurring, quasi-two dimensional structures are the result of the tetragonal-to-orthorhombic phase transition which it underwent near 680° C in the growth process. The tetragonal phase consists of an equal distribution of the O(4) and O(5) sites. At the transition to the orthorhombic phase, oxygen atoms in the O(5) position move to the O(4) sites, resulting in the Cu-O chain structure along the b axis shown in Figure 6.1. This produces an increase in the length of the lattice parameter b, and a subsequent distortion strain in the basal plane[103]. The strain is taken up by the formation of twin boundaries which are strain fields along the <110> and <110> direction and act as sinks for atomic displacements and oxygen vacancies in the crystal. The twin boundaries in the as-grown crystals can be viewed with a polarized light microscope, where they separate two different colored regions where the basal plane is rotated by 90 degrees, as shown in Figure 6.4.

Twin boundaries act as highly anisotropic defect planes. For our studies, it is necessary to isolate them from other defects which we artificially induce by irradiation. This is done via the application of uniaxial pressure in the ab

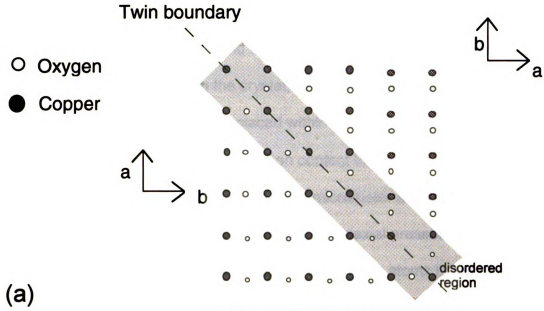

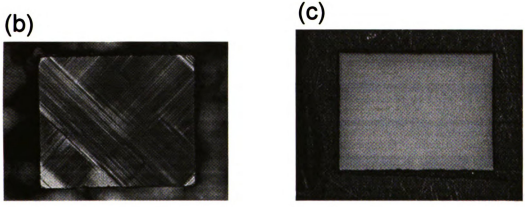

Figure 6.4 Twin boundaries in YBCO. (a) Schematic of twin plane. (b) A twinned crystal. (c) A twin-free crystal.

plane[105, 106]. The crystal is placed within a detwinning device where uniaxial pressure is applied with a spring and adjusting micrometer, see Figure 6.5. A section of the device containing the crystal, sandwiched between two quartz plates with a soft gold leaf buffer is placed within a furnace and heated to 420° C in flowing oxygen to ensure that the oxygen content in the crystal does not vary during the detwinning process; the spring and micrometer are kept outside the furnace and cooled with flowing air. The applied uniaxial pressure is typically of the order of ~10^7 N/m. The pressure causes the oxygen atoms in the direction of the uniaxial pressure to move to the transverse direction and consequently leaves the uniaxial pressure direction to form the shorter crystallographic a-axis and the transverse direction becomes the longer b-axis. This alignment of the a and b axes throughout the entire crystal eradicates the twin boundaries. The removal of twin boundaries takes minutes to achieve under the appropriate pressure and heat. However, it is important to continue the process ~24 hours after the crystal appears fully detwinned, in order to allow the crystal to come to equilibrium. The superconducting transition temperature is usually unaffected by this detwinning process. These detwinned crystals invariably exhibit a very sharp first order vortex lattice to liquid melting transition, usually observed as a sharp 'kink' in the resistivity in the presence of a magnetic field.

For heavy ion irradiation experiments, these crystals must be thinned to less than 30 μm along the c-axis, in order to ensure that the heavy ions produce continuous and straight defect tracks throughout the sample. A crystal is thinned by mounting it with crystal bond onto a metal holder along with small glass plates

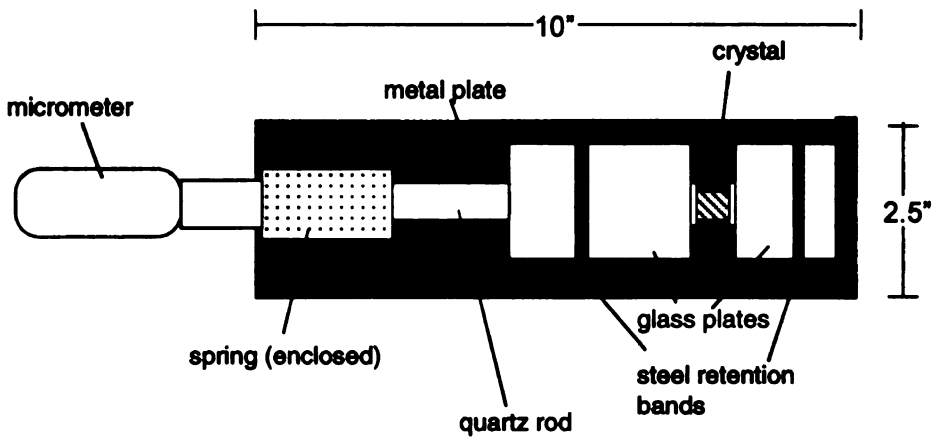

Figure 6.5 Detwinning device.

to support the crystal edges and then grinding it, using 1-30 μm grit polishing discs and diamond-in-oil suspensions. Since the glass is harder than the crystal, it provides a support along the crystal edges, as well as providing a horizontal polishing plane. Final polishing is conducted using 0.1 μm diamond suspension. With this method, flat millimeter sized crystals less than 20 μm thick with no discernible scratches down to a scale of 0.1 μm can be obtained.

Transport measurements are conducted using the standard four-probe technique. One of the challenging aspects of this type of measurement on single crystals is the fabrication of low resistance contacts. Using an evaporation chamber, the sample surface is first cleaned with argon gas plasma etching. Four gold contacts, approximately 2000 Å thick, are then deposited on the crystal by gold evaporation through a metal mask. As deposited, the gold contacts have high resistances. Hence the gold contacts are subsequently sintered at 410° C in flowing oxygen for approximately six hours to ensure good bonding of the gold to the ceramic crystal surface. Half mil annealed gold wires are attached to the

gold pads using Epo-TeK H20E silver epoxy, then cured for 5-10 minutes at relatively low temperatures, usually around 150° C, resulting in final contact resistances of about 1 Ω or less.

Chapter 7

EXPERIMENTAL SETUP AND HEAVY ION IRRADIATION

7.1 System configuration

(7.1.a) Cryogenic and Superconducting Magnet System

The cryostat (Figure 7.1) is a home built ^{3}He system capable of achieving temperatures as low as 0.47 K, but adapted for use in our experiments with ^{4}He. The dewar used in conjunction with the cryostat is a superinsulated design built by Precision Cryogenics, and fabricated mainly of aluminum with a 12 inch G-10 neck. The main sections of the ^{3}He cryostat are shown in Figure 7.1. It is a top loading system, with a sample chamber diameter of 0.75". The midsection of the sample chamber is surrounded and in contact with a 1 K pot which can hold 1 liter of liquid helium, used mainly for low temperature experiments below 1 K. The tail of the sample chamber is constructed of non-magnetic stainless steel and extends approximately 12 inches below the 1 K pot, enabling the tail of the cryostat to be thermally isolated from the 1 K pot when used in the ^{3}He mode. Both the sample chamber and the 1 K pot are isolated from the liquid helium bath by an inner vacuum can. Two superconducting magnets surround the tail of the cryostat: A 1.5 Tesla transverse split coil NbTi superconducting magnet which resides in the 2.75" diameter bore of an 8.0 Tesla longitudinal superconducting magnet. The two superconducting magnets supply the two orthogonal fields, which can be programmed to give a desired resultant vector field. Each superconducting magnet is controlled with a Lakeshore Cryotronic Model 622

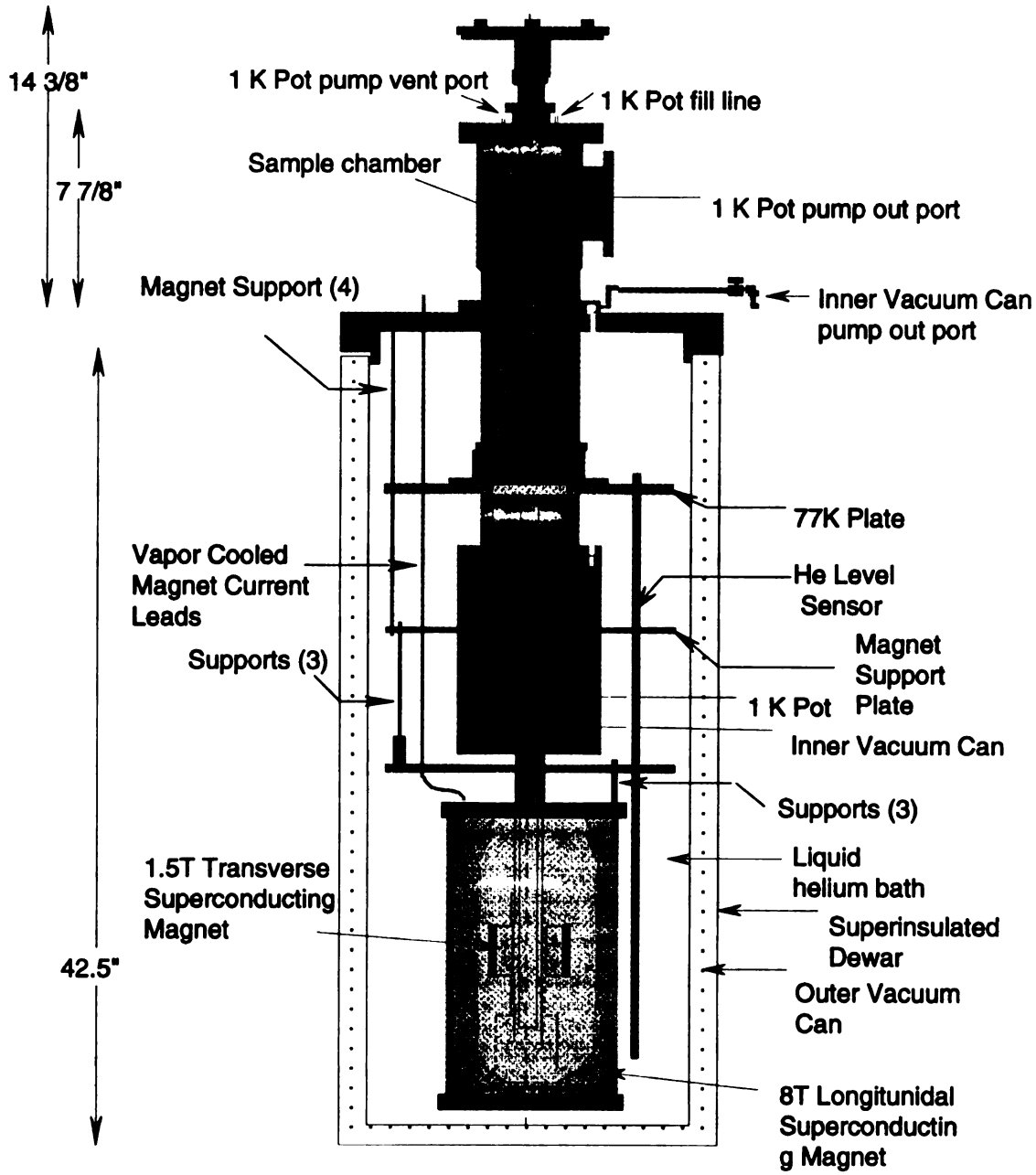

Figure 7.1 ^{3}He, ^{4}He cryostat system.

power supply capable of delivering 120 A at up to 5 V. The current through each magnet is independently monitored by a Keithley 196 digital voltmeter connected across a copper shunt (0.001Ω), which is in series with the magnet high current cables. The following steps define the cooling operation down to about 0.47K using ^{3}He as an exchange gas in the sample chamber. The sample chamber, inner, and outer vacuum cans are evacuated with a rotary pump/diffusion pump system to about ~10^{-6} torr (see Figure 7.2). The bath of the dewar is then filled to capacity with liquid nitrogen to pre-cool the superconducting magnets. Subsequently, the liquid nitrogen is removed by supplying a back pressure of nitrogen gas. When all the liquid is displaced, the bath is flushed several times with ^{4}He gas to ensure that no liquid nitrogen remains at the bottom of the dewar. Next, the bath is filled with liquid ^{4}He to capacity. The 1 K pot is then filled with liquid ^{4}He through a supplied transfer line and the sample chamber is filled with ^{3}He gas to about 400 mtorr. By pumping on the 1 K pot through a large rotary pump, and thereby reducing the vapor pressure of liquid ^{4}He, the temperature in the 1 K pot falls to about 1.19 K, allowing the ^{3}He gas to first condense at the inner wall of the sample chamber where it contacts the 1 K pot. The condensed liquid then drips down and collects at the bottom of the sample chamber. Sufficient ^{3}He gas is introduced into the sample chamber to completely immerse the sample with liquid ^{3}He when the gas is condensed. By pumping on the liquid ^{3}He, we can reduce the vapor pressure of the liquid and the temperature decreases to about 0.47 K. For the data presented in this thesis, the system is operated using liquid ^{4}He: The sample chamber is filled with ^{4}He gas to a

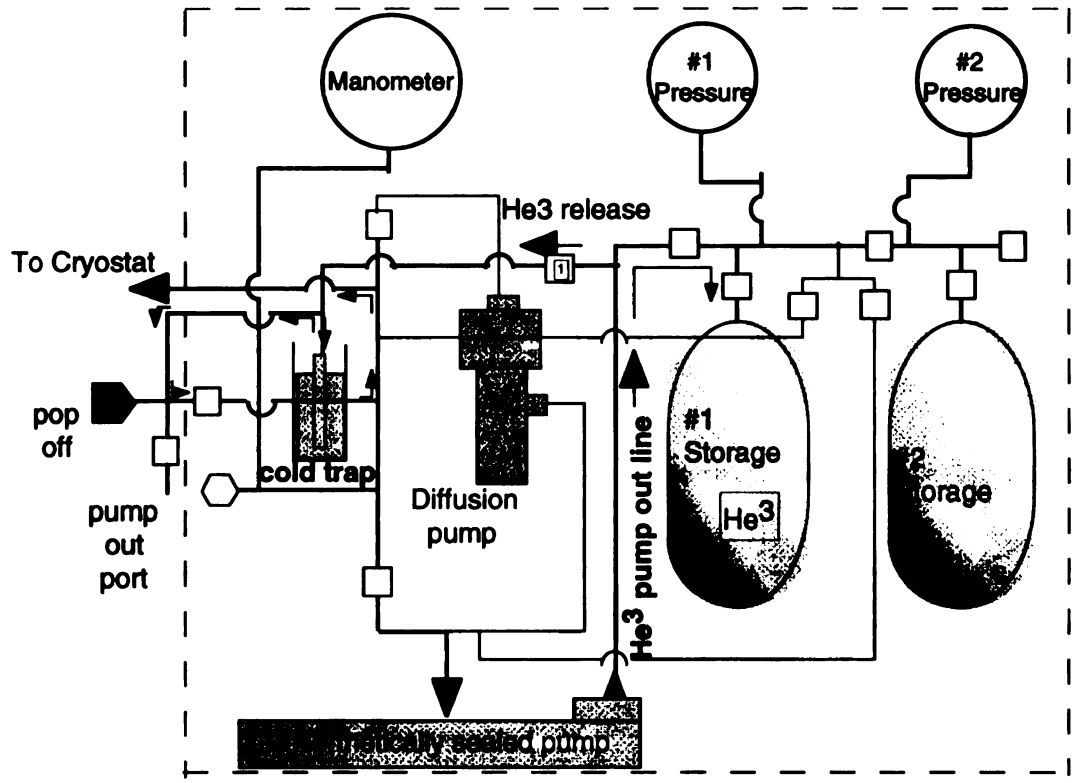

Figure 7.2 Gas handling system.

pressure of ~100 mm Hg. The 1 K pot is filled with ^{4}He gas, and cooling occurs via conduction and radiation from the liquid ^{4}He in the bath. Temperature control is maintained locally by a non-inductively wound phosphor bronze heater wire wrapped around a copper cap which surrounds the sample.

(7.1.b) Sample Probe

The sample probe consists of a long G-10 (fiberglass reinforced plastic) tube interrupted with two OFHC copper heat sinks located in positions such that they are in contact with the top and bottom of the 1 K pot (see Figure 7.3(a)). The tail of the resistivity probe (Figure 7.3(b)) consists of a Lakeshore Cernox thermometer calibrated from 300K to 0.33 K, a standard T08 eight pin IC socket

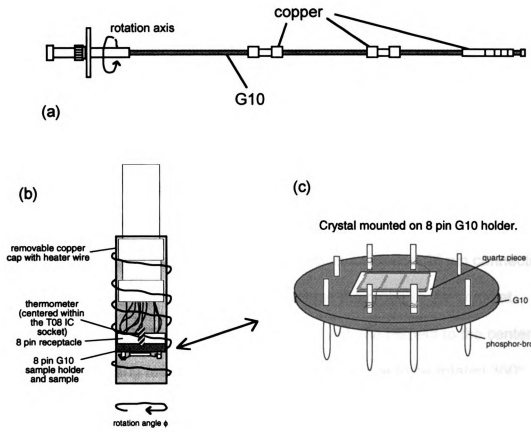

Figure 7.3 (a) Sample probe used to insert the samples in the cryostat. The probe can be rotated about its long axis. (b) Expanded view of the probe end. The sample is located at the bottom of the figure. A thermometer is located close to the underside of the sample holder. Also shown is the copper cap used to control the local temperature. (c) View of sample and sample holder. Here four contacts are shown, with gold wires connecting the contacts to the pins.

for the sample, and a cap heater consisting of an OFHC copper cap wrapped non-inductively with 36 gauge Phosphor Bronze heater wire.

To facilitate quick sample exchanges, we developed a removable sample holder to fit in the IC socket (Figure 7.3(c)) for four-probe resistivity measurements. The sample holder consists of a G-10 disk with either four or eight Phosphor Bronze posts which fits the IC socket. For resistivity measurements the YBCO single crystals are typically mounted on a sapphire

substrate with silver epoxy on both ends of the sample which also serves as the current contacts. The sapphire substrate with the sample is then mounted onto the G-10 disk with GE varnish. Contacts from the sample to the posts are made with 0.5 mil annealed gold wire which are attached with silver epoxy to the sample, and attached to the posts with indium solder. The G-10 disk with the sample plugs into to the 8 pin IC socket at the bottom of the probe. Connection from the sample to the top of the probe is made with 24 twisted pairs of 38 gauge copper wire, terminating at a hermetically sealed Amphenol 26 pin connector at the top. An O-ring slip connection, which mates the probe to the cryostat, enables the height of the probe to be adjusted with the respect to the center of the superconducting magnets and also allows the probe to be rotated 360°. This latter capability allows an extra degree of sample orientation with respect to the transverse magnetic field provided by the 1.5T superconducting split coil magnet.

Temperature is controlled by a Lakeshore Cryotronics DRC-93A temperature controller connected to the Cernox thermometer and with the Phosphor Bronze heater wire wrapped around the OFHC copper cap as shown in Figure 7.3(b).

(7.1.c) Electronics

A schematic diagram of the standard four probe geometry for measuring the ac resistivity is shown in Figure 7.3(c). AC current is generated with a Wavetek Model 90 function generator, in series with a 1 kΩ resistor which enables the function generator to provide a constant current source to the sample in a

transport measurement as long as any changes in the resistivity of the sample upon cooling remain much smaller than 1 kΩ. An additional 0.1 Ω resistor in series with the sample is used to monitor the sample current. The sample voltage and current (measured across the 0.1 Ω resistor) leads are each connected to a Stanford Research model 554 transformer which acts as a step up 1:100 isolation pre-amplifier. These transformers are then connected to Stanford Research 830 lock-in amplifiers.

For DC resistivity measurements, the function generator and the associated resistors are replaced with a single Keithley model 220 current source and the DC voltage is measured using a Keithley 182 nanovoltmeter, making sure to reverse the current direction several times to avert thermal drift voltages.

The data acquisition system consists of a UMAX (Apple clone) desktop computer connected with the laboratory instruments via an IEEE 488.2 GPIB interface, running either C++ or LabView data acquisition programs.

7.2 Heavy ion irradiation

The superconducting coherence length, for $YBa_2Cu_3O_{7-\delta}$ crystals for fields parallel to the crystallographic c-axis at zero temperature, is approximately $\xi_0 = 16$ Å[107]. Since the coherence length varies with temperature as $\xi \approx \xi_0 / (1-T/T_C)^{1/2}$, the coherence length for YBCO varies from ~ 16 to 100 Å throughout most of its superconducting temperature range, up to ~$0.98T_C$. This length is a measure of the radius of the normal vortex core. In the creation of the

nonsuperconducting core, the free energy per unit length increases by the vortex condensation energy:

$$\frac{1}{8\pi}\int h^2 dA = \frac{H_c^2}{8\pi}\pi\xi^2 \qquad (7.1)$$

Since this is the energy to suppress the superconducting state within the core, any nonsuperconducting defect would act to pin the vortex line at the defect, since some of the condensation energy would then be conserved. A favorable pinning site will be a nonsuperconducting column of defect material, aligned with the vortex line, with a diameter comparable with the vortex core size. Such columnar defects can be produced by high energy heavy ion irradiation of the crystals. Magnetization[108, 109], and transport[44, 110, 111] data have shown sharp increases in the critical current, as well as an upward temperature shift in the irreversibility line in YBCO, as a result of heavy ion irradiation. So far, these defects produce the most effective pinning sites in YBCO[84].

Columnar defects are created in YBCO by the impingement of high energy ions, which traverse the thickness of the crystal, producing defect tracks (see Figure 7.4). In order to produce these defects in a linear column geometry, the ions must have enough energy to pass completely through the sample with only negligible stray from the bombardment direction, as well as transfer enough energy to the material to create the track; this energy is defined as the stopping power, dE/dx. The energy transfer from the ion, moving at velocity v, to the target material occurs via nuclear scattering and electronic interactions, which

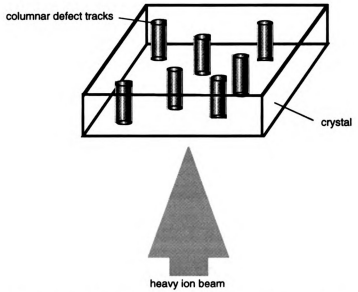

Figure 7.4 The creation of columnar defect tracks via heavy ion irradiation.

can be calculated using Monte Carlo calculations[112, 113]. The ion energy loss per unit length is given as the combination of the two types of processes:

$$dE/dx = dE/dx)_{nuclear} + dE/dx)_{electronic} \quad (7.2)$$

where $dE/dx)_{nuclear}$ describes ion-atomic elastic scattering collisions, characterized by large deflections and energy losses per collision, and $dE/dx)_{electronic}$ describes the interaction of the ion with the electronic structure of the target, characterized by small ion deflections and energy losses per collision. These are commonly referred to as the nuclear and electronic stopping power S_n and S_e. They depend not only on the ion type and energy, but also on the target material. For high ion energies (> 200 keV/amu), S_n can be neglected relative to the size of S_e. For the high energy ions, the electronic stopping power S_e is

calculated by treating the solid as a charged electron plasma, with a charge density ρ that varies with position. The interaction between the electron plasma and moving ion is calculated using the Lindhard particle-plasma interaction function $l(v, \rho)$, which relates the interaction of the ion, velocity v, with the electron distribution function, integrated over all wavelengths. The density is convoluted with $l(v, \rho)$, and the heavy ion's *effective* charge $Z^*(v, Z_i)=Z\,\gamma(v,Z_i)$, where Z is the ion atomic number, Z_i is a target atom atomic number, and γ is the fractional effective charge of the ion:

$$S_e = \int l(v,Z)\,(Z\,\gamma(v,Z_i))^2\,\rho\,dV \qquad (7.3)$$

The ion is said to be effectively stripped of a (target material dependent) fraction γ of its total electrons due to the interaction of the outer shell electrons with the material.

For heavy ions, the stopping power is calculated in the following way: The predictions of equation (7.3) are compared to experimental data for hydrogen and helium ions. From this comparison, eqn. (7.3) is corrected to give more accurate predictions. Thus a resultant *empirically corrected* electronic stopping function is obtained. Finally, for heavy ions, a scaling procedure is applied, where the heavy ion stopping power is related to the hydrogen stopping power in the same material:

$$S_{\text{heavy ion}} = S_{\text{hydrogen}}\,Z^2_{\text{heavy ion}}\,\gamma^2 \qquad (7.4)$$

The resulting predictions have been shown to be accurate to within 10% of actual results.

The effect of high energy heavy ion irradiation in YBCO is calculated using the Transport of Ions in Matter (TRIM) Monte Carlo calculation program[114]. This program takes as inputs the ion type, its initial energy, and the target material, producing a statistical distribution of the final ion penetration depth and energy transferred to the target material (*ion energy loss per unit length*) along the ion path. This energy is the stopping power $S=S_n+S_e$, in units of eV / Å. A typical distribution includes over 5000 ion simulated trajectories. The program assumes a random distribution of target atoms, with a density of 6.54 g/cm^3 for YBCO in the fully oxygenated state. Figure 7.5 shows TRIM calculations for three ions, Au, U, and Pb, at varying initial energies, for a YBCO target. The figure plots the stopping power (ion energy loss per Angstrom) of the impinging ion, as a function of target depth. The ion energies in the figure are for the ions before entering the material. As the ion transfers energy to the target, its energy is lowered, thus changing the prediction of the stopping power.

The process of columnar defect track formation is described by the ion explosion spike model[115-117]. As the high-energy ion traverses the superconductor, it has been found to interact almost exclusively with the electrons, causing local ionization along the path. The atoms remaining within the now electron-depleted region are thus affected by a net repulsive force and, if this force is greater than the atomic bond strength, the atoms are displaced along the path, as shown schematically in Figure 7.6. In this manner a cylindrical region of defects is established. In order to produce an effectively continuous path of defects, certain criteria must be satisfied. The number of ionizations must

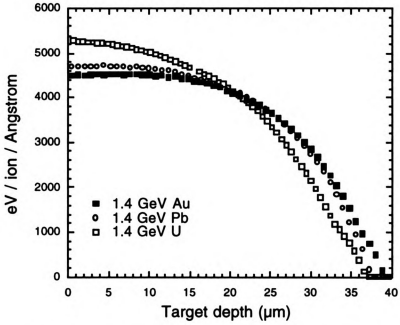

Figure 7.5 Stopping power for U, Pb, and Au in a YBCO target.

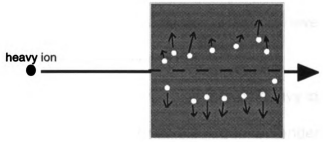

Figure 7.6 Defect Formation: Atoms (white circles) are first ionized by the ion, then mutually repulsed from the electron depleted region.

be at least one per ab-plane, with an energy transfer high enough so that the net ion repulsion will be greater than the atomic bond strength. The mobility of the created defects must be less than an interatomic distance, otherwise the defects created would disperse over time. It must also be possible to deplete the region of electrons for enough time as to allow the atoms to repulse one another. This last criterion is not satisfied for most metals, excepting for those with a density of conduction electrons less than $10^{20}/cm^2$[115].

A concern in the production of 'straight' columnar defects is the stopping power. From electron microscopy measurements, a lower bound S_m in the stopping power has been established for the production of continuous defect tracks. Szenes[118] examined thirteen data on YBCO, obtaining $S_m \approx 1900$ eV / Å for this minimum stopping power, in agreement with other work[119, 120]. Data on 0.58 GeV Sn[121] and 2.29 GeV Xe[122] finds somewhat higher values for this threshold, S_m >28 eV / Å and 23 eV / Å, respectively. For stopping energies below the threshold, aligned spherical defects have been produced instead of continuous columnar defects[121].

Our crystals were irradiated with high energy heavy ions at two facilities: The 36" diameter ATSCAT chamber at the Argonne Tandem Linear Accelerator System (ATLAS), located at Argonne National Laboratory, and the N3 chamber at the National Superconducting Cyclotron Laboratory (NSCL) at Michigan State University. The basic chamber configuration is shown in Figure 7.7. The samples are placed on a ladder mount which is located at the center of the chamber on a rotatable table which is also capable of raising and lowering the

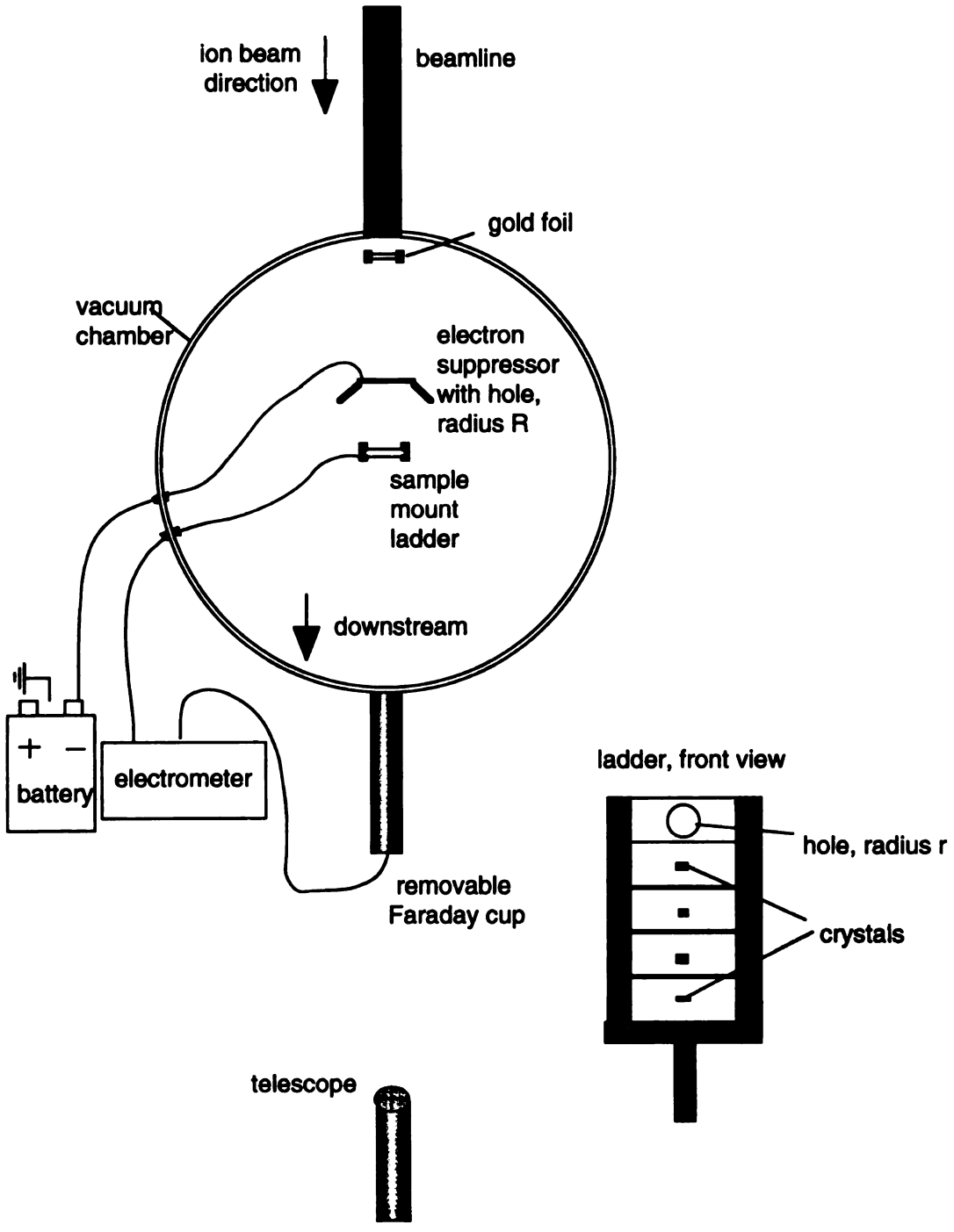

Figure 7.7 Heavy ion irradiation vacuum chamber, orientation, and sample ladder.

sample. The ladder mount consists of several rectangular aluminum plates which are stacked vertically on top of one other. Samples are mounted onto the aluminum plates, except for the topmost plate, which contains a fixed diameter hole drilled into the plate. This hole is used to align the beam on the ladder and is also used as the reference diameter of the beam (i.e. the beam size is adjusted by the beam controller such that the entire beam barely passes through this hole). A telescope located outside the chamber and downstream from the beam tube is used to align the sample with the beam direction and record the position of each sample on the ladder. After the alignment is completed, a Faraday cup is placed at the back end of the chamber and connected to an electrometer to measure the beam current. This 'downstream' Faraday cup is used to record the beam current through the hole on the ladder mount. During irradiation, the beam current impinging on the samples on the ladder is also monitored with an electrometer. Heavy ions striking the samples with over 1 GeV of energy produce ejection of surface electrons from the target. To counter this effect and to obtain an accurate record of the beam current, a -300V suppressor plate with a collimator hole is placed in close proximity in front of the target samples. For the high energy ions used in the irradiation, the mean ejected electron energy from the target is on the order of 250 eV[123]. Thus the negative charge of -300V at the suppressor plate is enough to repel the electrons back onto the target. Monitoring the beam current on the conducting suppressor plate can assist the beam tuner to steer the beam onto the target. The downstream Faraday cup is geometrically suppressed, i.e. any ejected electrons

will be collected by the long cylindrical wall of the cup, thereby yielding an accurate reading.

One of the main issues in using heavy ion irradiation to create columnar tracks is the control of the irradiation dose which depends heavily on the stability and uniformity of the beam intensity. In most high energy heavy ion accelerators, the beam energy can be controlled to a high degree of accuracy. However, the beam intensity and the homogeneity of the beam over a few millimeter square region can vary dramatically during the time it takes to irradiate a single sample. One technique to homogenize the beam pattern is to place a thin gold foil in front of the beamline. The foil acts to diffuse the beam via Rutherford scattering and eliminate possible hot spots within the spatial profile of the beam. The beam profile can be checked by exposing a piece of Gafchromic™ radiographic film for a few seconds (see Figure 7.8). These films are sensitive to ion irradiation, and change from a light blue hue to a dark blue color after exposure to ion irradiation. If the beam is spatially inhomogeneous, a hot spot indicating a very high dose section of the beam will appear as a reddish 'burn' mark on the film.

After sample alignment has been completed, the chamber is closed and pumped down to ~10^{-6} torr. The heavy ions enter the chamber in a stripped state, with a net positive charge. Electrons are further stripped as the ions traverse through the gold foil. The charge state can be calculated for a given ion energy[124].

Given the final ion charge Q, the beam flux can be calculated in the following manner: The beam is adjusted such that the entire beam barely passes

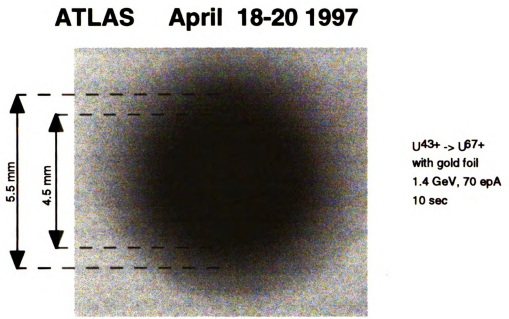

Figure 7.8 Radiographic film image.

through the hole with radius r on the topmost plate of the ladder, and the current I_{FC} is measured by the downstream Faraday Cup. The ion flux F, defined as the numbers of ions per cm^2 per second, is obtained from this current:

$$F = I_{FC} \bullet (1\text{charge}/1.6\text{x}10^{-19}\ \text{C}) \bullet (1\ \text{ion/charge Q}) / (\pi r^2) \qquad (7.5)$$

The columnar defect density n is chosen to be equivalent to a matching vortex density B_Φ,

$$n = B_\Phi/\Phi_0 \qquad (7.6)$$

where $\Phi_0 = 2.07 \times 10^{-15} T/m^2$ is the flux quantum and B_Φ is in units of Tesla. The time of irradiation, t, to obtain a specific matching field B_Φ is given by:

$$t\ (\text{sec}) = (B_\Phi/\Phi_0) \bullet (\pi r^2) \bullet Q \bullet 1.6 \times 10^{-19}\ \text{C} / I_{FC} \qquad (7.7)$$

The beam is monitored using an alpha particle detector, pointed towards the gold foil at a fixed angle from the beam direction. Thus the detector counts

the elastically (Rutherford) scattered particles allowing for the calculation of the beam current intensity at off-angles from the beam direction. The detector output is a voltage pulse proportional to the alpha particle incident energy. Figure 7.9 shows the detector and the electronics. An incident particle produces electron-ion pairs within the particle detector. The bias voltage acts to collect the free electrons before they recombine. The signal is amplified, and the single channel analyzer (SCA) converts all of the voltage pulses above a threshold into constant amplitude voltage pulses, which can then be measured by the counter. The measured counts per unit time is proportional to the beam current. Besides calculating the predicted particle counts for a given beam intensity from Rutherford scattering off the gold foil we can also obtain the corresponding conversion from actual beam current to off-angle detector counts by measuring the alpha detector counts and the downstream Faraday cup current simultaneously for one minute. The average current on the Faraday cup is first converted to equivalent irradiation dose B_Φ(1min), using eqn. (7.7). The number of counts measured is then defined as being equal to B_Φ. To obtain a necessary dose B_Φ, the crystal is irradiated until the counter measures the corresponding number of counts needed to attain B_Φ, i.e., #counts(B_Φ) = #counts(1min) • B_Φ / B_Φ(1min).

For the heavy ion irradiation experiment, three large untwinned $YBa_2Cu_3O_{7-\delta}$ single crystals, each < 20 μm thick, were grown using the self-flux method, described earlier. Two of the crystals were each cleaved down the c-axis into four smaller pieces using a clean razor blade and the third crystal was

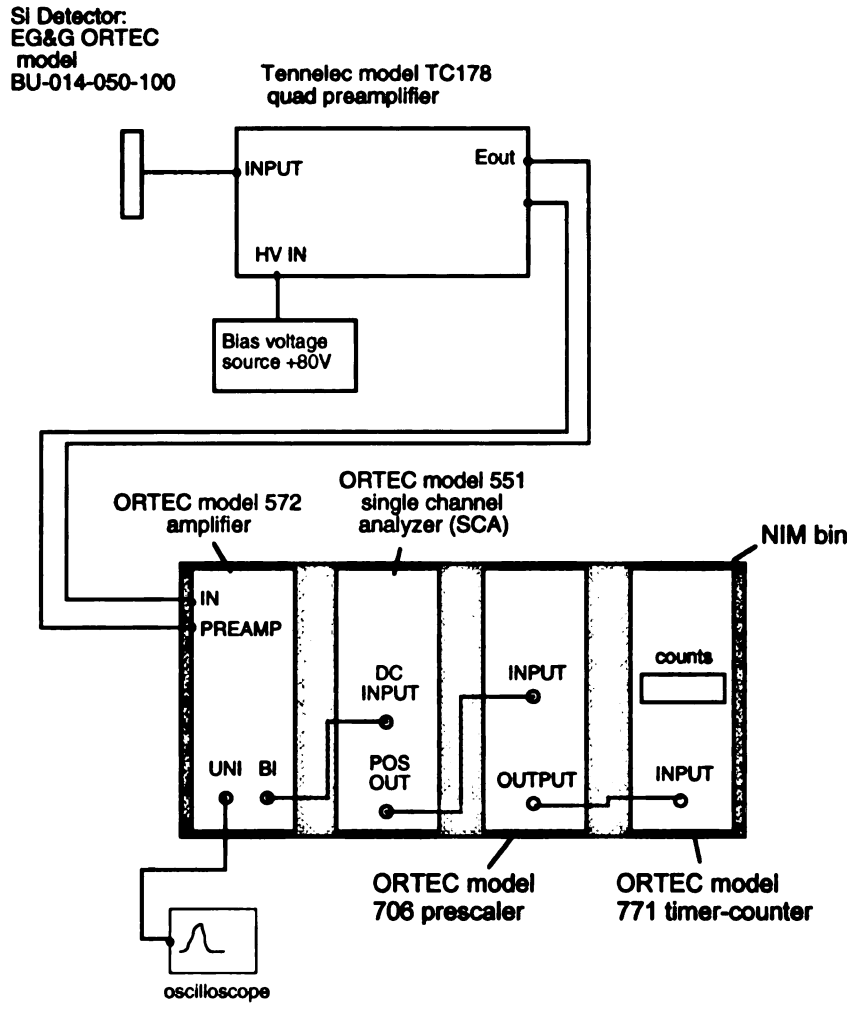

Figure 7.9 Alpha particle counting electronics

cleaved into five pieces. This approach ensures that each of the pieces for irradiation will have the same underlying starting quality. One piece from each large cleaved crystal was kept as an unirradiated reference. The crystals were irradiated with 1.4 GeV $^{238}U^{67+}$ and 1.4 GeV $^{208}Pb^{56+}$ ions at ATLAS, to a dose matching field B_Φ = 1, 2, and 4 Tesla for the uranium ions, and B_Φ = 50 Gauss, 100 Gauss, 500 Gauss, 1000 Gauss, and 1 Tesla for the lead ions. The stopping powers for these ions and incident energies are presented in Fig. 7.5. Resistivity vs. temperature data for the crystals irradiated with high doses is shown in

Figure 7.10, for zero applied field. The data shows an increase in the normal state resistivity, a decrease in T_{Co}, and broadening of the transition ΔT_{Co} with increasing irradiation dose. For this work, T_{Co} is defined as the peak in the derivative $d\rho/dT$ (Fig. 4.4), and ΔT_{Co} is defined as 90%-10% of ρ_{normal}, where ρ_{normal} is the resistivity at the onset of the peak in the derivative. These results are summarized in Table 7.1.

Table 7.1 Columnar defect tracks in YBCO.

Crystal	T_c (K)	T_c/T_c(unirrad)	δT_c (K)	ρ(95K)/ρ(unirr,95K) (approximate)	Calc. defect separation (Å)	Measured defect core (Å)
PbO (0T)	93.83	1	0.28	1	-	-
Pb1 (1T)	92.57	0.987	0.46	1.13	458	~70-96
U0 (0T)	92.59	1	0.38	1	-	-
U1 (1T)	90.79	0.98	1.20	1.14	458	90
U2 (2T)	89.67	0.968	1.95	1.90	324	90
U4 (4T)	88.0	0.95	3.40	2.86	229	90

The defect track information was obtained from electron microscopy measurements (Figure 7.11). For the 1.4 GeV Pb ion defects the 70-96 Å value in Table 7.1 was estimated from High Resolution Electron Microscopy (HREM) measurements on YBCO samples irradiated with 0.9 GeV Pb ions[111] and 1.1 GeV Au ions[125]. This diameter agrees with other TEM measurements on YBCO crystals irradiated with 1.08 GeV Au ions[84, 126, 127], which found continuous homogeneous defects, with a diameter of 60-70 Å. The stopping powers shown in Figure 7.5 are comparable for the Au and Pb ions at equivalent

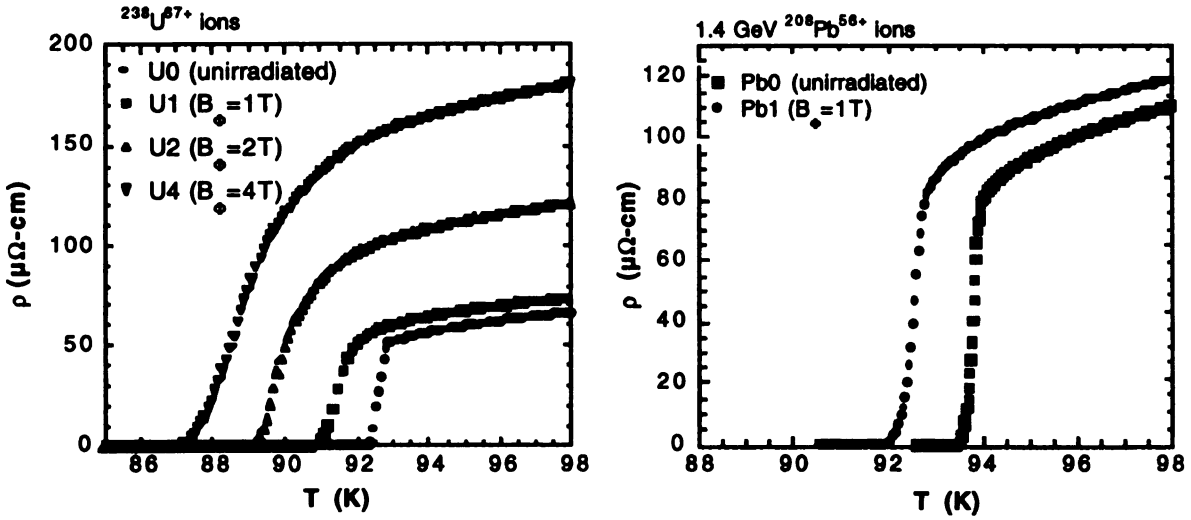

Figure 7.10 Resistivity versus temperature data in zero field.

ion energies; since the two ions are nearly the same mass, comparable track formation is expected.

TEM measurements on tracks in YBCO produced by 1.3 GeV U ions have been performed[122]. From this and other work[128, 129], a more complex picture of the damaged tracks has emerged, in which three types of damaged regions have been observed: At the center of the defect is the amorphous core region, d ≅ 10 nm. Beyond the core is an oxygen-reordered region extending approximately 10 nm around the core, and an extended stressed region, which extends up to 30 nm further beyond the core. Within the extended stressed region, 'nanotwin' structures may form between two defects when they are within 50 nm of one another. However, angle dependent measurements of the resistivity of the uranium irradiated crystals failed to record any anisotropic pinning due to the nanotwins. The net conclusion is that the effective damage

radius extends beyond the core, although it is unclear whether this affects the pinning behavior of the defects.

Also, recent data on 2.25 GeV Au[122] and 1.1 GeV Au ions[125, 130] show significant defect core diameter modulation (4-11 nm for the 2.25 GeV data) in measurements at varying depths. TEM measurements on 1.3 GeV U irradiated crystals (S>50 eV / Å) did not show this modulation, thus it is as yet unclear if this occurs in the 1.4 GeV Pb (S≈47 eV / Å) irradiated crystals.

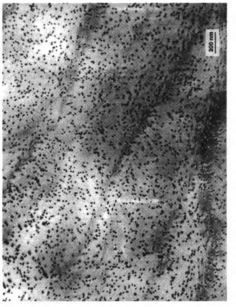

Figure 7.11 TEM image of columnar defects in YBCO, looking along the defect direction. Defects were created by 1.3 GeV uranium ions.

Chapter 8

THE EFFECT OF HIGH DENSITIES OF COLUMNAR DEFECTS ON VORTEX MOTION IN CLEAN, UNTWINNED $YBa_2Cu_3O_{7-\delta}$ SINGLE CRYSTALS

8.1 Introduction

The motion of vortices in $YBa_2Cu_3O_{7-\delta}$ can be dramatically affected by the bombardment of high energy, heavy ions, which produce amorphous defect tracks through the sample. These columnar defect tracks produce anisotropic pinning centers which are energetically favorable pinning sites for vortex lines. The result is significant vortex pinning in the vortex solid state and the slowing down of vortex dynamics in the vortex liquid state. The nature of the vortex melting transition is also altered by the defects. In the presence of columnar defects the melting transition is predicted to be a continuous, Bose glass transition[86, 87]. Unlike isotropic defects which are responsible for a purported Vortex Glass transition[22, 29], the Bose glass transition predicts a sharp cusp in the transition temperature as the applied field is rotated about the columnar defects, clearly discerning it from the isotropic pinning case.

For very clean $YBa_2Cu_3O_{7-\delta}$ (YBCO) single crystals, in the absence of correlated disorder, a first order melting transition has been found in transport measurements[32, 131] and confirmed by magnetization[38-40] and specific heat[41] measurements. In transport measurements, a sharp drop, or 'kink' near the tail of the resistivity curve measured in a magnetic field has been associated with the first order melting transition. For crystals with a significant number of either point or correlated defects, the first order transition transforms into a

continuous transition, with the transition predicted to be either to a Bose glass, vortex glass, or polymer glass (vortex molasses), depending on the type of defects induced into the sample.

Several experiments purporting to demonstrate the existence of these phases have been reported. However, earlier experiments have been plagued by inherent defects such as twin boundaries in the as grown sample leading to some ambiguity as to the nature of the glassy phase. In many cases, what was reported as a vortex glass phase[20, 132, 133] in twinned YBCO thin films and crystals may in fact be related to a Bose glass phase due to the existence of correlated defects in the samples[134]. Twin boundaries can behave as correlated defects, and introduce added complications in transport measurements due to such phenomena as guided motion of the vortices parallel to a twin plane[135, 136]. A number of earlier studies on YBCO crystals with columnar defects induced by heavy ion irradiation were also performed on twinned crystals, compounding the difficulty in separating the behavior of vortex localization by columnar defects from twin boundary pinning. Thus a definitive investigation of the Bose glass transition in YBCO is still lacking.

In this chapter, we investigate the melting transition in pristine untwinned YBCO crystals in the presence of columnar defects created by Pb and U ions, and compare the results with the predictions of the Bose glass theory. We determine the static and dynamic critical exponents ν and z, respectively, associated with the Bose glass scaling theory and show direct evidence of the

anisotropic pinning nature of the columnar defects. In addition, we find a systematic kink in the irreversibility line which tracks the defect matching field.

Single crystals of YBCO were prepared using the flux growth method described elsewhere[103]. The as grown and annealed crystals were detwinned by applying uniaxial pressure along one side of the ab-plane at 420° C in flowing oxygen and then polished down along the crystallographic c-axis to less than 30μm to ensure that the heavy ions traverse through the entire cross-section of the sample according to TRIM calculations[112]. No vestiges of twins were observed by polarized microscopy after detwinning.

Three large detwinned crystals were cleaved into three sets of several pieces. The first crystal (thickness 19 μm) was cleaved into four crystals, three of which were irradiated with 1.4 GeV $^{208}Pb^{56.4+}$ ions along the crystallographic c-axis to dose matching fields of B_Φ = 100 G(Pb0.01), 1000G (Pb0.1), and 1T (Pb1) and the fourth piece from the same crystal was kept as a reference (Pb0). The second crystal (thickness 17.5 μm) was cleaved into five pieces, three of which were irradiated in like manner with 1.4 GeV ^{238}U ions to dose matching fields of B_Φ = 1T (U1), 2T (U2), and 4T (U4) and the other two were irradiated with 4 GeV ^{297}Au ions to dose matching fields of B_Φ=1 (Au1) and 4T (Au4) at the National Superconducting Cyclotron Laboratory at Michigan State University. For this set no reference crystal was kept. Instead U1 was precharacterized before irradiation (U0). The third crystal (thickness 10 μm) was cleaved into four pieces, three of which were irradiated with 1.4 GeV $^{208}Pb^{56.4+}$ ions to dose matching fields of B_Φ=50 (Pb50G), 100 (Pb100G), 500 Gauss (Pb500G). Cleaving several

crystals from a larger piece for this experiment ensures that the starting underlying quality of the crystals prior to irradiation are equivalent. In this Chapter I will report on the crystals irradiated at high defect doses, namely Pb1, U1, U2, and U4.

Transport measurements were carried out using the standard four-probe technique. Gold contacts were first evaporated onto the surface of the crystal and sintered at 420° C. Gold wires were subsequently attached to the contacts with silver epoxy, resulting in contact resistances of about 1 Ω. AC resistivity measurements were performed with transport current densities typically in the range of 2 to 20 A/cm^2 at 23 Hz directed in the crystallographic ab-plane of the crystal. DC resistivity and I-V measurements were carried out with a nano-voltmeter with current reversal to minimize thermal effects. The crystal was placed in the bore of a 1.5 T superconducting split coil 'transverse' magnet which resides in the bore of an 8 T 'longitudinal' superconducting solenoid magnet. The magnetic field could be rotated with respect to the sample by energizing the magnets independently. For the irradiated crystals, θ is defined as the angle between the applied magnetic field and the columnar defect direction. The measuring current was always applied in the ab-plane and perpendicular to the applied field/columnar defect plane, ensuring maximum Lorentz force on the vortices for all orientations.

8.2 Uranium ion irradiation: U1, U2, and U4

The zero field resistivity data for these crystals were plotted in the last chapter, Figure 7.10. A broadening in the superconducting transition temperature width, a lowering of the transition temperature, and an increase in the normal state resistivity were observed in the irradiated crystals. Figure 8.1 shows resistivity versus temperature measurements for the U0, U1, U2, and U4 samples in applied fields of 8,7,6,5,4,3,2,1,0.5, and 0 Tesla aligned with the crystallographic c-axis. The data in Figure 8.1 has been normalized with respect to the resistivity at 95 K and T_c in order to compare the relative effects of the irradiation. Before irradiation, a 'kink' in the tail of the superconducting resistive transition associated with the first order vortex solid to liquid melting transition can be clearly observed in U0 for H = 1-8T. After irradiation, the kink has been replaced by a smooth, monotonic decrease in the resistivity, indicating that the first order transition has been completely suppressed by the irradiation and transformed perhaps to a higher order transition.

Figure 8.2(a) shows that the kink in the resistivity for the unirradiated crystal also marks the onset of non-ohmic behavior, with a sharp minimum in resistivity at ~86 K (peak effect). In contrast, the uranium-ion irradiated crystals show ohmic behavior throughout the entire superconductive resistive transition for all fields. This is clearly shown in Figure 8.2(b) for the U1 crystal where the resistivity curves measured with two different current densities lie on top of each other for all fields investigated. For these current densities, the data is ohmic

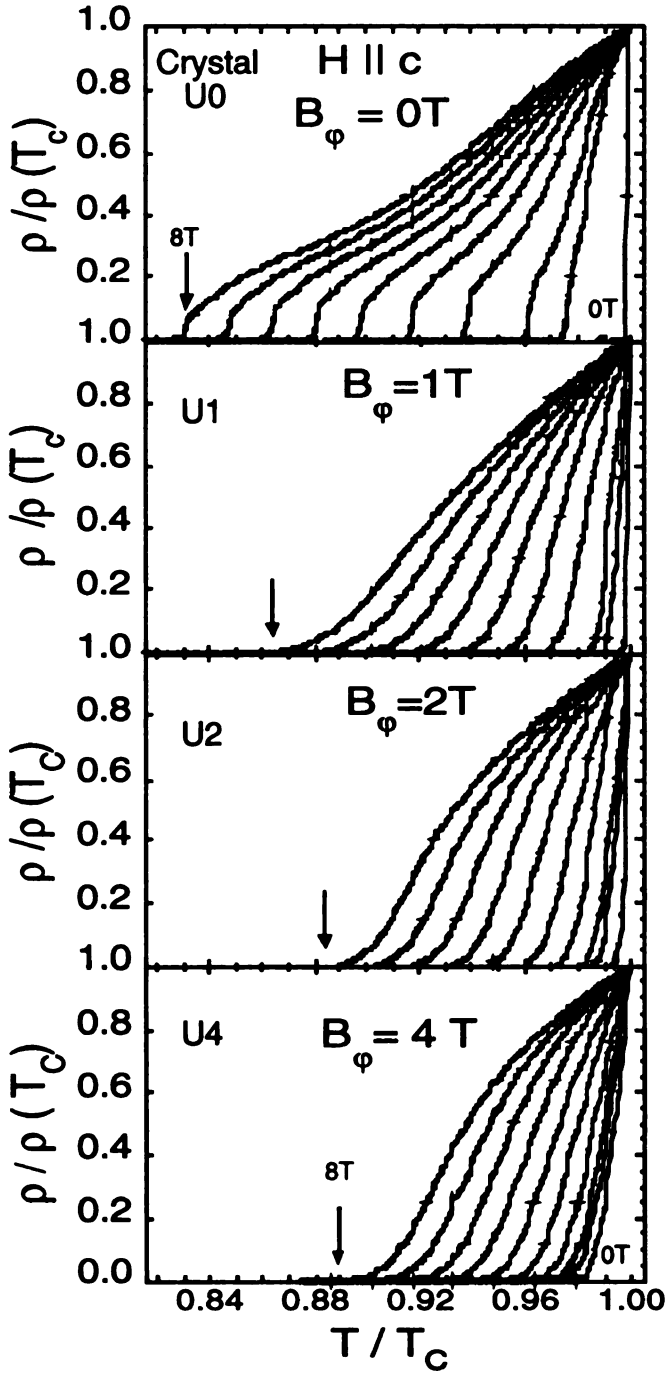

Figure 8.1 Resistvity vs. temperature, for crystals irradiated with $^{237}U^{67+}$ ions, to a dose matching field B_Φ = 0, 1, 2, and 4T. Shown are for applied fields of 8,7,6,5,4,3,2,1,0.5, and 0 Tesla.

down to the experimental resolution. The result is also found in data for crystals U2 and U4. The absence of a kink and the presence of ohmic behavior suggest that the vortices remain in the liquid state down to the zero resistivity limit.

The dramatic anisotropic pinning behavior of columnar defects is demonstrated in Figure 8.3 where we show the angular dependence of the resistivity measured at a fixed field value and at several temperatures. At high temperatures, we observe a broad maximum at $\theta = 0°$ when the magnetic field is aligned with the crystallographic c-axis and a minimum at $\theta = 90°$ when the field is parallel with the ab-plane of the crystal. This behavior at high temperatures reflects the anisotropic superconducting behavior of YBCO due to its effective mass anisotropy. With lowering temperatures, the broad maximum observed at $\theta = 0°$ slowly transforms into a shallow minimum as the columnar defects induced by heavy ion irradiation along the c-axis begin to trap the vortices in the liquid state. With further lowering of the temperature, the shallow dip turns into a sharp minimum. We define the onset of the anisotropic pinning due to columnar defects as the temperature where the dip centered around $\theta=0°$ first appears. This onset temperature can also be determined by the temperature where the two resistivity curves in Figure 8.3 inset, taken at two different angles of the applied field, first deviate from each other.

The magnetic field dependence of the onset temperature of anisotropic pinning by columnar defects T_{onset}, for U1, U2, and U4 is shown in Figure 8.4, where here the data is normalized to T_c. At low applied fields (H<1 Tesla), the T_{onset} curves for all three crystals lie almost lie on top of each other, regardless of

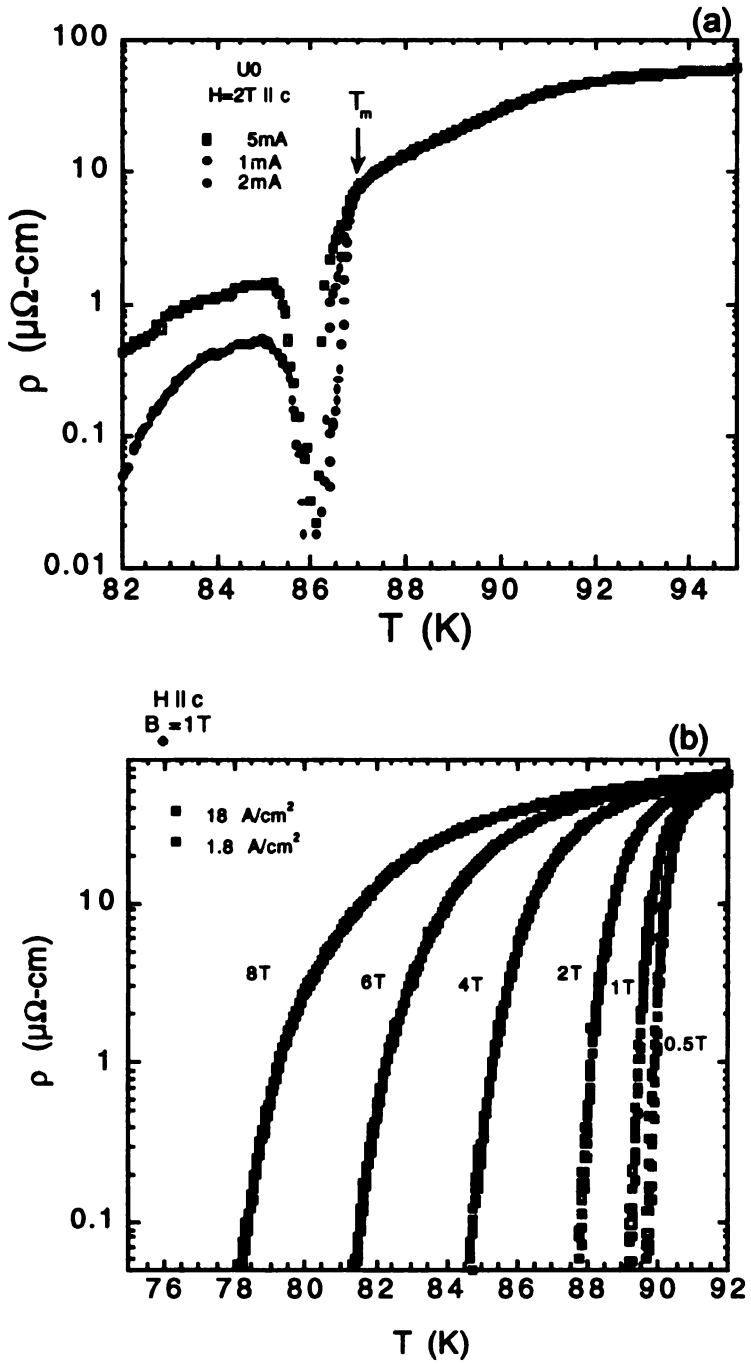

Figure 8.2 (a) Preirradiation melting transition, marking the onset of nonohmic behavior. (b) After irradiation only ohmic behavior is observed.

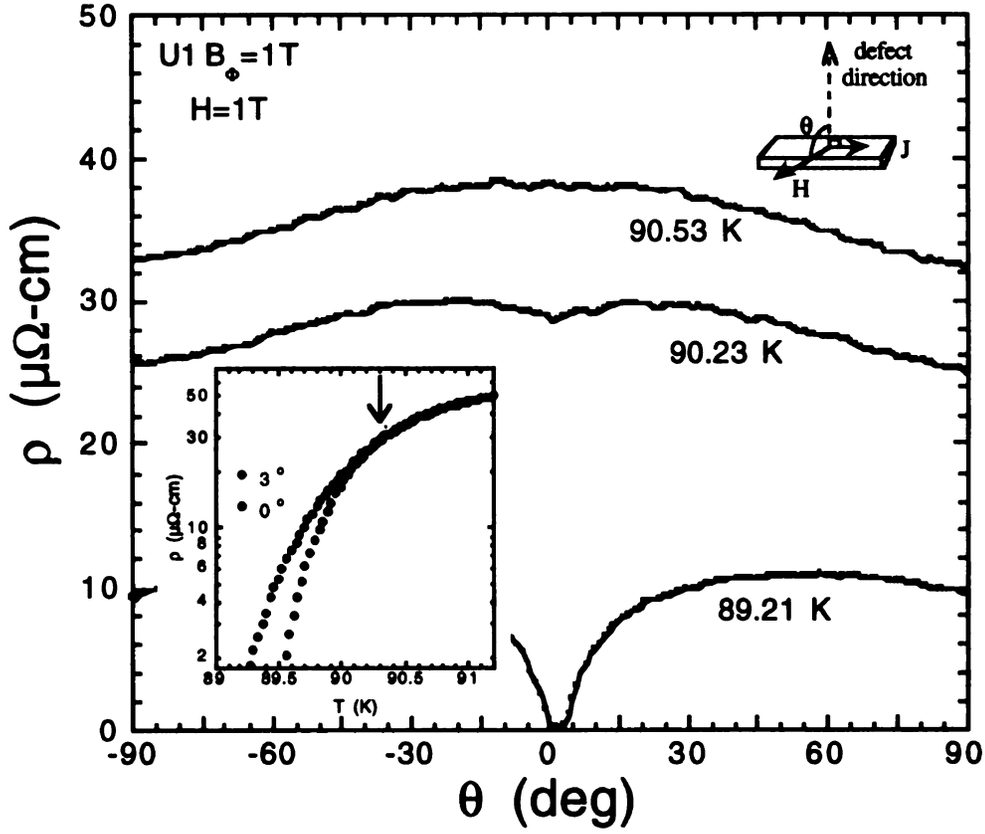

Figure 8.3 Angular dependence of the resistivity, demonstrating the anisotropic pinning strength of the columnar defects.

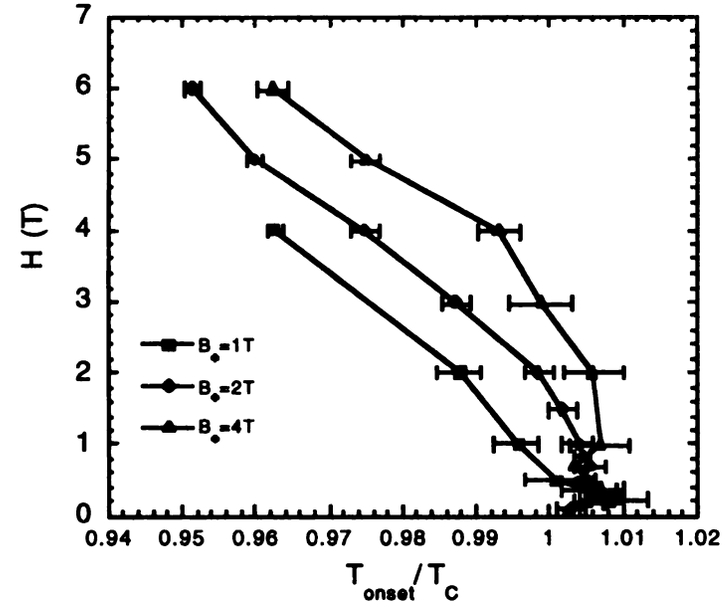

Figure 8.4 Onset of columnar pinning in the vortex liquid as a function of applied field, for defect matching fields of 1, 2, and 4T.

the dose matching field. In this field regime, the defect density is greater than the vortex density for all three crystals since the lowest dose matching field is B_Φ=1T. As the field is increased, T_{onset} decreases, as the ratio of vortices to pinning sites increases. For H = 1T and above, T_{onset} becomes strongly dependent on the irradiation dose, with higher onset temperatures with higher doses. These results demonstrate the remarkably controlled change in the vortex pinning behavior as the ratio of columnar defect to vortex density is varied.

We verified the ohmic behavior observed in the liquid state in Figure 8.2 with DC current-voltage curves. Figure 8.5(b) show the *E-J* curves in a log plot for the B_Φ = 4T crystal, taken at H=2T || c at various temperatures. The corresponding temperatures are marked with arrows in the resistivity vs. temperature data, in Figure 8.5(a). The measurement resolution is $E = 3x10^{-7}$ V/cm. For current densities below ~20 A/cm^2, the electric field shows ohmic behavior. Non-ohmic behavior is observed above 20 A/cm^2. However, this appears to be caused by sample heating at the current contacts, appearing as the applied current is increased. This was further confirmed by ac resistivity measurements at current densities up to 195 A/cm^2 as shown in Figure 8.5(c) where we observed a systematic shift to higher resistivity with increasing measuring current density due to heating of the sample. Thus within a DC measuring current density of 20 A/cm^2, we observe ohmic behavior in all the crystals irradiated with U ions. The results suggest that after irradiation, the vortex liquid state persists down to temperatures below which we are unable to measure the resistivity. We define an irreversibility temperature as the

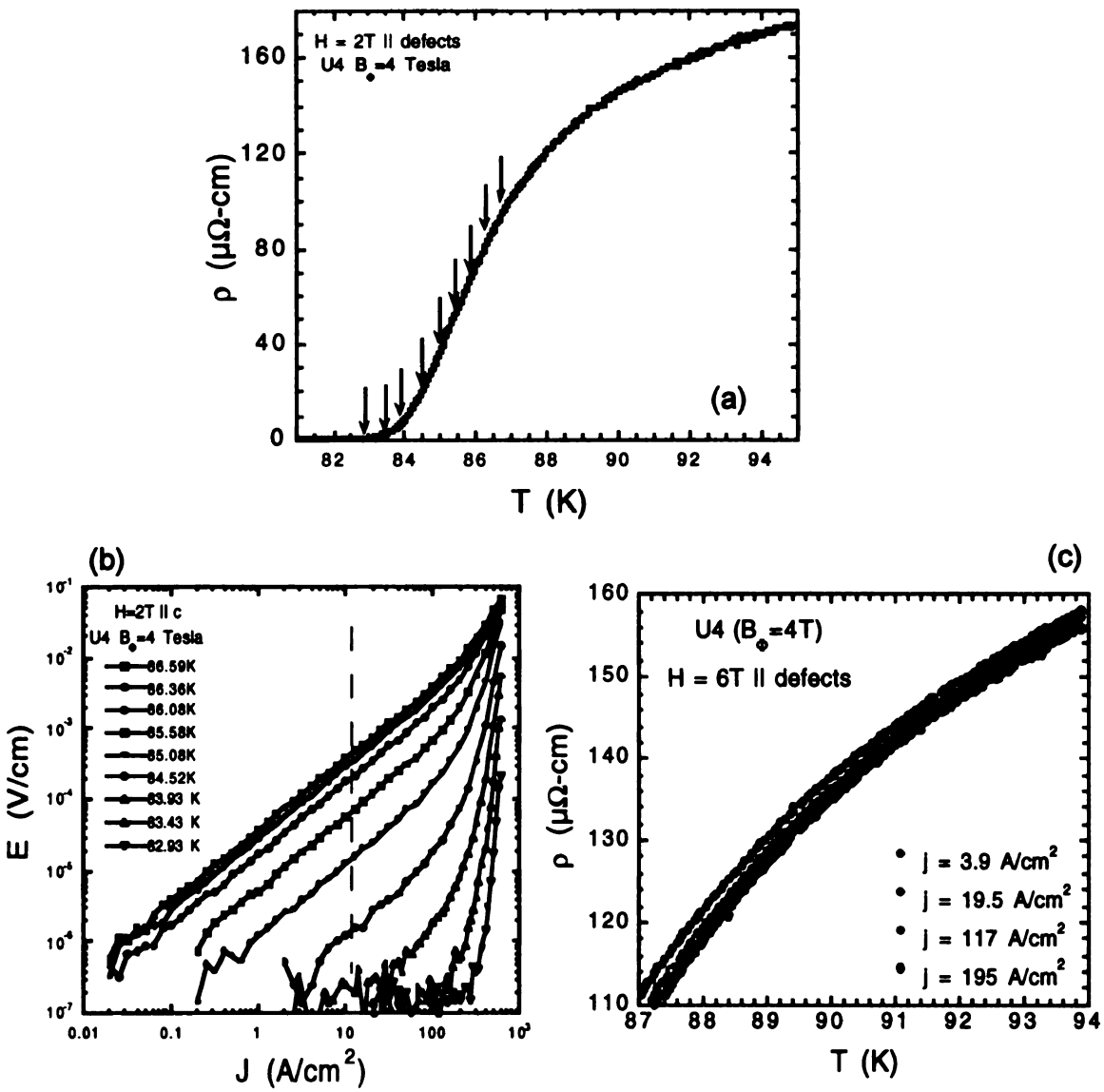

Figure 8.5 (a) RvT for U4, H=4T. Arrows indicate temperatures where E-J curves were obtained as shown in (b). In (b) the dashed line indicates the crossover current for ohmic behavior below and non-ohmic above the line. (c) Contact heating at high current densities.

temperature where ρ = 0.01 μΩ-cm, the resolution of the experiment. This represents an upper bound of the irreversibility behavior. Figure 8.6(a) shows the irreversibility line on an H-T phase diagram for the irradiated (B_Φ=1, 2, and 4T) crystals using this criterion. For comparison, the temperature axis is normalized to the zero resistance temperature at zero field for each crystal. The plot shows an upward shift of the irreversibility line with irradiation dose. Also plotted for comparison is the melting transition for U0, defined by the onset of the peak in the temperature derivative of the resistivity, $d\rho / dT$. All the irradiated samples show a change in slope of the irreversibility line, with linear behavior above, and positive curvature below their respective dose matching field B_Φ, indicated by the arrows in the figure. Best fits of the low field data below the matching field to $|1-t|^\alpha$ are presented in Figure 8.6(b) and linear fits to the high field data above the dose matching field for each irradiated crystal are shown in Figure 8.6(c). Above the matching field, the linear slope increases with dose (Fig. 8.6(c)). If we extrapolate the first order vortex melting line with the fitted irreversibility lines after irradiation, we find that they intersect at 47.5T, 29.5T, and 15.5T for crystals U4, U2, and U1 respectively (see Figure 8.6(d)). This suggests a possible recovery of the first order melting transition at high fields. Indeed, we will show in Chapter 9 for crystals irradiated with a low dose matching field, the first order transition is recovered at a measurable field.

The abrupt change in slope of the irreversibility line at an applied magnetic field related to the matching field has been previously reported, by Smith et al., at H= B_Φ[137] as well as by Krusin-Elbaum et al., at H=1/2B_Φ[127], and by

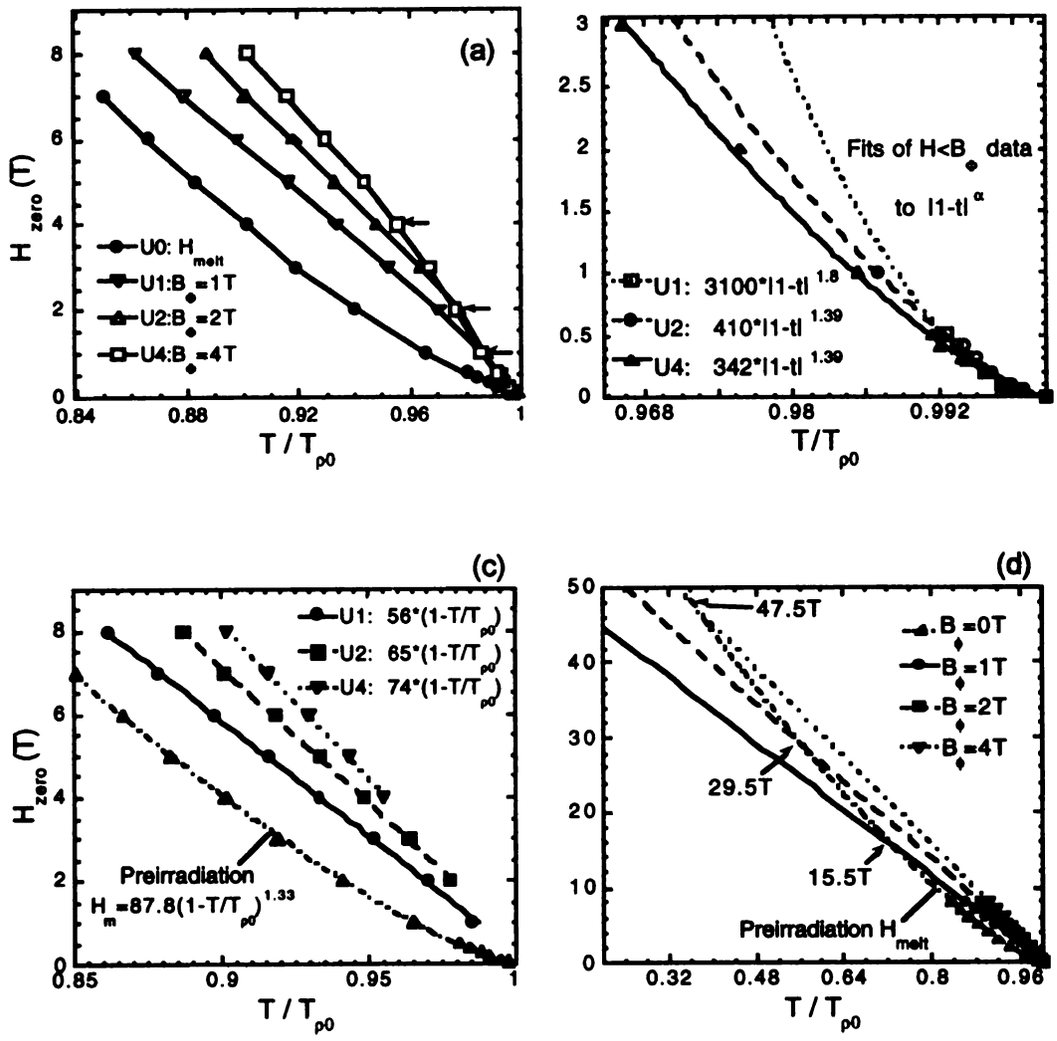

Figure 8.6 Irreversibility lines versus normalized temperature, for U1, U2, and U4.

Paulius et al. at $H=2B_\Phi$[44]. The linear behavior above B_Φ can be interpreted as a weakening of the overall pinning efficiency when the vortices outnumber the columnar defects as the vortex-vortex interaction begins to dominate[138, 139].

It has been predicted[139] that the rate of increase of the critical current with decreasing temperature will be lower for fields above B_Φ compared with fields below B_Φ, as a result of the weakening of the pinning strength above B_Φ. Since our data only show ohmic behavior, we are not able to determine the critical current. However, an upper bound can be determined from our data if we use a criterion of $E = 10^{-6}$ V/cm, the limit of our resolution for DC measurements, to define the critical current density. In this manner we identify J_c as the measurable vortex motion in the E vs. J curves. Plotted in Figure 8.7(a) is J_c vs. T for crystal U2, for fields above and below B_Φ=2T. The data shows no abrupt change in the slopes $\Delta J_c / \Delta T$ for all applied fields near 2T. Samples U1 and U4 also display similar behavior.

However, a comparison among the irradiated crystals with the unirradiated crystal demonstrates an increase in the pinning efficiency with increasing dose matching field. Plotted in Figures 8.7(b) through 8.7(f) are J_c vs. $T/T_{\rho 0}$ data for U1, U2, and U4, in applied fields of 0.5, 1, 2, 4, and 6T, respectively. The critical current for the irradiated crystals lie above the critical current of the unirradiated (pristine crystal) crystal, at all magnetic fields. In Figure 8.7(b) a comparison of the three irradiated crystals taken at a magnetic field value of $H = 0.5T < B_\Phi$ show that all the curves lie almost on top of each other and seem to be independent of the defect dose. Likewise, we observe similar behavior for H = 1T in all the

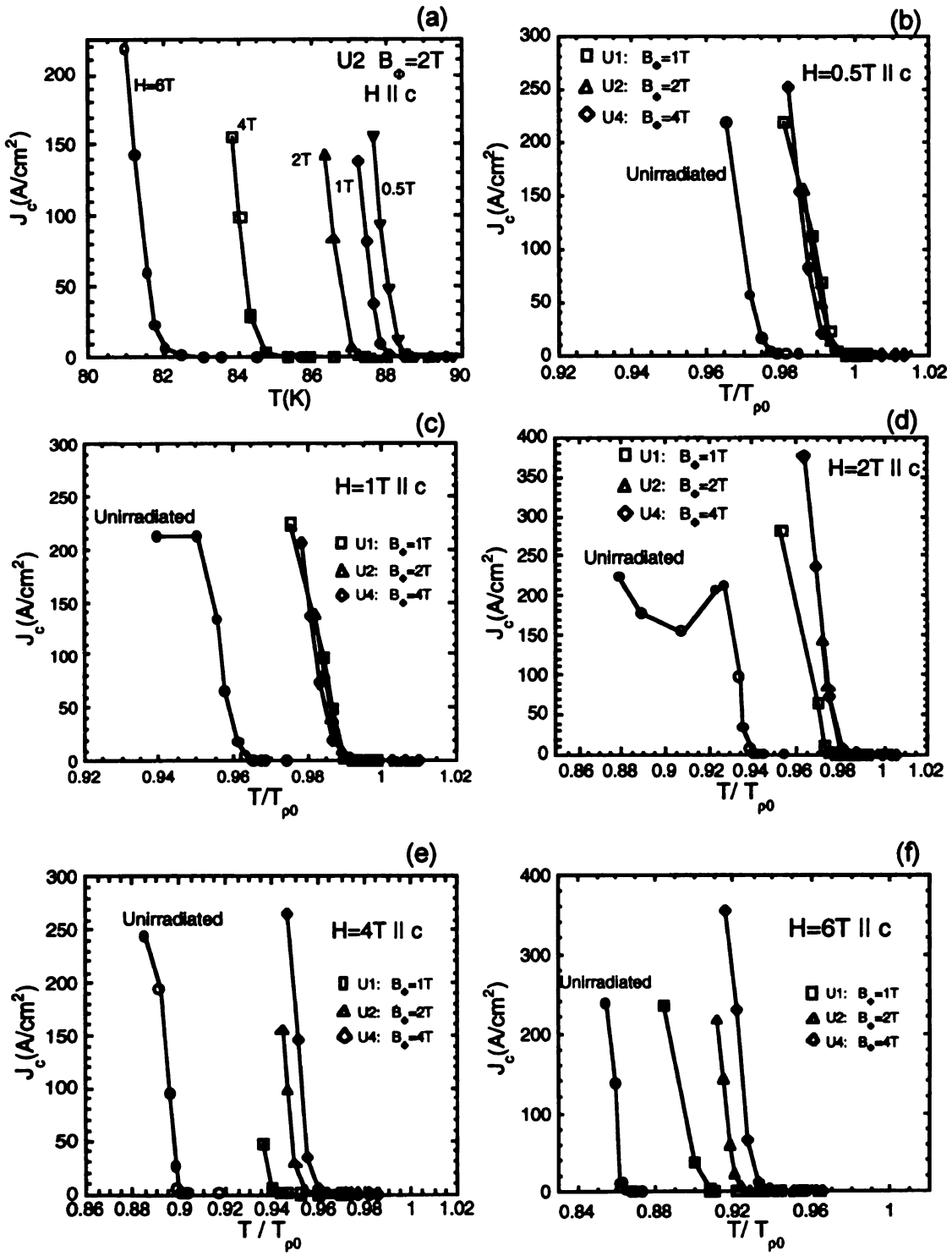

Figure 8.7 Critical current versus temperature for U1, U2, and U4.

irradiated crystals. However, for H = 2T, the J_c curve for sample U1 (B_Φ = 1T) begins to fall below the J_c curves of samples U2 (B_Φ = 2T) and U4 (B_Φ = 4T), which were irradiated with higher dose matching fields, as shown in figs. 8.7(c). At even higher fields, the J_c curve for U2 begins to fall below that of U4, as shown in figs. 8.7(e) and (f). Thus the pinning efficiency decreases as the number of vortices outnumbers the columnar defects, although the functional dependence of J_c with temperature remains the same.

As previously discussed in Chapter 5, a Bose glass transition is predicted for crystals irradiated with columnar defects. This theory predicts a power law dependence on the tail of the resistivity data: $\rho \sim (T-T_{BG})^s$, where $s = \nu(z-2)$, and ν and z are the static and dynamic scaling exponents respectively. Recall this ansatz is for the case of an ohmic resistivity at low currents, which is applicable for these crystals where we find only ohmic behavior. We determine T_{BG} and s by fitting the tail of the resistivity transition, by evaluating the linear region of the $\rho / (d\rho/dT)$ vs. T plot, as shown in Figure 8.8(a). The inverse of the slope yields s = 3.6, while the temperature intercept gives T_{BG} =85.78 K. In order to check the quality of the fit, we compared the result with the measured experimental data, as shown in Figure 8.8(b). To within an error of Δs=±0.3, the fit is in excellent agreement with the measured data. Figure 8.8(c) shows the results of this analysis for U1, U2, and U4, in fields up to 8 Tesla. Our values for the scaling exponent s vary widely in field from 2.5 – 6. Previous measurements[44] of an untwinned YBCO single crystal irradiated by 1 GeV U ions also find ohmic behavior in the resistivity data at all temperatures. From these measurements a

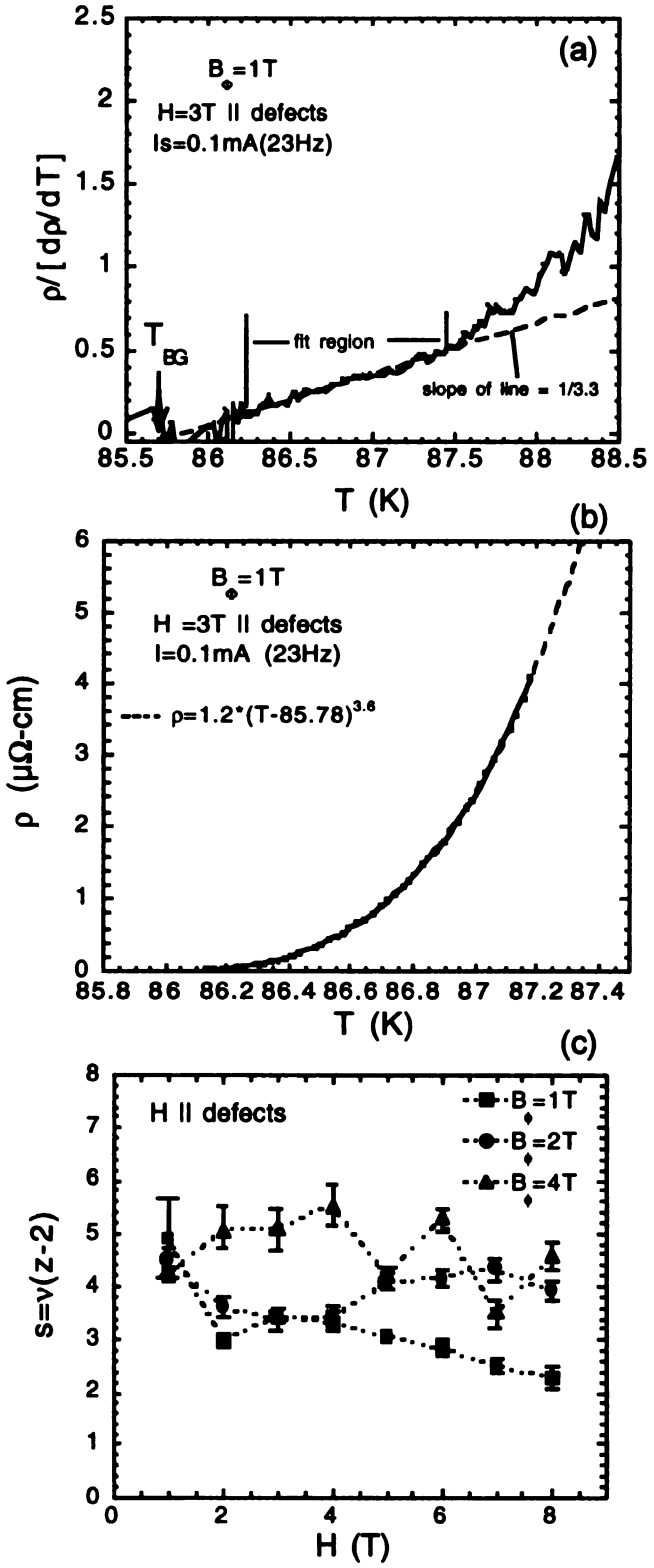

Figure 8.8 (a), (b) Evaluation the tail of the resistivity data in terms of the Bose glass transition $(T\text{-}T_{BG})^s$. (c) Results of s for U1, U2, and U4.

value of $s = 5.2 \pm 0.4$ was obtained for applied fields up to 7 Tesla, in general agreement with our results.

8.3 Lead ion irradiation: Pb1

The sample Pb1, irradiated with 1.4 GeV Pb ions to $B_\Phi = 1$ Tesla, is compared with an unirradiated piece of the same crystal, sample Pb0, in Figure 8.9. Similar to the uranium-irradiated samples, the kink in the resistivity associated with the first order vortex melting transition in the unirradiated crystal is replaced by a smooth continuous transition after irradiation. However, unlike the uranium irradiated samples, Pb1 show *non-ohmic* behavior at measurable resistances, as shown in Figure 8.10. The onset of non-ohmic behavior is represented by the temperature where the resistivity curves, measured at two different currents 1 mA and 0.1mA in a magnetic field, begin to deviate from each other. This point marks the onset of the Bose glass critical regime expected for a continuous liquid-to-glass transition. At high magnetic field, the onset of non-ohmic behavior shifts to lower temperatures and the corresponding resistivity values also decreases. For fields above 4 Tesla the non-ohmic behavior is below the sensitivity of our apparatus.

As described in Chapter 5, in the presence of correlated defects, the Bose glass theory predicts a continuous transition which is described by a transverse and a longitudinal correlation length given by: $\ell_\perp \sim 1/|T_{BG} - T|^\nu$ and $\ell_\parallel \sim \ell_\perp^2$ respectively, where T_{BG} is the Bose glass transition temperature, and ν is a critical scaling exponent. The relaxation time of a fluctuation is expected to diverge with

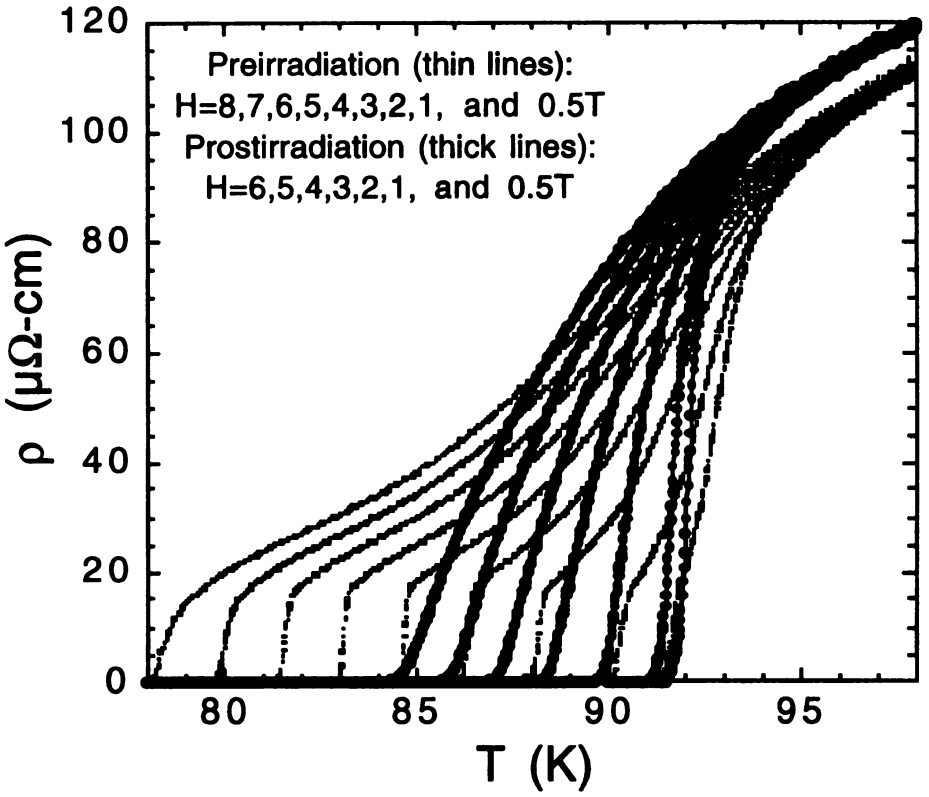

Figure 8.9 Resistivity versus temperature for Pb0 (unirradiated) and Pb1 (1T defect dose).

a dynamic scaling exponent *z*, given by: $\tau \sim \ell_{\perp}^{z}$. From the anisotropic Ginzburg-Landau free energy, the current density scales as $J \sim 1/\ell_{\perp}\ell_{\parallel}$, while the resultant electric field produced by vortex motion scales as $E \sim 1/\ell_{\perp}\tau$, leading to the *scaling ansatz* for the critical current, describing the critical regime: $E\ell_{\perp}^{1+z} = F_{\pm}(\ell_{\perp}\ell_{\parallel}J\Phi_0/cT)$ where $F_{\pm}$ is the universal scaling function. While F_{+} and F_{-} are unknown, the scaling hypothesis allows current-voltage data for different temperatures to be collapsed onto F_{+} above, and F_{-} below T_{BG}. Since the

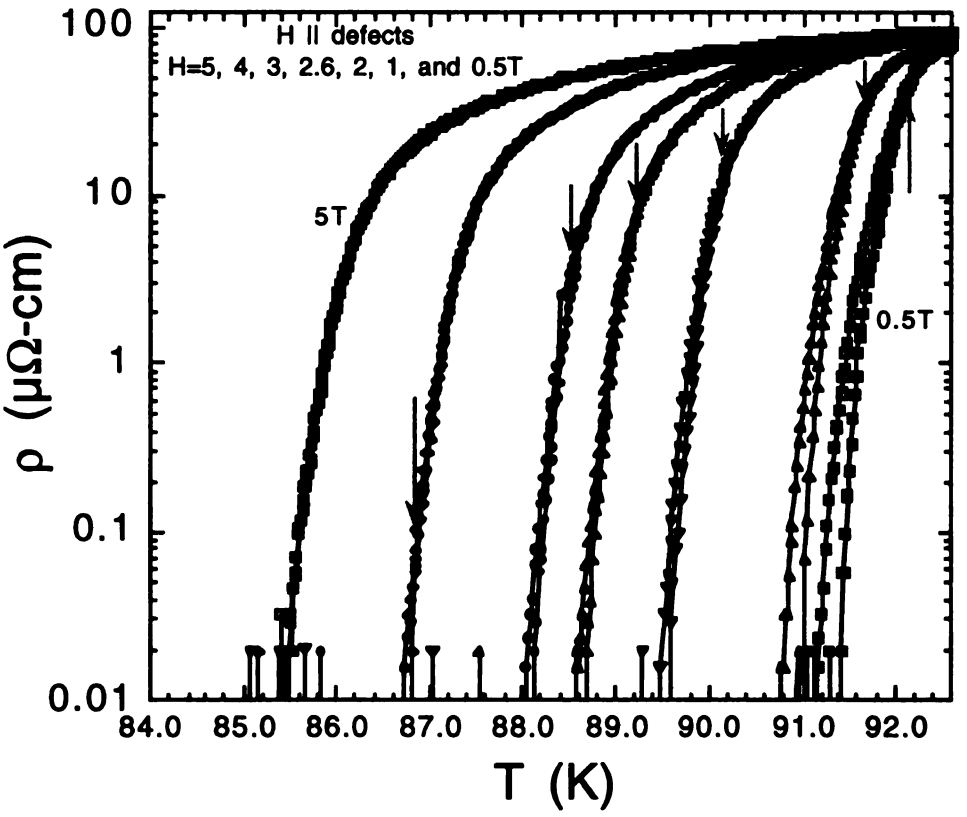

Figure 8.10 Onset (arrows) of non-ohmic behavior in the liquid state, for crystal Pb1.

response is finite at the transition, the two divergent lengths must cancel there, giving a power law dependence $E \sim J^{(1+z)/3}$ when $T = T_{BG}$.

Figure 8.11(a) shows DC current-voltage curves for Pb1, taken above and within the non-ohmic critical regime, for H = 1 Tesla. The curves are linear for $T \geq 91.70$ K, where the resistive response is ohmic, and become progressively non-ohmic with decreasing temperature. In Figure 8.11(b) the nonlinear curves have been scaled according to the scaling ansatz, with an excellent collapse of the data both above and below T_{BG}. The critical exponents ν and z, as well as the Bose glass temperature were varied to obtain the best overall fit. From this

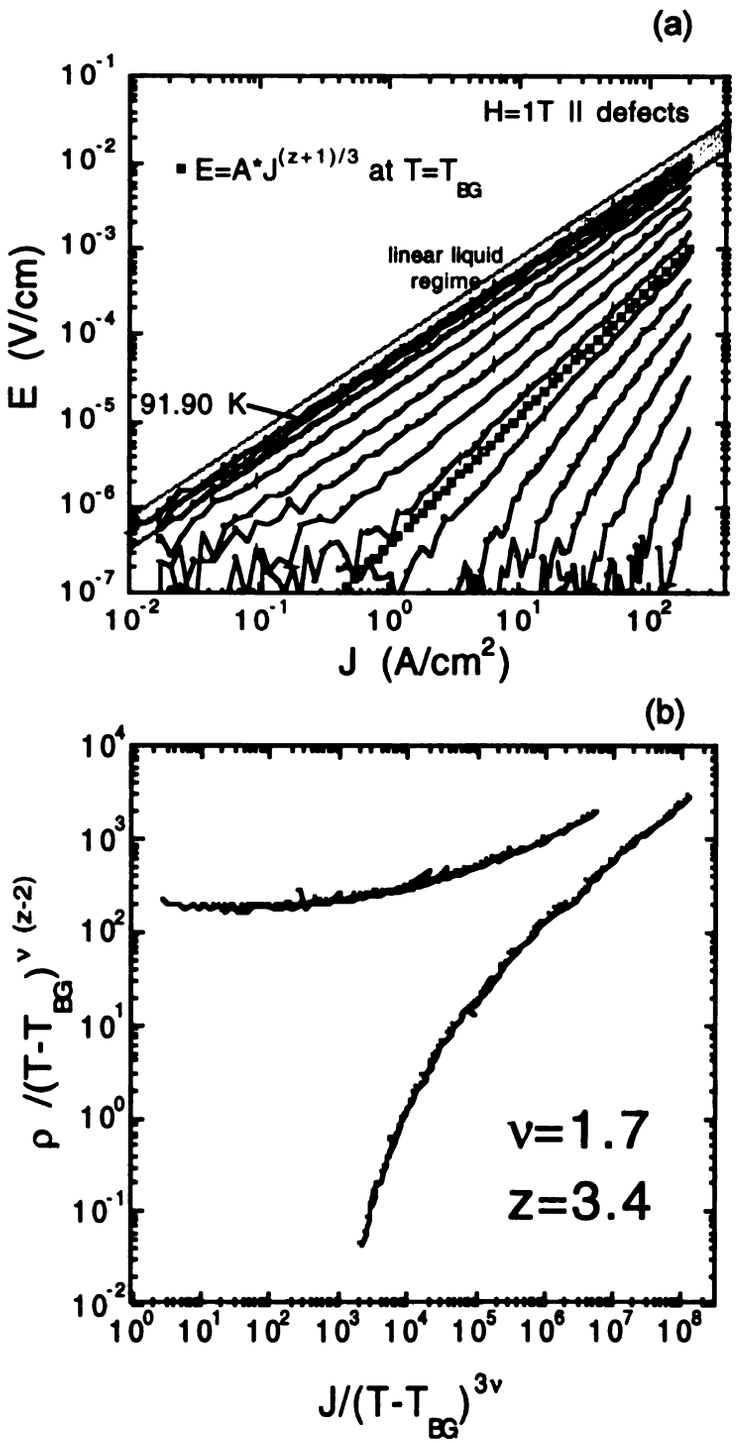

Figure 8.11 (a) E-J curves for Pb1 (H=1T || defects), showing a high temperature linear regime, and a non-ohmic critical fluctuation regime surrounding the Bose glass transition temperature T_{BG}. (b) Scaling of the non-ohmic curves.

analysis we obtain ν=1.67±0.10, z=3.44±0.10, and s=$\nu(z-2)$=2.4±0.2. Similar analysis for H = 0.2T, 0.5T, and 2T, yielded the *same* critical exponents, as shown in Figure 8.12.

Also plotted in Figures 8.11 and 8.12 is the expected power law dependence $E \sim J^{1.47}$ at T_{BG}, where we have used z = 3.44. This power law behavior is consistent with the experimental data, and serves as a consistency check for the scaling analysis. Figure 8.13(a) shows the vortex phase diagram for Pb1. The Bose glass transition temperature, obtained from the above *E-J* scaling (circles) shifts to lower temperatures as the applied field is increased. Beyond H = 4T, the non-ohmic behavior characterizing the onset of the Bose glass critical regime is shifted to lower temperatures and lies below the measurable voltage resolution of the experiment. For these fields, we resort to fitting the tail of the *ohmic* resistivity data with the power law $\rho \sim (T-T_{BG})^s$, as was done with the U ion data to obtain the Bose glass transition temperature. The tail of the ρ vs. T measurements for H = 4-6T was fit to this power law, in a temperature range of 0.5-0.7 K. From this analysis we obtained $s = \nu(z-2) = 4.4 \pm 0.5$, a value substantially higher than that obtained from the *E-J* scaling procedure. A possible reason for this discrepancy may be that our resistivity data are not within the true critical fluctuation regime for these fields, which perhaps lie at even lower temperatures. The obtained values for s however are in agreement with the values obtained from the U data above.

The values of T_{BG} obtained from scaling the *E-J* curves are in very good agreement with the T_{zero} curve where the resistivity goes to zero, using a criterion

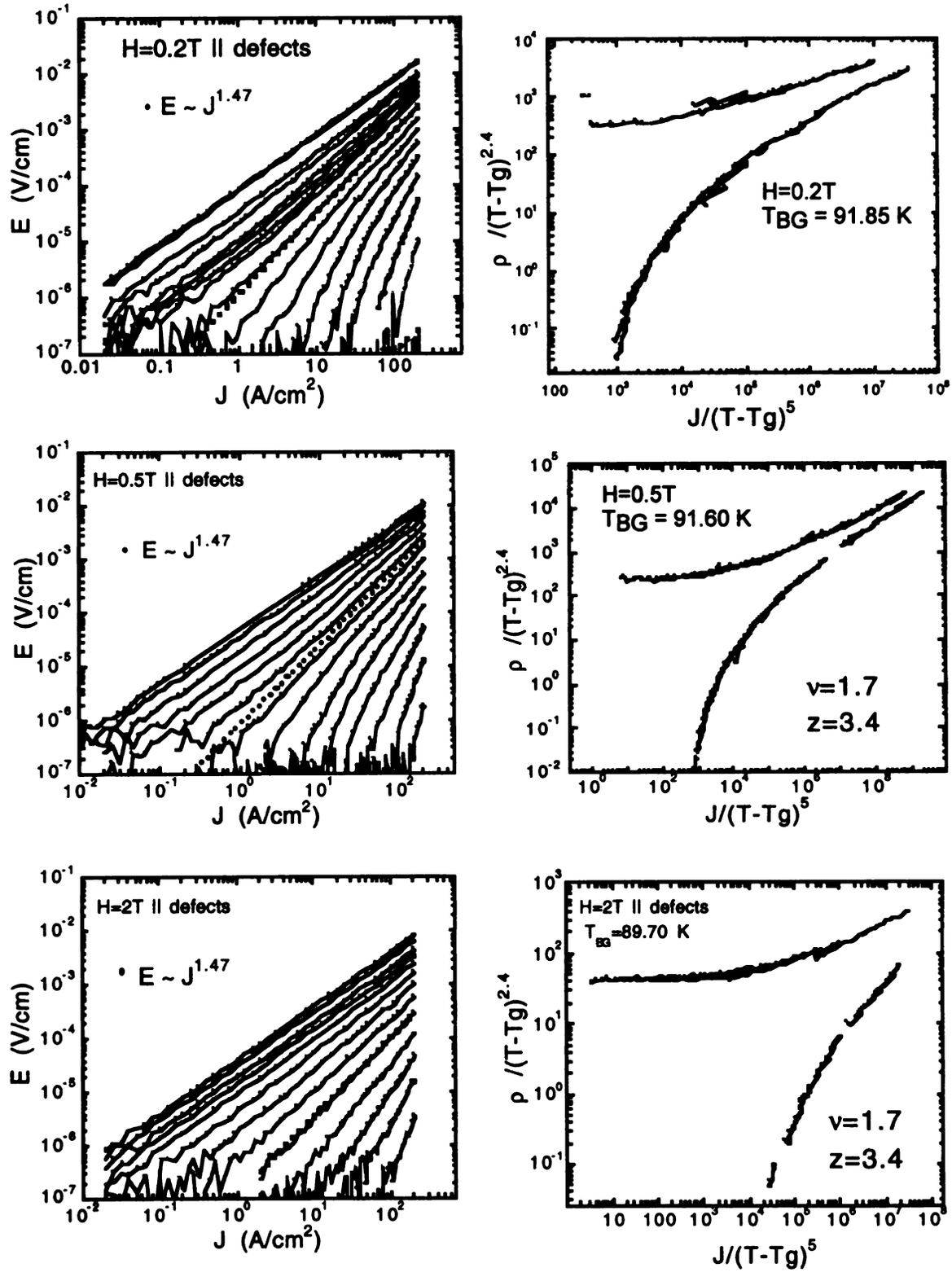

Figure 8.12 E-J curves and scaling for H=0.2, 0.5, and 2T.

of ρ = 0.01 μΩ-cm, as shown in Figure 8.13(a). A plot of the irreversibility line using the T_{zero} criterion shows an abrupt change in slope of the Bose glass transition line at the dose matching field for the Pb1, similar to the one observed in the uranium irradiated crystals, as shown in Figure 8.13(b). Also plotted in the same phase diagram is the first order vortex melting line before irradiation. An extrapolation of the linear behavior above H = B_Φ = 1T shows that the first order melting line intersects the irreversibility line after irradiation near H = 26T, much bigger than the value of 15.5T reported for the uranium irradiated sample, U1. A comparison of the irreversibility line of Pb1 and U1 in Figure 8.13(a) shows that H_{irr} for Pb1 lies above that of U1, indicating that the solid phase is enhanced more with the Pb ion irradiation than with U ions for a 1T irradiation dose. Furthermore, the critical current density for Pb1 is also enhanced over that of U1 as shown in Figure 8.13(d), where the temperature dependent critical current curves for Pb1 always lies above that of U1 for all fields.

8.4 Angular dependence for Pb1

The anisotropic pinning behavior of the defects predicted from the Bose glass theory is exemplified by the detailed plot of the resistivity when the magnetic field is tilted away from the columnar defect direction, as shown in Figure 8.14(a). The minimum dissipation at $\theta = 0^\circ$ indicates that columnar defects are most effective as pinning sites when the vortices are aligned along the defect direction. Dissipation increases with increasing tilt angle, up to $\theta = \theta_a$, beyond which

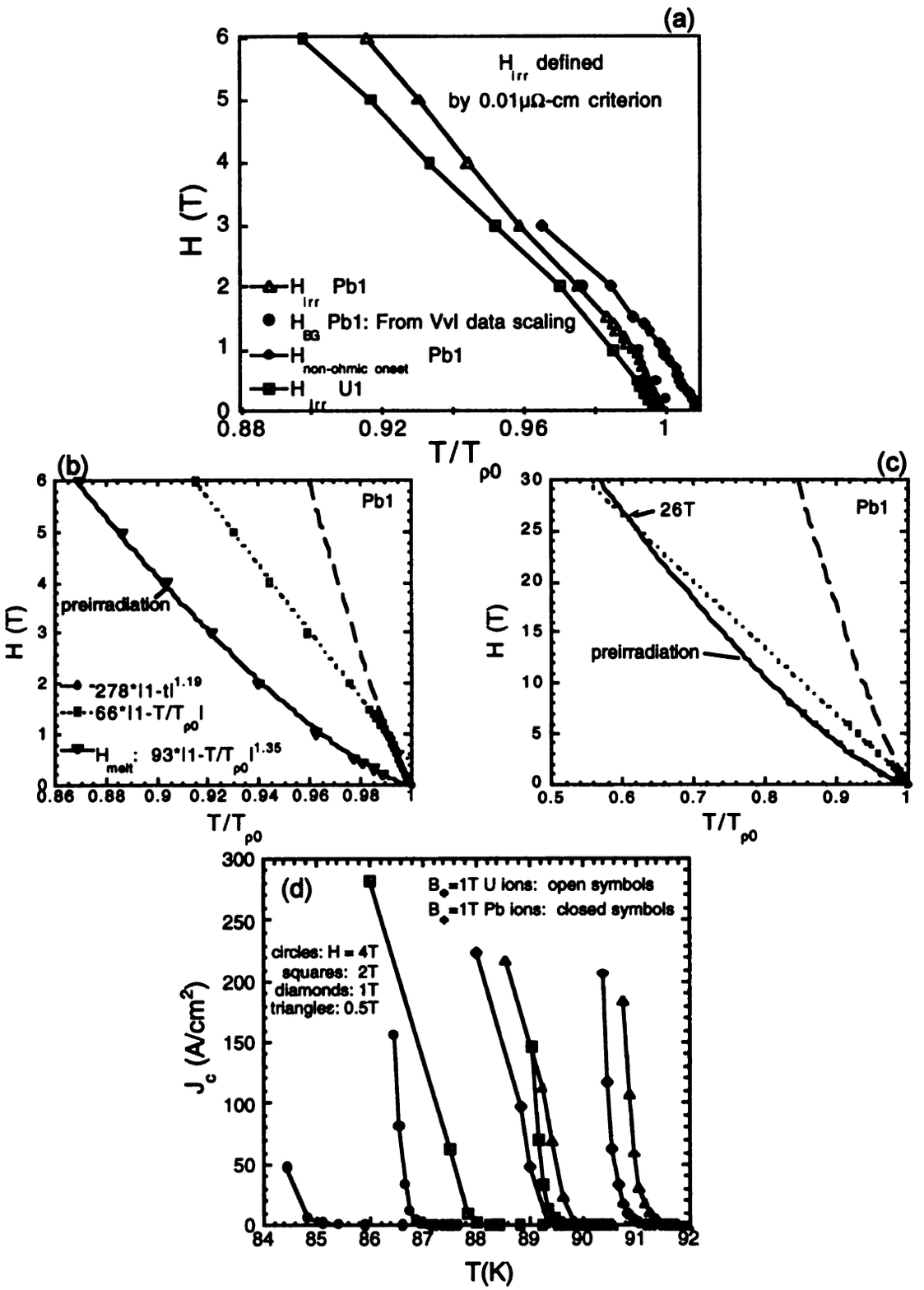

Figure 8.13 (a) Transition lines for Pb1, U1. (b) and (c) Transition line for Pb1, as compared to the preirradiation melting line. (d) J_C v. T for Pb1 and U1.

pinning by columnar defects disappears and dissipation is dictated by the intrinsic superconducting anisotropy.

As the temperature is lowered below $T_{BG}(\theta = 0)$, the Bose glass phase is entered, characterized by strong vortex localization along the defect tracks. Within this so called 'transverse Meissner' phase[86, 87] an infinite tilt modulus is expected, where the vortices remain aligned to the tracks even as the applied field is tilted. However, at some finite $H_{\perp}^{c}(T)$, a lock-in transition[87] occurs, where the strongly pinned Bose glass state is transformed continuously into a kinked vortex configuration[93]. The transition is characterized by a sharp increase in the measured resistivity, due to the relatively free motion of the kinks as they move along the columnar defects. As the temperature is lowered, the angle where the transition occurs increases. The lock-in transition is expected to scale from above as [86, 87, 92] $T_{BG}(0) - T_{BG}(\theta) \sim | H_{\perp}{}^{c} |^{1/\nu}$. The transition cannot be scaled from below, since $l_{||}$ is essentially infinite (equal to the sample thickness) below the transition.

At H=1.0T and at very small angles -1°<θ <1°, we measured several *E-J* curves at various temperatures near T_{BG}. We can collapse the *E-J* data with the same scaling procedure as the θ=0° data, obtaining s= $\nu(z-2)$=2.4±0.10, ν=1.57±0.4, and z=3.55±0.5, in excellent agreement with our previous results. This is demonstrated in Figure 8.15, which shows scaled data for θ=1°. Thus within the 1° window the vortices behave as if they are perfectly aligned with the columnar pins, illustrating the effective localization of the vortices to the defect sites. Beyond 1° the data no longer can be scaled in this manner.

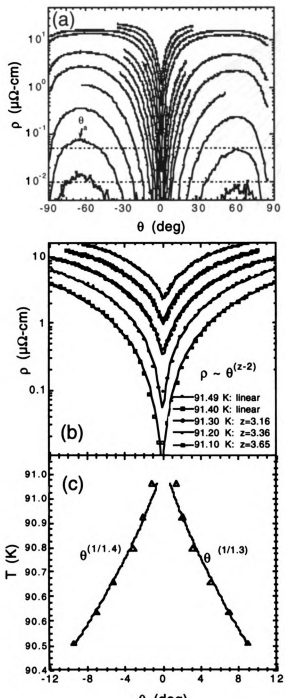

Figure 8.14 Angular dependence of the resistivity, for H=0.5T, crystal Pb1. (a) The arrow denotes the accomodation angle, beyond which the vortex lines are no longer confined to the defects. (b) Fits of the liquid phase near T_{BG}, as a function of angle. (c) Fits to the lock-in transition.

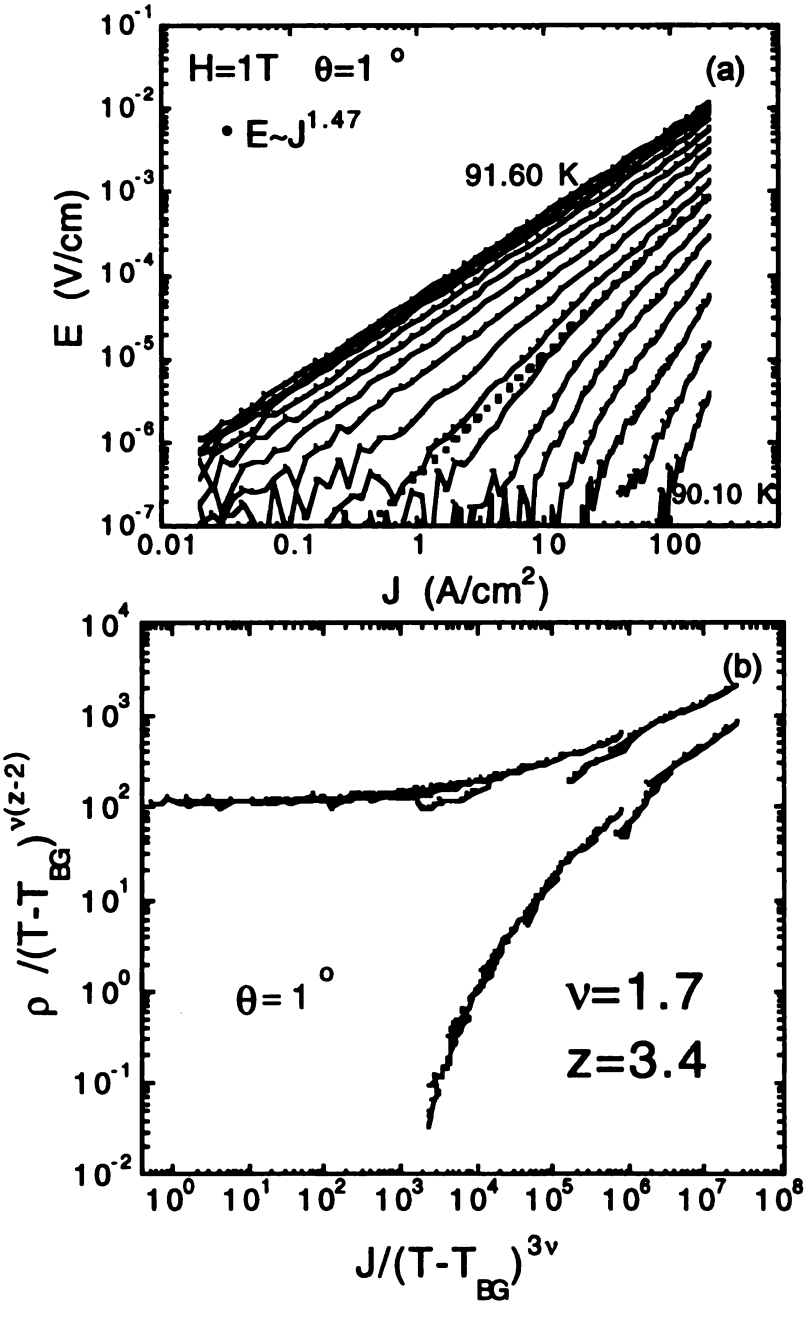

Figure 8.15 E-J curves and resultant scaling for H=1T, applied 1° from the defect direction.

As the angle between the applied field and the columnar defect tracks is increased, the current-voltage measurements no longer display the negative curvature that characterized temperatures below T_{BG}. This is shown in Figure 8.16, where E vs.J data is plotted for θ = 5, 25, 70, and 90°. While there appears to be a slight downward curvature in the θ = 5° data, none can be seen at the larger angles, although the low temperature curves still are non-ohmic. Since the negative curvature, clearly seen in the θ = 0-1° E vs. J data, is a criterion of the strongly pinned Bose glass transition, the lack of this negative curvature can be described as a weakening of the defects to effectively pin the vortex lines, and thus we cannot qualify the nature of the solid-liquid transition at large angles.

Shown in Figure 8.14(b) is ρ vs θ data for H = 0.5T. For the temperatures shown the vortex lines are in the liquid state, but at temperatures close to the Bose glass transition temperature T_{BG} = 91.10 K, here defined by the ρ = 0.01 μΩ-cm criterion. According to the Bose glass theory[87, 92], just at $T_{BG}(\theta=0^{\circ})$ the resistivity is expected to increase with increasing tilt as $\rho \sim \theta^{(z-2)}$. For $T > T_{BG}(\theta=0^{\circ})$, we find that the resistivity can be fit with a linear function and close to $T_{BG}(\theta=0^{\circ})$ the resistivity can be fit with $\rho \sim \theta^{(z-2)}$ with $z = 3.4 \pm 0.1$, in good agreement with the z value obtained from E-J scaling above.

In Figure 8.14(a) a sharp increase in resistivity is seen as the field is tilted away from the defect track direction. We equate this sharp jump with the lock-in transition, here determined by using a ρ = 0.01 μΩ-cm criterion to establish the onset of a measurable resistance. This same criterion was used earlier to obtain

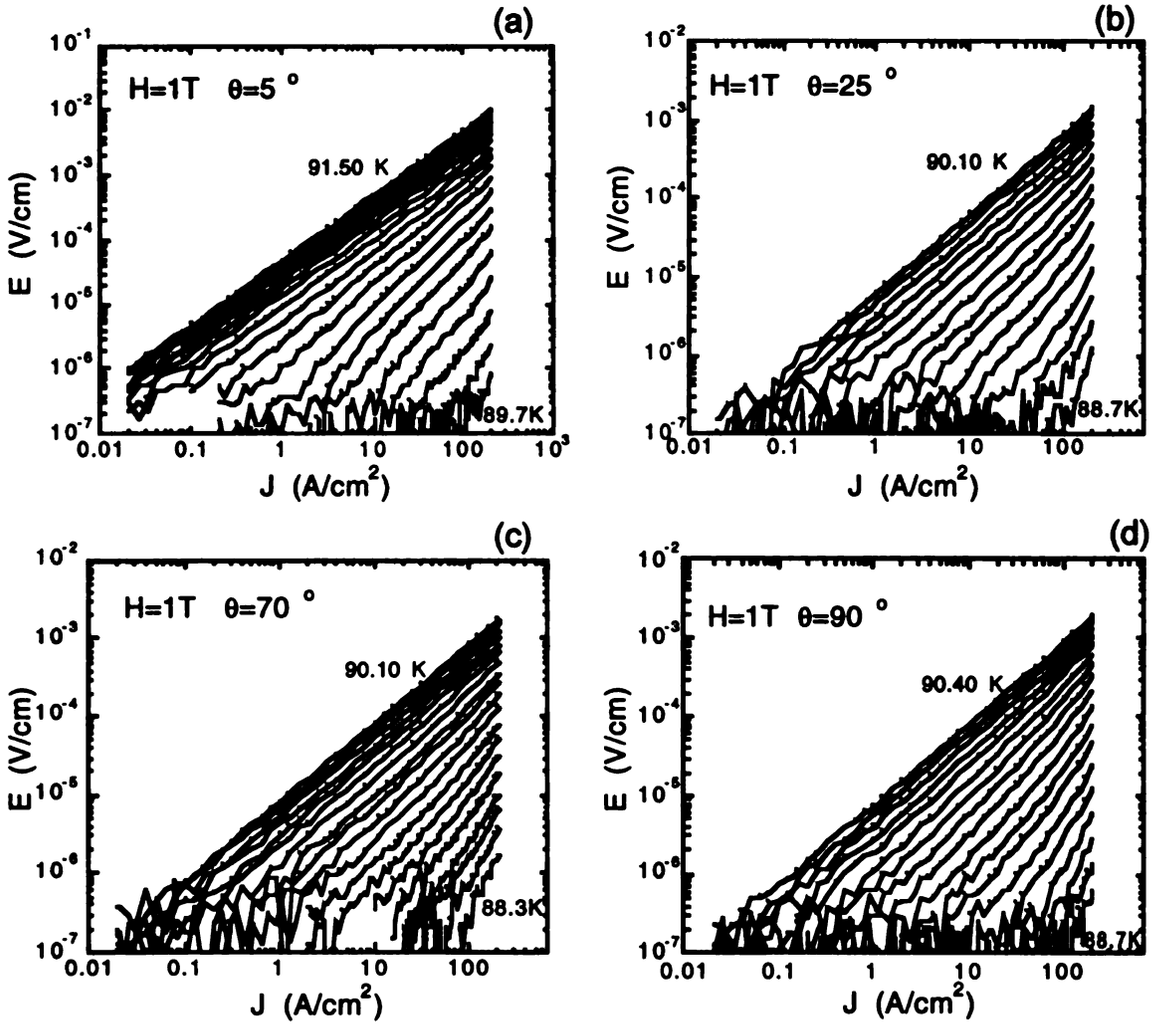

Figure 8.16 E-J curves for H=1T, applied at large angles.

T_{zero}, and since the T_{zero} line showed consistent agreement with the Bose Glass transition line obtained from scaling the *E-J* curves below H=3T, it may be a reasonable estimate of the glass-liquid transition at finite angle. The transition line is shown in the Figure 8.14(c), along with best fits to the lock-in transition function $T_{BG}(0) - T_{BG}(\theta) \sim | H_{\perp}^{c} |^{1/\upsilon}$, where $H_{\perp}^{c} / H \approx \theta$ for small angles. As a check, other resistive criteria were also investigated, with consistent results for ν. From this analysis, using resistivity criteria ranging from 0.05 to 0.1 μΩ-cm, we obtained $\upsilon = 1.7 \pm 0.4$, in excellent agreement with the earlier analysis. Recent

magnetization measurements carried out on untwinned YBCO samples irradiated with 4 GeV Au ions[140] found $\upsilon \approx 1.7-1.9$ for θ=1-10°, in agreement with our measurements. Data from twinned crystals[134, 141] find a sharper peak in the transition when compared to these results, demonstrating that the glass phase is more effectively stabilized with columnar defects than with twin boundaries.

In summary, a non-ohmic regime was observed in transport data on an untwinned YBCO crystal with columnar defects produced by Pb ion irradiation. The non-ohmic *E-J* curves were scaled following the Bose glass theory, both above and below a critical transition temperature T_{BG}, from which the critical exponents ν and z were obtained. The values of these exponents are in agreement with results obtained from the angular dependence of the resistivity. Finally, a sharp change in the slope of the irreversibility line was found at the matching field for crystals U1, U2, U4, and Pb1, with a weakening in the pinning efficiency for applied fields above B_Φ. Whereas a Bose glass transition is firmly established in the Pb1 crystal, the data from the uranium irradiated crystal show at best an upper bound of the transition. Nevertheless, a change in slope at the matching field is observed in data as well as enhanced pinning for both U and Pb irradiated samples. This consistency implies the existence of a Bose glass transition for the uranium samples, at temperatures where the resistivity has fallen below the experimental resolution.

Chapter 9

THE EFFECT OF LOW DOSES OF COLUMNAR DEFECTS ON VORTICES IN UNTWINNED $YBa_2Cu_3O_{7-\delta}$ CRYSTALS

9.1 Introduction

With new experiments on the first order melting transition line in $YBa_2Cu_3O_{7-\delta}$ single crystals, both an upper (H_{ucp}) and a lower (H_{lcp}) critical point of this melting line has been found. These critical points mark a pronounced change in the vortex behavior with disorder. The position of these critical points vary widely from sample to sample, even among so called 'clean' crystals. Furthermore, in some overdoped YBCO crystals, no evidence of an upper critical point has been found, although these crystals exhibit a fairly large lower critical point. On the other hand, in optimally doped YBCO crystals, the lower critical point can extend down to a few hundred Gauss and very close to the zero field superconducting transition temperature, although the upper critical point in this case is usually below 15 Tesla.

Within the vortex solid state, a second magnetization peak has been observed in magnetization loop data, shown schematically in Figure 9.1 inset. The onset of an increase in the magnetization at H^* as a function of increasing field indicates an enhancement of pinning within the solid state, as shown in Figure 9.1. The locus of points on the phase diagram in the vortex solid state which indicates this change in the vortex behavior is usually defined by the onset of increased magnetization[142], the peak in the derivative dM/dH[143], or, for very clean crystals, by the onset of hysteretic behavior[66, 144]. Above H^* lies

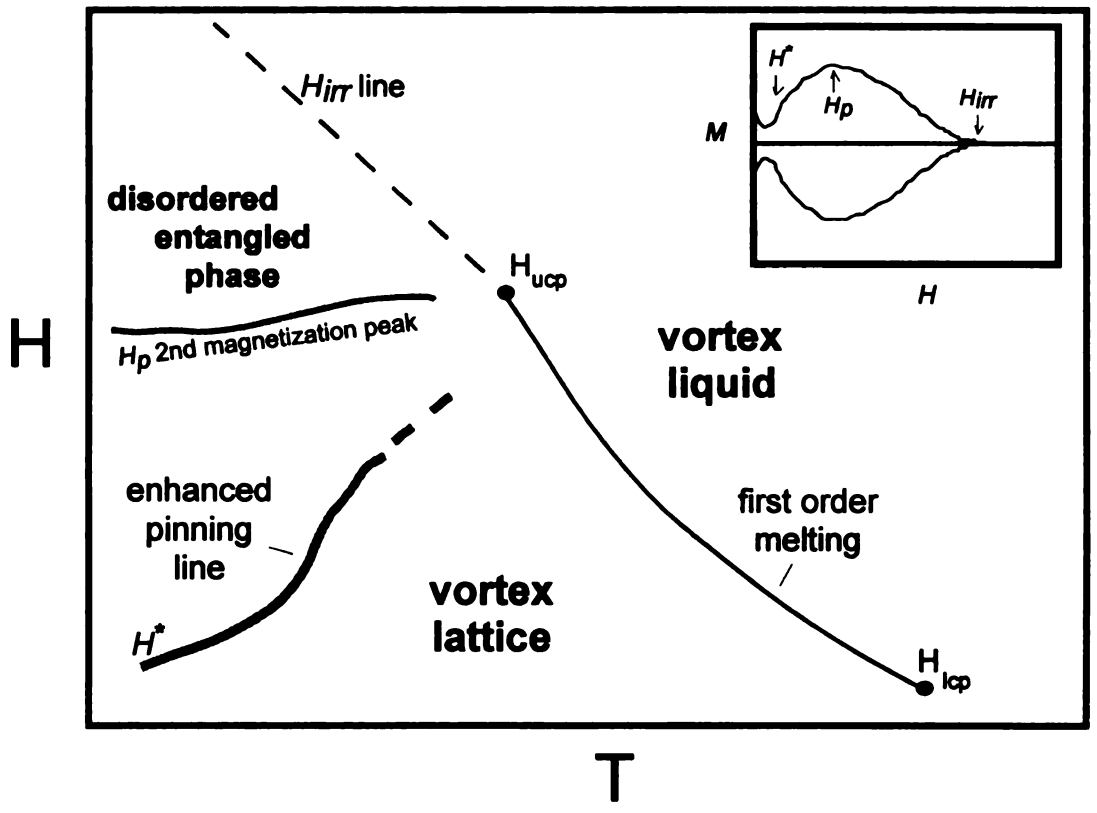

Figure 9.1 Phase diagram for YBCO. Inset shows a typical magnetization loop, for temperatures below T_{ucp}.

the peak in the magnetization data H_p, known as the 2nd magnetization peak (see Figure 9.1 inset). This line has been associated with a dislocation-mediated phase transition[59] from a vortex lattice to a disordered glass phase, with the line possibly extending to the upper critical point[145]. A recent study[146] has raised the possibility that the peak in measured magnetization H_p marks an additional transition from a disordered glass to a highly disordered entangled phase. This peak line also appears to approach H_{ucp}. Thus the upper critical point may in fact be a multicritical point where the liquid, lattice and glass phase merge.

The positions of both the upper and lower critical points can be altered by the controlled introduction of point-like defects, created by oxygen vacancies, proton irradiation, and electron irradiation, as well as by columnar defects produced by heavy-ion irradiation. In the last chapter, I presented data on a single crystal where the first order melting transition was suppressed completely and replaced by a continuous Bose glass transition due to columnar defect pinning sites within the sample. In this chapter, the *evolution* of the melting line from first to second order is investigated via the introduction of low densities of columnar defects. Data is presented on crystals irradiated with 1.4 GeV Pb ions, to dose matching fields of 50 Gauss (Pb50G), 100 Gauss (Pb100G), 500 Gauss (Pb500G), and 0.1 Tesla (Pb0.1T)[147]. These results are compared with YBCO crystals irradiated with protons and electrons where the major defects are point-like[148].

9.2 Low densities of columnar defects

The samples studied were prepared in the same manner as previously described in Chapter 8. Each sample, (except Pb0.1) was precharacterized before irradiation to allow for comparative studies of the same crystal before and after irradiation. An unirradiated crystal was also kept as a reference sample for general comparisons.

Figure 9.2(a) shows the tail of the resistivity vs. temperature data for Pb50G at H=2 Tesla. Here the squared ratio of the defect spacing to the vortex spacing is $H/B_\Phi = 400$. At high fields the kink in the resistivity associated with the

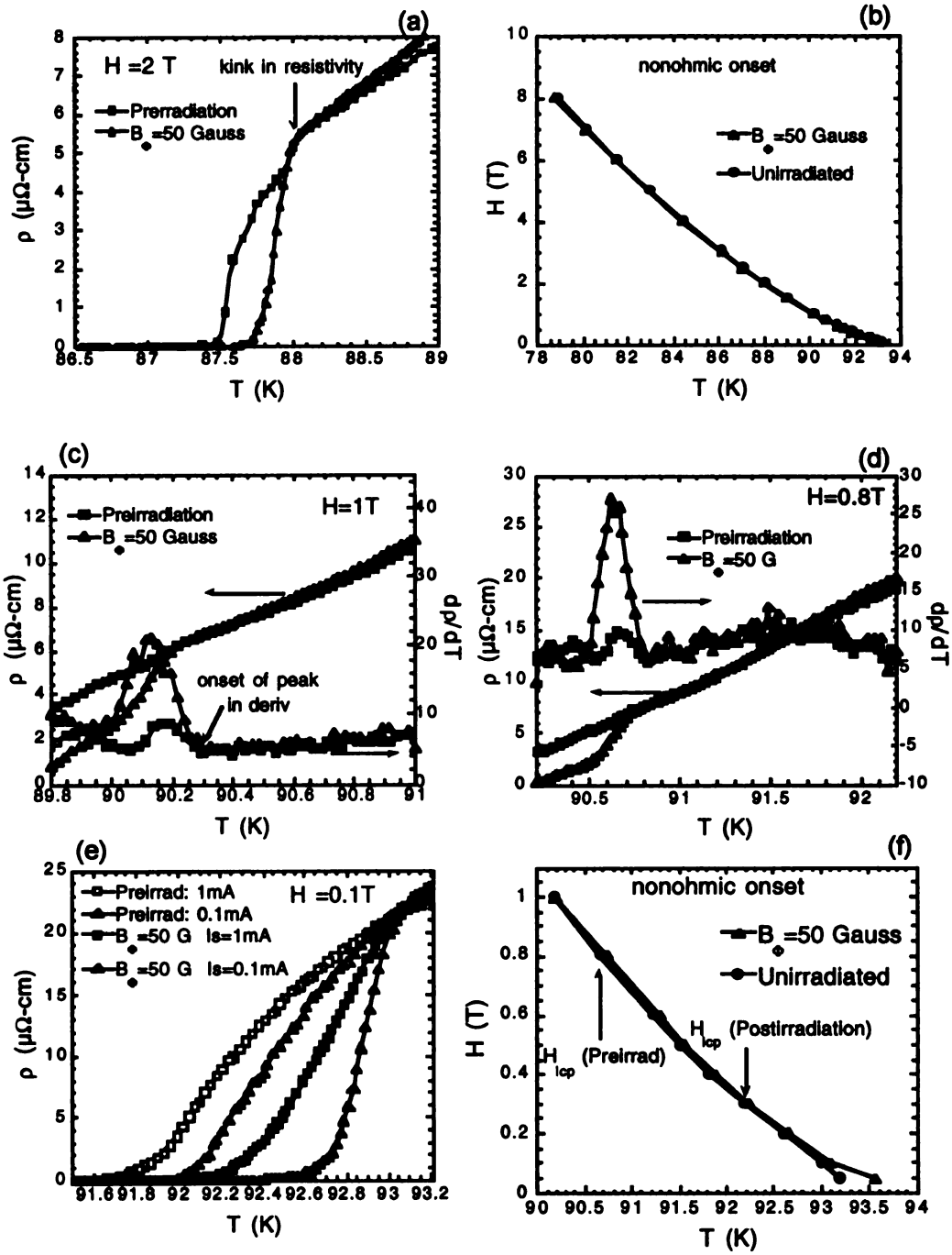

Figure 9.2 Data for preirradiation and for B_Φ=50Gauss.

first order melting transition is observed in both the unirradiated and the irradiated sample. Note that while the position of the kink has remained unchanged, the resistive drop has sharpened for the irradiated sample. Figure 9.2(b) shows that the resultant first order melting transition lines for the unirradiated and irradiated sample, determined from the temperature of the onset of non-ohmic behavior, which coincides with the temperature of the onset of the resistive 'kink', lie virtually on top of one another.

The kink in the temperature dependence of the resistivity can be tracked down to H≈0.8-1T (Figure 9.2(c) and (d)) in the unirradiated sample and defines the pre-irradiation lower critical point H_{lcp}. After irradiation the kink can be tracked down to lower fields, with H_{lcp}(Pb50G) = 0.3T, thus establishing a lower H_{lcp} after irradiation. This is quite surprising, and at first sight would suggest that irradiation actually improves the quality of the crystal by maintaining the vortex lattice state to lower fields and higher temperatures. However, transport measurements are non-equilibrium measurements. The 'kink' in the resistivity which is associated with the first order melting transition will only be observable if the current density used to measure the resistivity is lower than the critical current of the sample. If the measuring current is greater than the critical current at the melting temperature, a finite resistivity will be recorded at the position of the melting temperature due to flux flow. This could explain the decrease in the lower critical point from 0.8T before irradiation to 0.3T after irradiation in sample Pb50G. If the measuring current was *above* the critical current before irradiation and *below* the 'enhanced' critical current after irradiation, the new position of the

lower critical point is a better representation of the true lower critical point of the crystal. In other words, the introduction of a minute number of columnar disorder is able to increase the critical current of the crystal by 'carpet tacking' a few vortices.

Although the first order transition is recovered above the lower critical point, vortex pinning and hence the critical current is dramatically altered by the columnar defects. Current-voltage (*E-J*) curves before (a) and after (b) irradiation for Pb50G are plotted in Figure 9.3 for an applied field of 1T. The *E-J* curves display ohmic behavior above the melting temperature T_{melt}=90.0K. Before irradiation, non-ohmic behavior is measured within an 11 K-wide temperature range, but after irradiation this range has decreased to a mere 1.2 K, establishing strong pinning just below the melting transition for the irradiated crystal. This sharp increase in pinning after irradiation can be illustrated by comparing the critical current density vs. temperature, shown in Figure 9.3(c) where the critical current density is defined by the onset of measurable voltage, E = 10^{-6} V/cm. The fact that the critical currents are significantly shifted to higher values for fields as high as 2T for a B_Φ of only 50 Gauss is a measure of the remarkable pinning ability of the defects once the vortex solid state is established. Combining this with the fact that the first order vortex solid to liquid transition exists above H_{lcp} after irradiation demonstrates that the vortices are pinned elastically, without compromising the periodicity of the lattice.

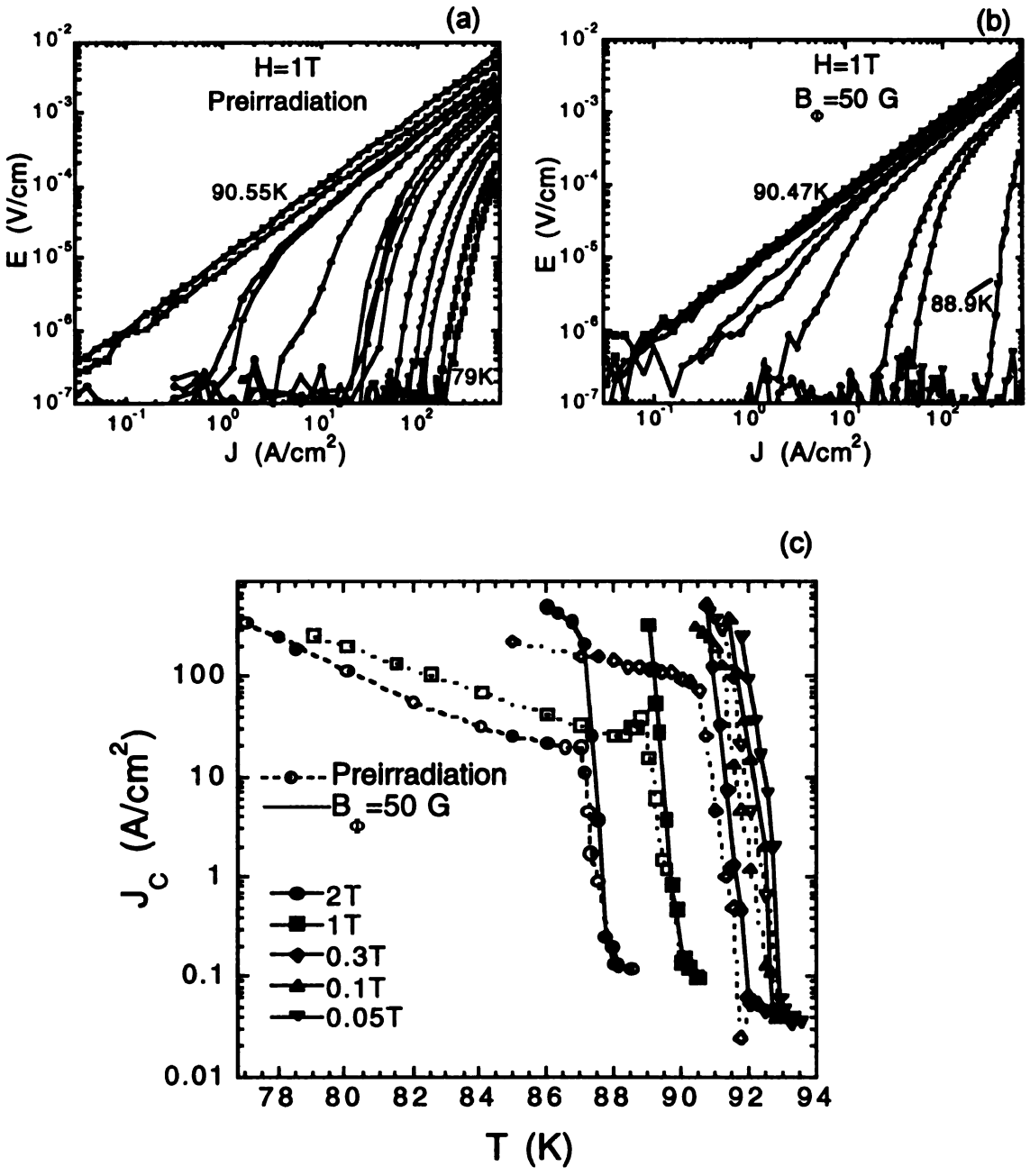

Figure 9.3 E-J curves for (a) pre- and (b) post-irradiation, H=1T>H_{lcp}. (c) Dramatic increase in j_c after low dose irradiation, here shown as a semi-log plot.

Below the lower critical point of 0.3T, no 'kink' in the resistivity is observed as shown in Figure 9.2(e). A comparison of the resistivity curves before and after irradiation measured at two different currents show an upward shift in the zero resistivity temperature after irradiation. Although the resistivity curves are monotonic and no vestige of a 'kink' associated with the first order melting transition is observed, the curves display non-ohmic behavior at a resistivity value approximately $\rho_{non\text{-}ohmic}/\rho_n$ = 90%, near the onset of the superconducting transition. Moreover, the resistive drop is significantly sharper for the irradiated sample. The irreversibility line near the lower critical point defined by the onset of non-ohmic behavior near the lower critical point is shown in Figure 9.2(f). Below 0.3T the irreversibility line for Pb50G shifts to higher temperatures, thus showing the enhancement of the solid phase due to the columnar defects.

Similar behavior is observed for the Pb100G crystal as presented in Figure 9.4. For this crystal the lower critical point is observed at the same field, H_{lcp}(preirrad) = H_{lcp}(Pb100G) = 0.3T. Figures 9.4(a) and (b) show data above and below H_{lcp} for both the irradiated and unirradiated case. In (a) a sharp peak in the derivative in the resistivity is clearly seen, while in (b) at H = 0.1T, the kink disappears in both data sets. Plotted in Figure 9.4(c) is H_{irr} at fields less than 1 Tesla, again obtained from the onset of non-ohmic behavior. Similar to Pb50G, the irreversibility line after irradiation lies above the pre-irradiation first order melting line below the lower critical point. At still higher matching fields, the lower critical point shifts up significantly. Plotted in Figure 9.4(d) is the phase diagram obtained for Pb500G. Here, the lower critical point shifts up to H_{lcp}=1.5T, and the

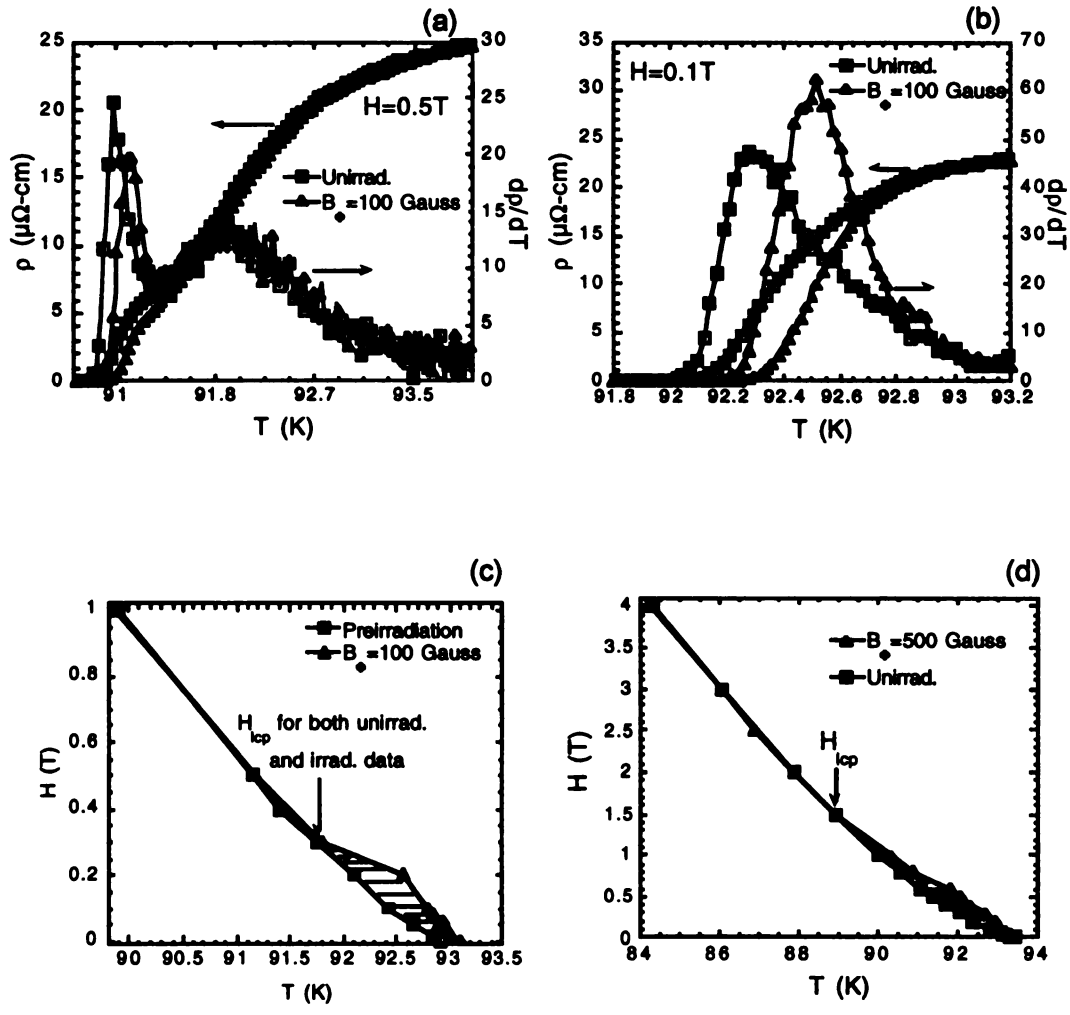

Figure 9.4 (a) Kink associated with the first order melting transition. (b) Low field, continuous transition, for H=0.1T. (c) Resultant phase diagram, for both pre- and post-irradiation, B_Φ=100 Gauss. (d) Phase diagram for crystal irradiated to B_Φ=500 Gauss.

irreversibility line is enhanced over the pre-irradiation first order melting line below the lower critical point. Finally, for Pb0.1, irradiated to a dose matching field of B_Φ = 0.1T, the lower critical point increases to H_{lcp} = 4T.

In order to investigate the transition below H_{lcp} in the presence of columnar defects, current-voltage measurements were taken at constant temperature for crystals Pb500G and Pb0.1 in an applied field of 1T, see Figure 9.5. This data can be scaled using the Bose glass theory, with values for ν and z close to those found from the Pb1 analysis in Chapter 8 as shown in the inset of the two figures. This provides evidence that below the lower critical point the vortices freeze via a continuous Bose glass transition. Further confirmation is found by evaluating the Bose glass irreversibility line as a function of angle at an applied field below H_{lcp}, as shown in Figure 9.6. Plotted is the normalized melting temperature before irradiation, and the irreversibility temperature determined from the onset of non-ohmic behavior after irradiation, as a function of the tilt angle between the applied magnetic field and along the axis of the columnar defects. The irradiated crystal displays a cusp in the irreversibility temperature centered about the columnar defect, in agreement with the prediction of the Bose glass theory. Beyond $\theta \geq 10°$ the kink in the resistivity is recovered in the irradiated crystal and the irreversibility line transforms into a first order melting line which joins smoothly with the melting line of the pre-irradiated sample. The solid line is a fit of the angular dependence of the first order melting line to the anisotropic London formula, given by $k_B T_m = [\Phi_o c_L]/[4\pi^2 \lambda_{ab}^2 B^{1/2} \varepsilon(\theta)^{1/4}]$, where $\varepsilon(\theta) = \gamma^2 \cos^2(\theta) + \sin^2(\theta)$, and γ is the superconducting mass anisotropy. The fit

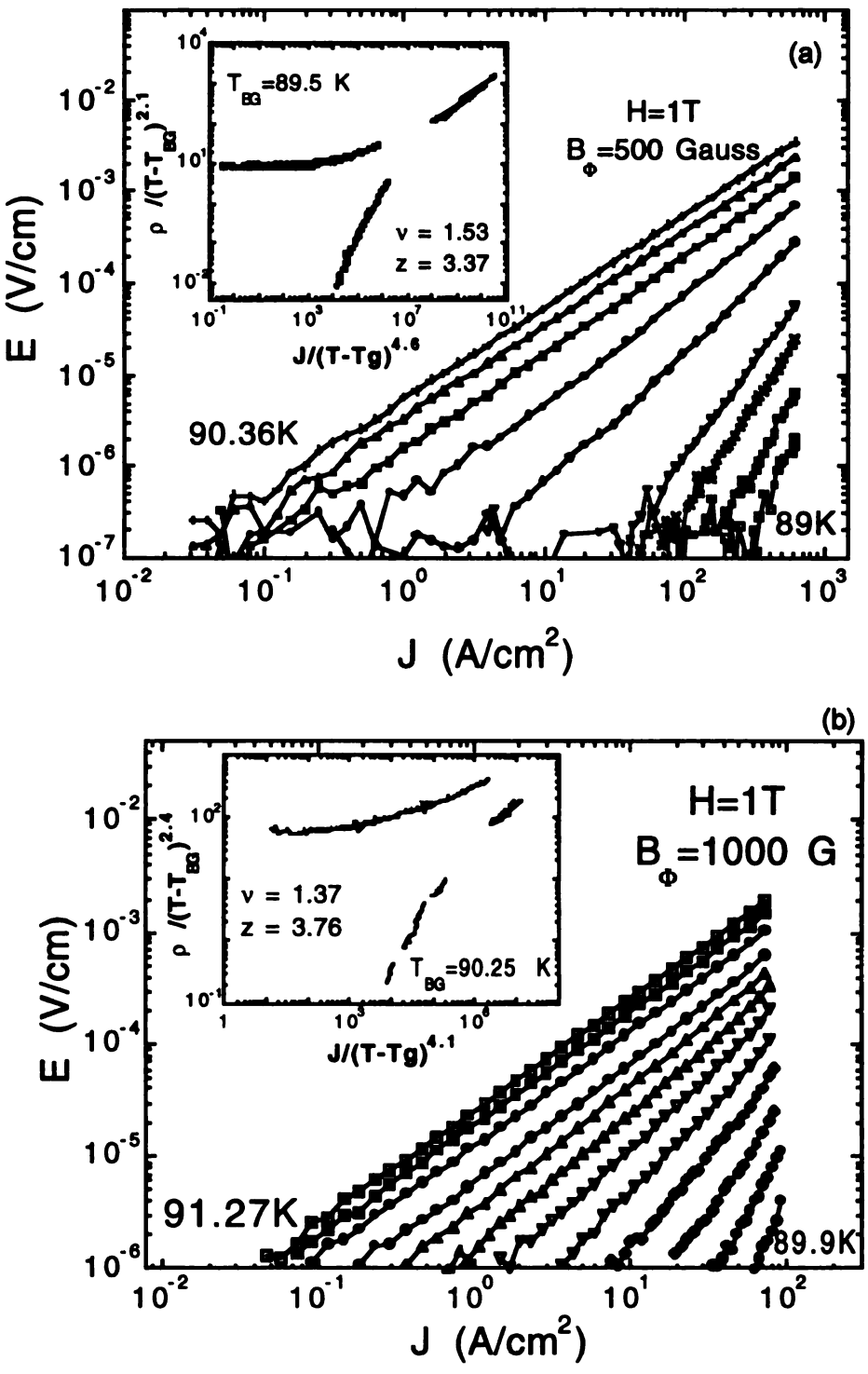

Figure 9.5 (a) E-J curves for (a) Pb500G and (b) Pb0.1T. The insets show the scaling of these curves to the Bose glass theory.

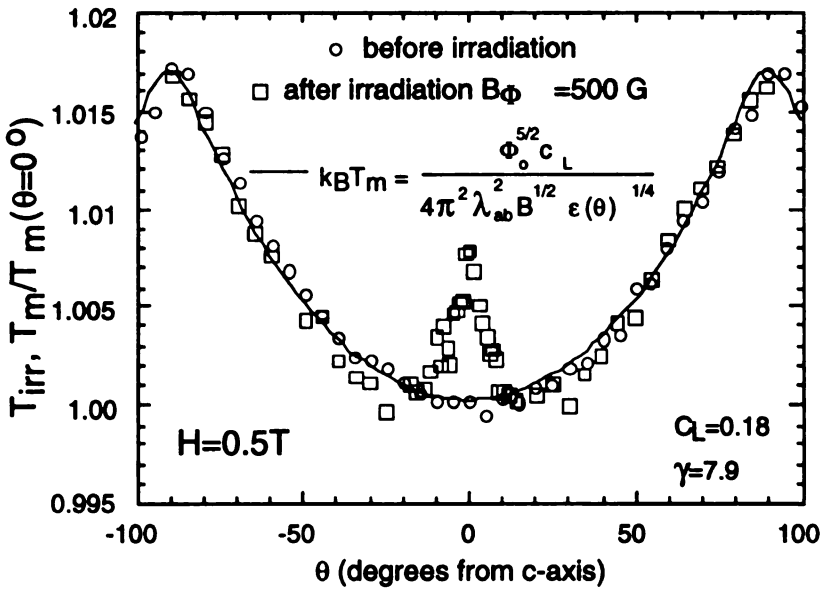

Figure 9.6 Angular dependence of the melting transition before irradiation, and of the irreversibility line after irradiation.

yields a Lindemann criterion number of $c_L = 0.18$ and a mass anisotropy of $\gamma = 7.9$, in good agreement with previous measurements on untwinned YBCO single crystals[32]. Thus, by increasing the tilt angle of the magnetic field with the columnar defects, the effective pinning strength of the defects is sufficiently weakened as to reestablish the first order melting transition. Our results clearly demonstrate that the vortex solid below the irreversibility line is a Bose glass.

The data from Pb50, Pb100, Pb500 and Pb0.1T demonstrate that the first order melting transition is recovered when the applied magnetic field is above 30–60B_Φ, corresponding to ~6-8 vortices between two given columnar defects. This is in qualitative agreement with the data from Pb1 (B_Φ = 1T), where by extrapolating the pre-irradiation first order melting curve and the Bose glass transition curve to higher magnetic fields showed an intersection at a field of 26T.

Our results suggest that the lower critical point is a vortex pinning saturation point. At low fields, the vortex interaction energy is less than the vortex pinning energy, resulting in the randomizing of the vortex structure due to columnar defect pinning (loss of long range translational and orientational order), leading to a Bose glass state. With increasing field, the density of vortices increases. At the lower critical point, the vortex interaction energy becomes greater than the pinning energy and the vortex lattice is recovered, along with the first order solid to liquid transition.

The phase diagram for the four irradiated crystals also shows the evolution of the first order melting line to a Bose glass line. This occurs through a shift in the lower critical point to higher temperatures, and with a corresponding shift of the irreversibility line below the lower critical point to higher temperatures. The increasing shift in the irreversibility line with dose is in agreement with the measurements on crystals U1, U2, U4, and Pb1 and confirms that the defects not only change the nature of the transition, but also act to stabilize the vortex solid phase. The enlargement of the vortex solid regime is shown by the cross-hatched areas in Figure. 9.4(c) and Figure 9.4(d).

The vortex motion in the liquid state is also retarded by the introduction of columnar defects. This is seen in Figure 9.7, where the normalized resistivity is plotted for Pb100G, Pb500G, and Pb0.1. For Pb0.1 the temperature is also normalized since the transition temperature shifts down slightly after irradiation. While there is virtually no difference between the unirradiated and irradiated data sets for Pb100G, there is significant lowering of the resistivity above the melting

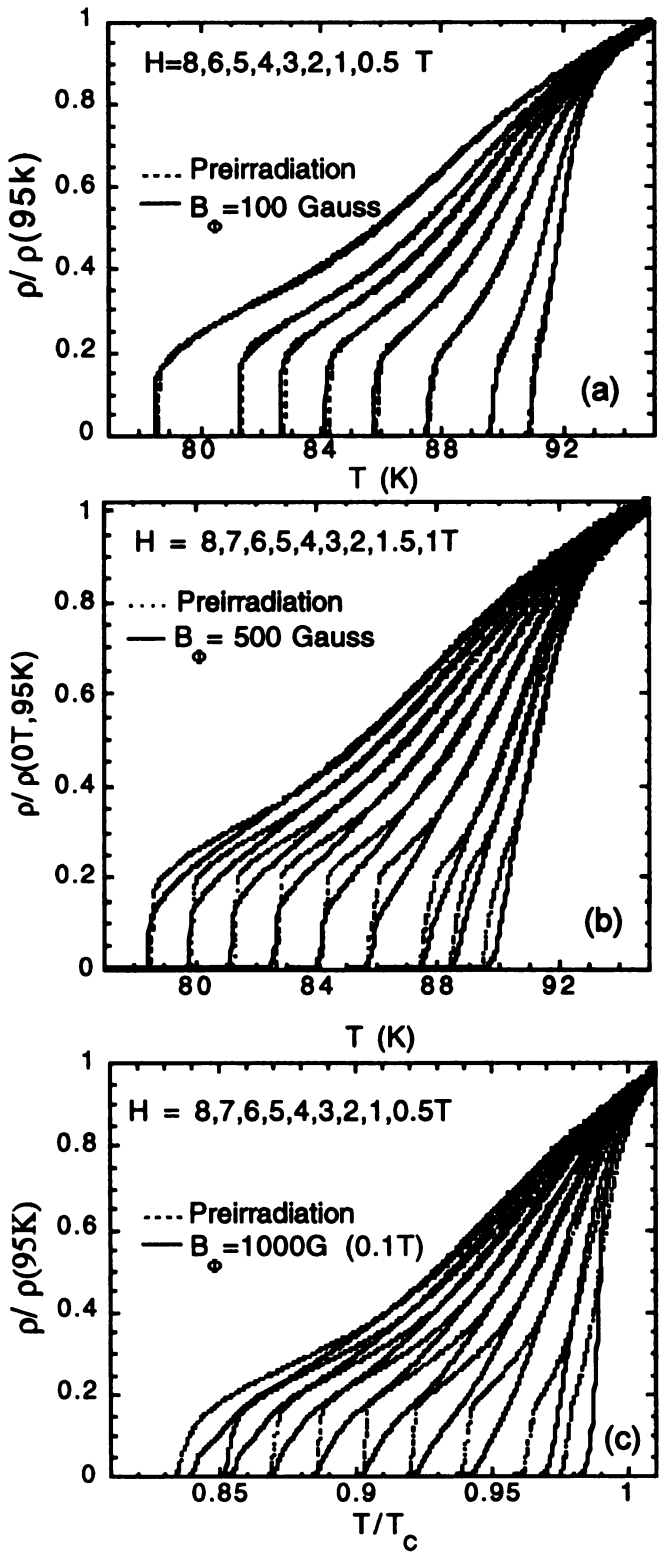

Figure 9.7 Normalized resistivity versus temperature for (a) 100 G, (b) 500 G, and (c) 1000 G. For (a) and (b) the data compares pre- and post-irradiation on the same sample. In (c) the 1000 G data is compared to a reference sample.

temperature for the other two crystals irradiated at a higher dose. This can be attributed to an increase in the viscosity of the vortex liquid due to a retardation of the vortex velocity from pinning in the liquid state[75, 149]. If the healing length for vortex flow originating from one pinning site as described in Chapter 5 is cut off by another nearby columnar defect, the vortex velocity in the liquid can be greatly retarded.

The crystals were also investigated at high fields at the National High Magnetic Field Laboratory at Tallahassee, Florida. Shown in Figure 9.8 is the temperature derivative of the resistivity for Pb0.1 (upper inset) and a comparison with the reference crystal at 10T (lower inset). The vortex melting lines for these two crystals are shown in the main figure, obtained from the peak in the temperature derivative of the resistivity. As noted previously, the lower critical point for Pb0.1 shifts up to H_{lcp} = 4T, and for fields below this field the irreversibility line of the irradiated crystal is shifted to higher temperatures. For the reference crystal, the kink associated with first order vortex melting is detected up to H_{ucp} = 9T, but after irradiation the kink is observed up to H_{ucp} = 11T. These are the first measurements which show an increase in the upper critical point as a result of imbedding columnar defects within the sample. The upper critical point marks the transformation of the first order vortex melting line into a higher order transition. This transformation is speculated to occur due to increased fluctuation of the vortex lines at high magnetic fields brought upon by increased pinning of weak random point defects. Previous measurements on twinned and untwinned crystals[49] have provided evidence that for fields above

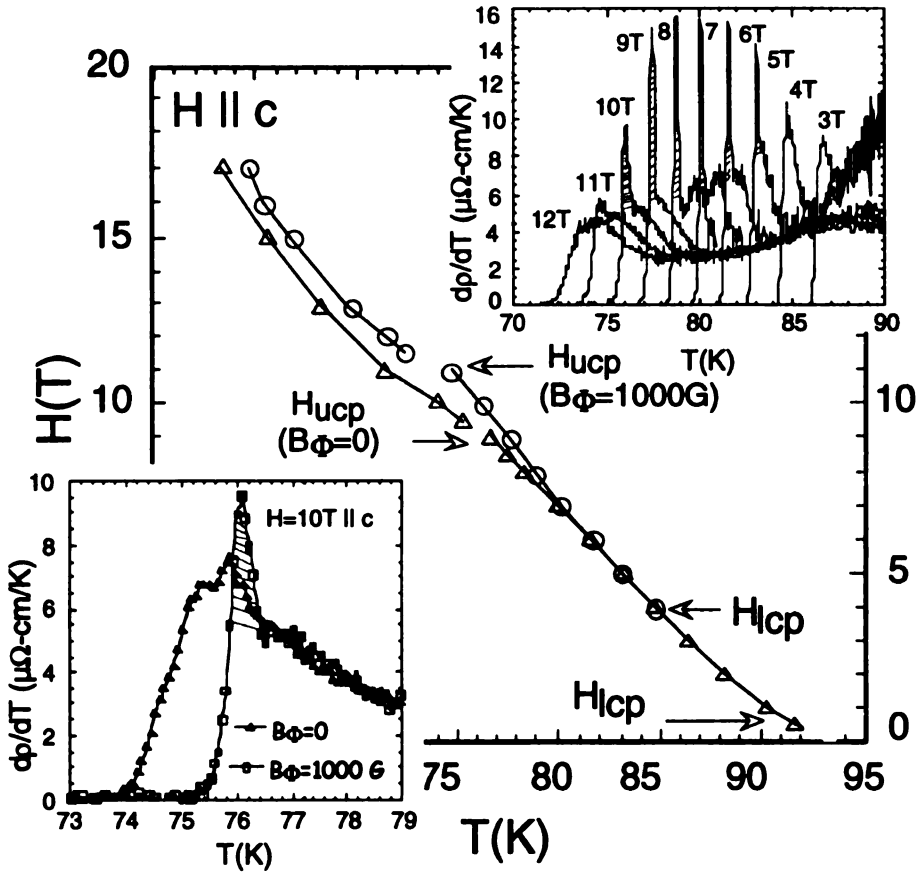

Figure 9.8 H-T diagram for crystal PB0.1T, where both the unirradiated (circles) and irradiated (triangles) crystal melting transition lines are shown. The upper inset shows the derivative of the resistivity dρ/dT versus T after irradiation. The lower inset compares dρ/dT unirradiated (triangles) and irradiated data (squares) for H=10T, with a peak in the data after irradiation.

H_{ucp} the vortices become entangled, due to meandering of the vortex lines promoted by the presence of point defects. Figure 9.8 demonstrates that the columnar defects can inhibit line wandering of the vortex line by pinning the vortex along its entire length. Consequently, the vortices remain unentangled, and thus the vortex lattice structure is preserved to even higher fields, resulting in an upward shift of the critical point. Also plotted in fig. 9.8 above H_{ucp} are the T_{zero} lines, defined where the resistivity goes to zero, using a $\rho = 0.01\mu\Omega$-cm

criterion. As a result of the increase in H_{ucp}, this solid-liquid transition line above H_{ucp} is also shifted to higher temperatures and fields after irradiation.

9.3 Comparison with low densities of point defects

The effect of low density of point defects induced by proton irradiation on untwinned $YBa_2Cu_3O_{7-\delta}$ has been investigated[148]. A clean, untwinned YBCO crystal, with dimensions 880(l)x440(w)x40(t) μm^3, was irradiated with 9 MeV protons at the tandem accelerator at Western Michigan University (WMU). Transport measurements were performed using the standard four-probe technique, with the current directed along the ab-plane of the crystal. The crystal was first pre-characterized and then sent to WMU for proton irradiation. Successive irradiations and characterization with transport measurements were performed on the same sample, with total doses amounting to 0.25, 0.5, 1.0, 1.5, and $2.0x10^{15}$ protons/cm^2. The irradiation produced random point-like defect sites, with diameters <20 Å in addition to cluster defects ~30 Å in diameter. The created defects are isotropic in nature without any apparent correlation along the irradiation direction. It is estimated[148] that the resultant defect densities are approximately one defect per ~29000 unit cells for $0.25x10^{15}$ p/cm^2 dose, increasing to one defect per ~3600 for $2x10^{15}$ p/cm^2, corresponding to defect separations from 175 Å for the lowest dose, to 85 Å for the highest dose. Room temperature annealing of ~30% of the oxygen defects has been taken into account in this calculation. As was the case for low dose columnar defects, successive proton irradiations at these low doses have virtually no effect on the

zero field transition temperature T_c, with only about ~6% increase in the normal state resistivity for the highest dose.

The unirradiated crystal for this study displayed a zero-field transition temperature of T_c = 92.8 K, with a transition width ΔT_c< 300 mK. Similar to our previous YBCO reference crystals, the unirradiated sample showed a sharp kink in the resistivity measurements associated with the first order melting transition, in fields of 0.05–8T, the maximum field of our measurement. Figure 9.9 shows resistivity measurements for H = 4T applied parallel to the c-axis, for an applied current density of 6 A/cm^2 in the ab-plane of the crystal. Fig. 9.9(a) shows an expanded view of the melting transition after each subsequent proton irradiation; the inset shows the full data up to 95 K. Above the transition the resistivity clearly decreases with increasing dose. The figure also shows a lowering of the melting transition temperature with increasing dose, the position of which is tracked by the onset of the peak in the temperature derivative of the resistivity, see Fig. 9.9(b). The onset of the peak clearly shifts down with increasing dose. The height of the peak also decreases with dose, and for doses of 1.5 and 2.0x10^{15} p/cm^2, a peak is no longer discernable. However no broadening of the temperature width of the transition is observed[148].

In Figure 9.10(a) the derivative of the resistivity data is shown for H = 3–8T, for a dose of 1.5x10^{15} p/cm^2. While a peak in the derivative is observed for H = 4–7T (shown as hatched in the figure), the peak has disappeared above and below these fields, establishing an upper critical point of H_{ucp} = 7T and a lower critical point of H_{lcp} = 4T. For a dose of 1.0x10^{15} p/cm^2, the

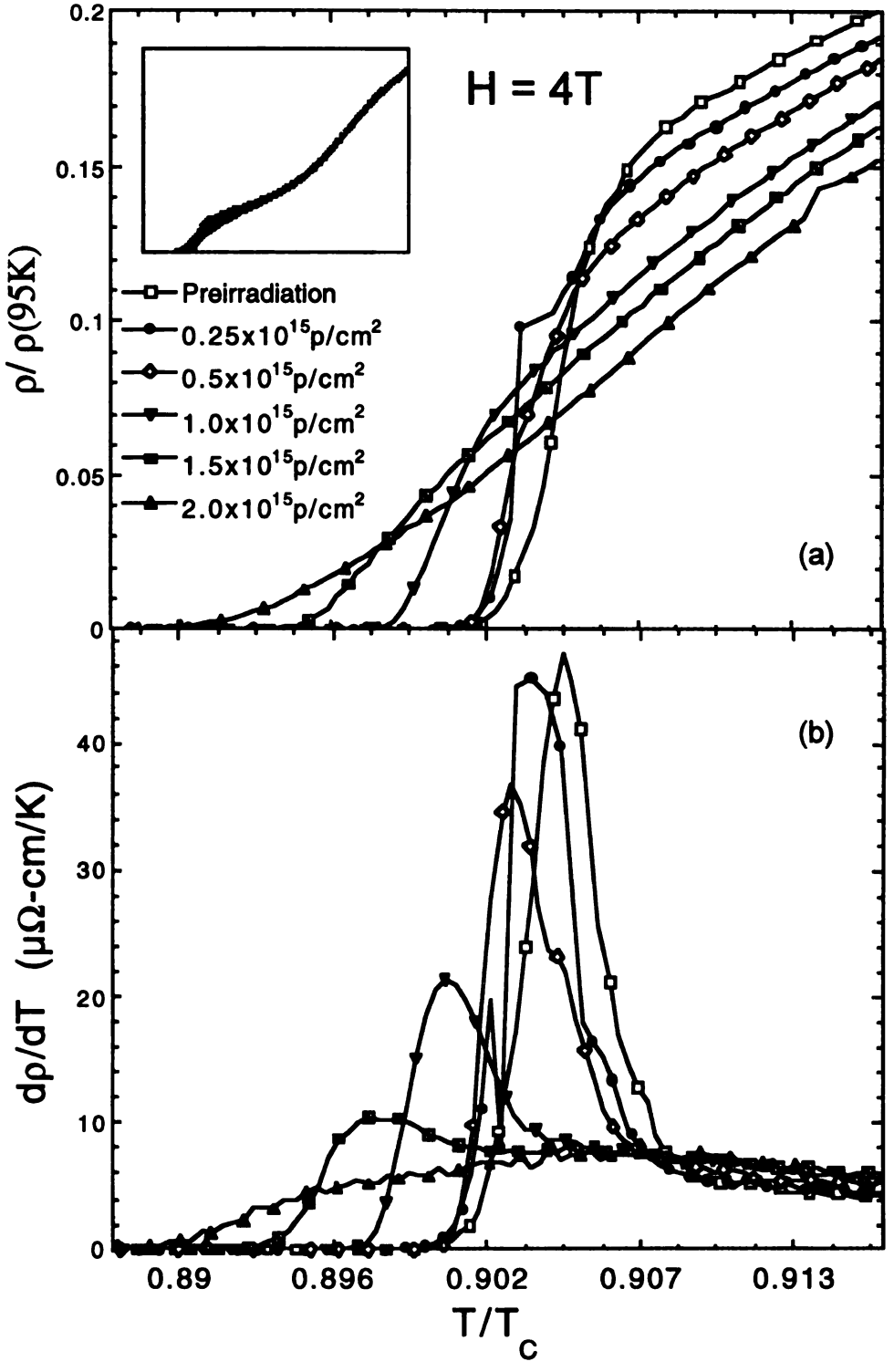

Figure 9.9 (a) Resistivity versus temperature for H=4T, here shown after successive proton irradiations. (b) The derivative of the resistivity data, showing a peak at all but the highest dose.

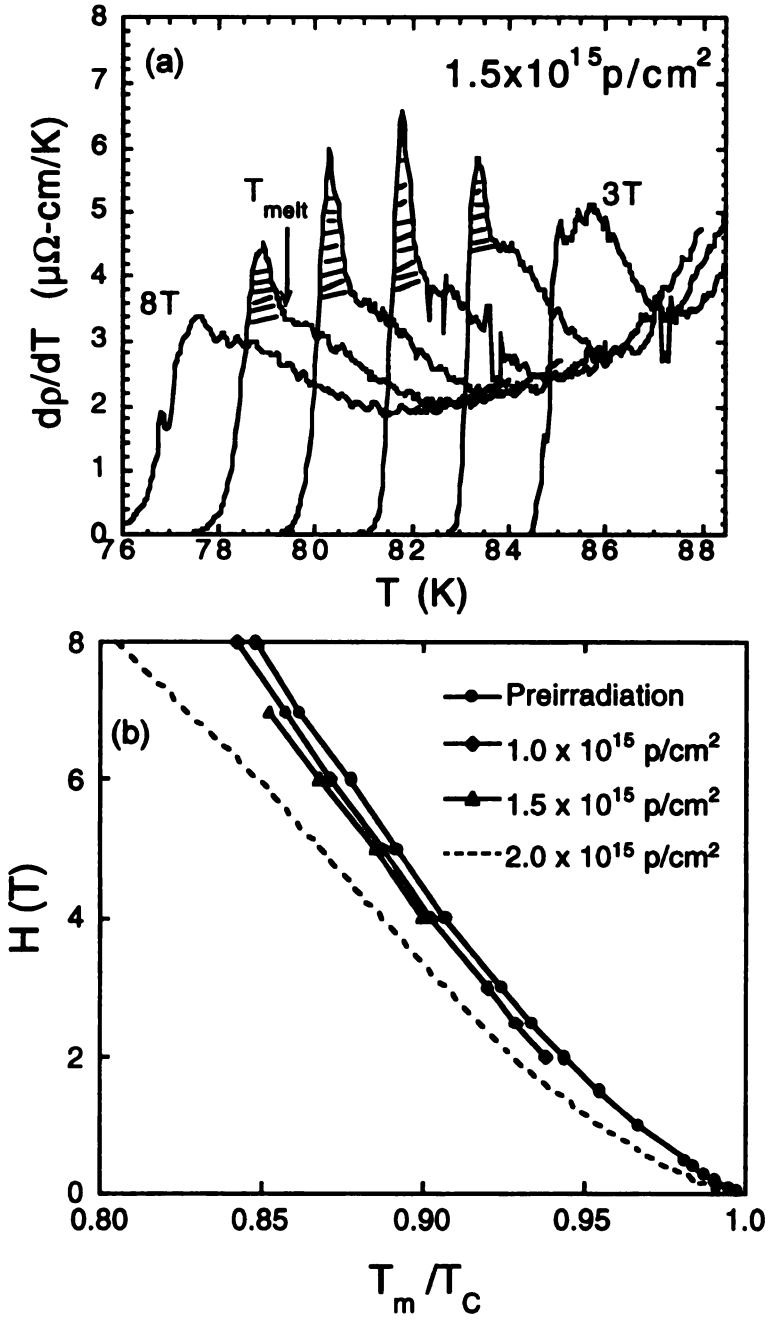

Figure 9.10 (a) Plot showing the derivative of the resisitivity for a dose of $1.5x10^{15}p/cm^2$, for H=3,4,5,6,7, and 8T. A peak in the derivative is seen for H=4-7T, shown as hatched in the figure. (b) Phase transition lines for the proton irradiation. For the preirradiation, 1.0, and $1.5x10^{15}p/cm^2$ data, the lines show the first order melting, defined by the onset of the kink in the resistivity data. The dashed line shows a resistivity criterion for the $2x10^{15}p/cm^2$ dose.

upper critical point is above H = 8T, in agreement with previous measurements on an untwinned crystal[150], which found that for the same dose the upper critical point was observed at 9T, lowered from an unirradiated value of 12.5T.

Figure 9.10(b) shows the resultant vortex phase diagram. The first order melting transition is shifted downward in temperature, and there is an upward shift in H_{lcp} and a downward shift in H_{ucp} with increasing dose. At a dose of $2x10^{15}$ p/cm^2 the critical points have converged and no first order transition is seen; for this dose the T_{zero} (ρ = 0.01μΩ-cm criterion) line is shown. The behavior of H_{ucp} with defect density agrees with other measurements of YBCO samples in which point defects were produced by oxygen vacancies, created by lowering the oxygen concentration[52, 53, 71]. The H_{ucp} point in an electron irradiated crystal was also investigated by coworkers[148]. In that work H_{ucp} was observed to increase via the lowering of the defect density through successive heat treatments of the sample, which is consistent with our proton irradiation results. For the electron irradiation, the strong defect sites were presumed to be point-like vacancies in the Cu-O planes[151], with the heat treatments acting to gradually anneal out the defects.

The lowering of the melting transition at high defect densities has been observed previously in proton[81, 82] and electron[16] irradiated YBCO crystals. A very recent study[145] of an electron irradiated crystal has confirmed the lowering of H_{ucp} and the first order melting line, as well as a shift to lower fields of the 'enhanced pinning line' H^* with increasing defect density, sketched in Figure 9.11, upper plot. The downward shift in H^* as well as in the magnetization

peak H_p as a function of increased oxygen vacancies has also been confirmed[53, 144].

Whereas the proton-created defects induced shifts in both upper and lower critical points, this is not the case for electrons, leading to a possible explanation based on the difference in defect production for the two cases[148]: While protons produce both large cluster defects as well as smaller vacancies, TEM studies[151] show that electrons produce random defects less than 20 Å in diameter, without creating the larger clustered defects. Since both ions act to lower H_{ucp}, we speculate that the smaller point-like defects are responsible for vortex disorder at these higher fields, possibly by promoting line meandering leading to entanglement. The fact that H_{ucp} can also be lowered by increasing the density of oxygen vacancies supports this view. The behavior of H_{lcp} however is controlled by the larger cluster defects, which may act as stronger pinning sites as compared to electrons. Previous magnetization measurements[151] show stronger pinning strength for proton versus electron irradiated YBCO samples. The cluster defects are able to pin the vortex lines at low vortex densities and high temperatures, possibly resulting in an unentangled vortex glass below the lower critical point: At these low fields the intervortex distance is much larger than (>3x) the defect spacing, which may lead to individual vortex pinning. With increasing dose more cluster defects are created which can pin more vortex lines, and thus the lower critical point shifts upward with dose.

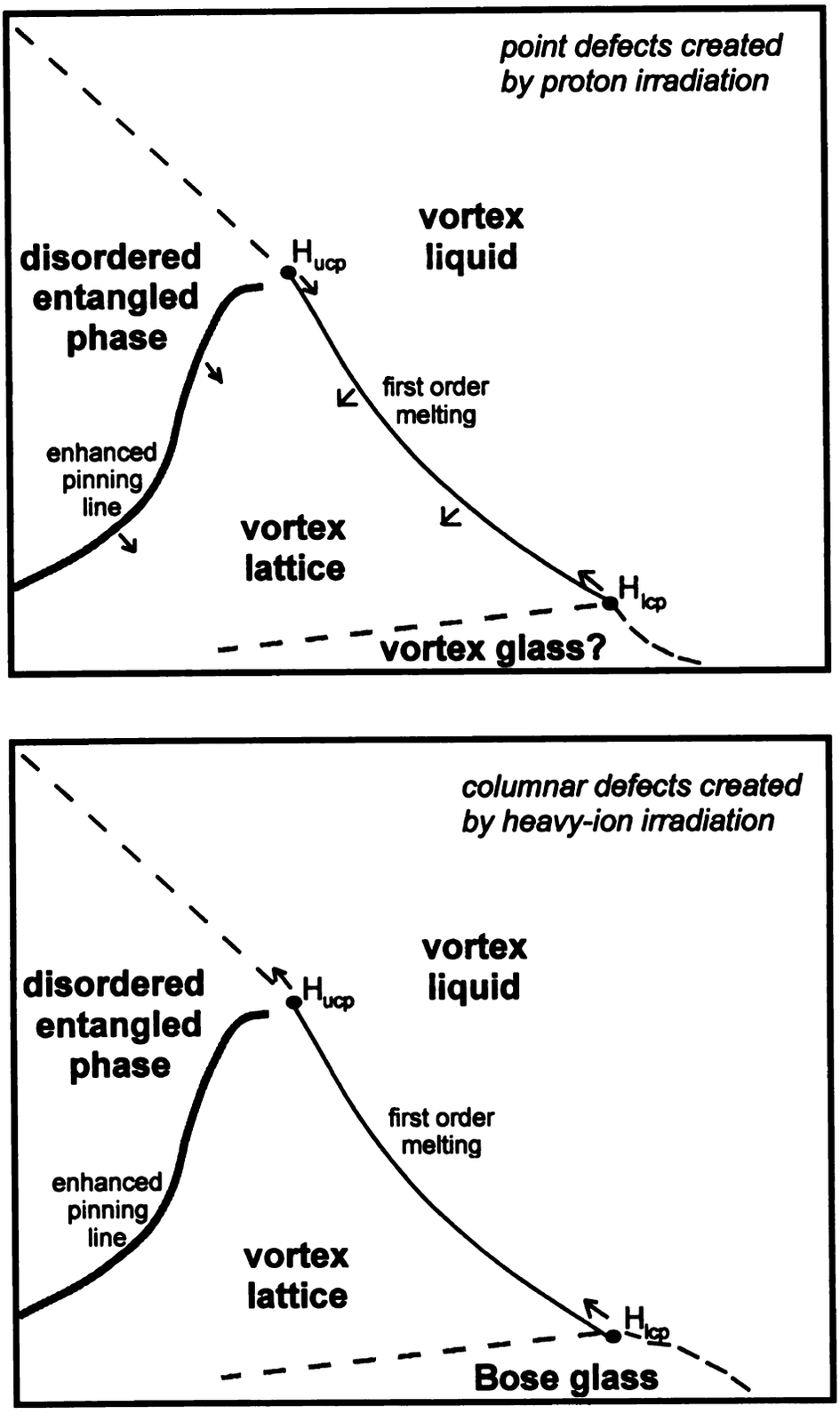

Figure 9.11 The effect of (a) point defects and (b) columnar defects on the vortex phase diagram of YBCO.

As discussed earlier, it is theorized that the peak effect measured in unirradiated YBCO crystals just below the melting transition was possibly due to a disordered phase, which lies just between the liquid and solid states[50, 67, 68], and extends up into the disordered solid phase above the enhanced pinning line. In this scenario, the magnetization peak line H_p meets the transport critical current peak in J_c below the upper critical point, and the upper critical point would not be a multicritical point. Recent magnetization data[143] on YBCO crystals irradiated with electrons appears to show a disassociation between H_{ucp} and the peak line, lending some support to this idea. While the resistivity data on crystals irradiated with low doses of columnar defects show a complete suppression of the peak effect, this is not the case for the low dose proton irradiation data. Shown in Figure 9.12 is *E-J* measurements for H = 2T. A clear transition from linear to negative curvature of the *E-J* temperature curves can be seen in (a) the pre-irradiation curves and (b) the 0.5×10^{15} p/cm^2 dose curves. At the highest dose no transition is seen and the curves all show ohmic behavior (fig. 9.12(c)). Plotted in fig. 9.12(d) is j_c vs. T/T_c, where j_c is defined by an E = 10^{-6} V/cm criterion; in fig. 9.12(e) it is replotted in semilog. The sharp jump in j_c (clearly seen in fig. 9.12(e)) for the unirradiated crystal and for the first two proton doses reflects the first order vortex lattice freezing transition where a non-zero shear modulus first appears in the vortex solid state. The j_c line increases above the jump, indicating *enhanced* pinning, which would be expected for point pins in a disordered vortex phase. Once the first order melting transition is suppressed (at a dose of 1×10^{15} p/cm^2 for H = 2T), then the curves shift downward with

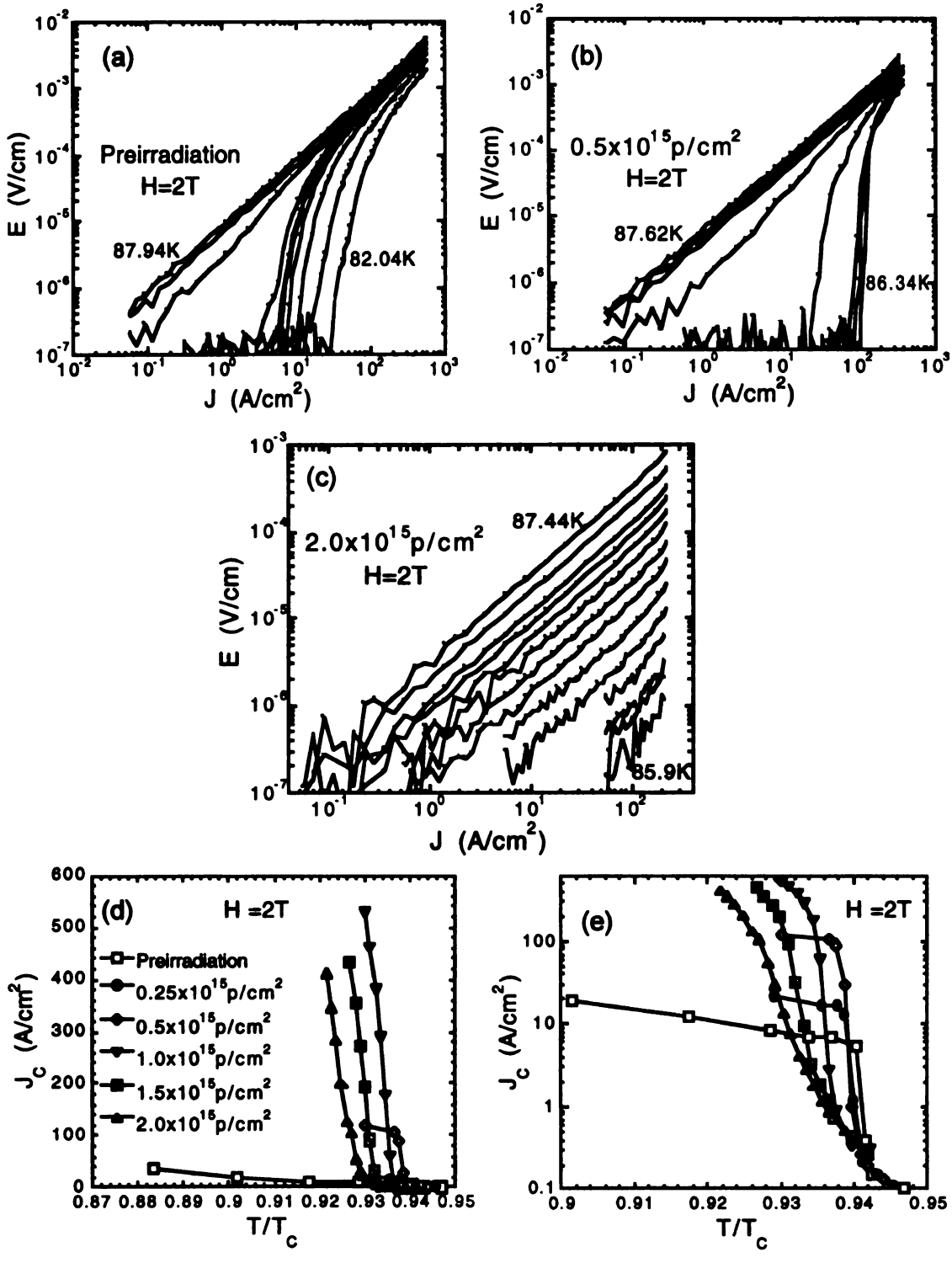

Figure 9.12 (a)-(c) E-J curves, as a function of proton irradiation dose. (d), (e) Critical current density versus temperature as a function of proton irradiation dose.

increasing dose. This reflects the downward shift in temperature of the solid state with increasing point defects, as seen in the vortex phase diagram (fig. 9.10(b)). The ability of the point defects to destabilize the solid state, due to the enhanced vortex wandering induced by the random defect sites, is in direct contrast with columnar pinning sites, which tend to stabilize the solid state and shift the transition line to higher temperatures and fields.

For the case of point defects, a vortex glass has been predicted[22, 29], in which a non-ohmic critical fluctuation regime is expected near the transition. However, looking at fields below the lower critical point, no feature of a liquid to solid transition was seen in the current-voltage curves (see Figure 9.12(c)), and thus the data presumably reflects only the liquid state. If there is a vortex glass transition, it lies below our experimental resolution. Recent data on the angular dependence of the ohmic tail of the resistivity for a crystal irradiated to a higher proton dose ($3x10^{16}$ p/cm^2), does show evidence of a possible vortex glass transition in YBCO[82].

In summary, the vortex phase diagram of high temperature superconductors in the presence of disorder contain a rich variety of novel vortex phases, which evolve as the density and dimensionality of the defects are increased. The general results of low densities of point and columnar defects are summarized in Figure 9.11. For the case of point defects created by proton irradiation the upper critical point is shifted downward with increasing dose, while for a crystal with a columnar density of B_Φ = 1000G the measured H_{ucp} shifted upwards. Hence we conclude that columnar defects tend to prevent vortex line

meandering which is normally promoted by weak random point defects, resulting in an upward shift in the upper critical point. However, as discussed previously, the upper critical point in YBCO will be established at higher fields, at the point in the phase diagram where the pinning energy of the underlying point defects overcome the vortex tilt energy and the vortex line begins to meander, leading to a possible entangled vortex state.

This type of novel behavior was also seen near the lower critical point. For both types of defects, H_{lcp} is observed to shift upwards with increasing disorder, with the first order melting transition transformed into a continuous transition below H_{lcp}. This transformation occurs due to the energy balance between the pinning energy and the vortex elastic energy, specifically the vortex shear modulus energy. The pinning energy of the point-like defect clusters induced by proton irradiation, and the columnar defects created by heavy ion irradiation, both act to randomize the vortex structure. For the case of the columnar defects, a Bose glass transition was established below H_{ucp}. It is unclear as to the nature of the transition below H_{lcp} in the case of proton irradiated samples. Above H_{lcp} the first order melting transition was reestablished. This occurs when the vortex-vortex interaction energy overcomes the pinning energy, restoring the lattice state at fields above H_{lcp}. Our work implies a possible existence of a low field disorder-order transition, shown in Figure 9.11 as dashed lines just below the vortex lattice. Whether this new line is related to the H^* or H_p line determined from recent magnetization measurements remains to be seen.

Chapter 10

CONCLUSION

We have investigated the effects of defects on the vortex melting transition in YBCO single crystals. Columnar defect densities at matching fields B_Φ = 1, 2, and 4 Tesla were investigated, in applied fields up to 8 Tesla. For these high defect densities, the kink in the resistivity data associated with a first order melting transition is replaced by a monotonically decreasing function of temperature. In the presence of a density of columnar defects in which the applied field $H \sim B_\Phi$, a continuous transition to a Bose glass has been predicted. This glassy phase is characterized by vortex localization within the defects, for an applied field applied along the defect direction. The glass-to liquid transition thus represents a localization-delocalization transition of the vortex lines. This transition has been investigated within the framework of the Bose glass theory, in which a scaling ansatz for *E-J* curves is expected for temperatures within the critical fluctuation regime. The results of the irradiation confirm a continuous transition, with a scalable non-ohmic critical regime. From scaling of resistivity data the static and dynamic critical exponents ν and z were obtained, with consistent values of these exponents at fields above and below B_Φ.

Due to the anisotropic nature of the defects, the effective pinning strength of the defects can be weakened by tilting the field with respect to the defect direction, resulting in a sharp cusp in the melting transition as a function of field angle. From the Bose glass theory a lock-in transition is predicted, which

describes vortex kink proliferation resulting in a cross-over from a Bose glass to liquid, induced by rotating the vortices at large angles away from the defects. This is studied experimentally by locating the onset of a measurable resistance as a function of angle and temperature. Results from angular measurements agree with the scaling results obtained for a field applied along the defects. Thus the existence of a transition to a Bose glass state is firmly established. Finally, the defects act to shift the melting transition to higher temperatures, thereby stabilizing the vortex solid state at higher thermal fluctuations. However, for vortex line densities above the columnar defect density the Bose glass transition line begins to approach the melting transition line of the pristine sample, although the merging of these lines is expected at significantly higher fields.

The evolution of the melting line from a first order transition to a continuous transition was evaluated by introducing low densities of columnar defects into the crystals. The lower critical point is shown to shift upwards with increasing columnar defect density, with the critical point occurring at $H_{lcp} \approx 30$-$60B_{\Phi}$. For fields below H_{lcp} a Bose glass transition is experimentally confirmed. Angular measurements identify the expected cusp predicted by the Bose glass theory, as well as a crossover from a Bose glass to a vortex lattice with increasing tilt angle. For $B_{\Phi} = 1000$ Gauss, an upward shift in the upper critical field H_{ucp} is observed. Thus the vortex lattice can itself be stabilized by columnar defects. Above H_{ucp} an entangled vortex configuration has been predicted, and much experimental evidence points to this scenario. An upward shift in H_{ucp} then implies that the columnar defects act to maintain straight vortices, thereby

inhibiting vortex wandering and the production of topological defects expected for an entangled phase.

In comparison to anisotropic columnar defects, low doses of isotropic defects created by proton irradiation were investigated. The defects take the form of both point-like defects and somewhat larger cluster defects. The resultant behavior of the melting transition is quite different in this case. Both the upper and lower critical points are shifted towards one another, while the first order melting line is shifted to lower temperatures. Thus for proton irradiated samples the vortex lattice is destabilized by the defects at both low and high fields, as well as at lower temperatures. At high fields the defects are expected to produce an enhancement of vortex line wandering, and thus a lowering of the upper critical point. This is due to the random isotropic nature of the defects, which tend to tilt and deform the lattice in directions both parallel and perpendicular to the field direction. The upward shift in the lower critical point is surprising, and has not been observed in electron irradiated crystals or in crystals with varying oxygen content. In the presence of point-like defects, a possible phase transition below H_{lcp} has not yet been established.

BIBLIOGRAPHY

Bibliography

1 H. K. Onnes, Leiden Comm. **120b, 122b, 124c** (1911).

2 W. Meissner and R. Ochsenfeld, Naturwissenschaften **21**, 787 (1933).

3 F. London and H. London, Proc. Roy. Soc. (London) **A149**, 71 (1935).

4 U. Essmann and H. Träuble, Phys. Lett. **24A**, 526 (1967).

5 M. Yethiraj, H. A. Mook, G. D. Wignall, *et al.*, Phys. Rev. Lett. **70**, 857 (1993).

6 H. F. Hess, R. B. Robinson, and J. V. Waszczak, Phys. Rev. Lett. **64**, 2711 (1990).

7 V. L. Ginzburg and L. D. Landau, Zh. Eksperim. i. Teor **20**, 1064 (1950).

8 A. A. Abrikosov, Sov. Phys.æJETP **5**, 1174 (1957).

9 J. G. Bednorz and K. A. Müller, Zeitschrift fur Physik B **64**, 189 (1986).

10 M. F. Schmidt, V. E. Israeloff, and A. M. Goldman, Phys. Rev. Lett. **70**, 2162 (1993).

11 J. Bardeen and M. J. Stephen, Physical Review **140**, A1197 (1965).

12 P. H. Kes, J. Aarts, J. v. d. Berg, *et al.*, Superconductivity, Science and Technology **1**, 242 (1989).

13 V. M. Vinokur, M. V. Feigel'man, V. B. Geshkenbein, *et al.*, Phys. Rev. Lett. **65**, 259 (1990).

14 W. K. Kwok, J. Fendrich, S. Fleshler, *et al.*, Phys. Rev. Lett. **72**, 1092 (1994).

15 W. K. Kwok, J. Fendrich, U. Welp, *et al.*, Phys. Rev. Lett. **72**, 1088 (1994).

16 J. A. Fendrich, W. K. Kwok, J. Giapintzakis, *et al.*, Phys. Rev. Lett. **74**, 1210 (1995).

17 P. W. Anderson, Phys. Rev. Lett. **9**, 309 (1962).

18 Y. B. Kim, C. F. Hempstead, and A. R. Strnad, Phys. Rev. Lett. **9**, 306 (1962).

19 T. K. Worthington, E. Olsson, C. S. Nichols, *et al.*, Phys. Rev. B **43**, 10538 (1991).

20 R. H. Koch, V. Foglietti, W. J. Gallagher, *et al.*, Phys. Rev. Lett. **63**, 1511 (1989).

21 M. Charalambous, R. H. Koch, T. Masselink, *et al.*, Phys. Rev. Lett. **75**, 2578 (1995).

22 M. P. A. Fisher, Phys. Rev. Lett. **62**, 1415 (1989).

23 E. Brézin, D. R. Nelson, and A. Thiaville, Phys. Rev. B **31**, 7124 (1985).

24 F. A. Lindemann, Zeitschrift fur Physik **11**, 609 (1910).

25 D. R. Nelson and H. S. Seung, Phys. Rev. B **39**, 9153 (1989).

26 A. Houghton, R. A. Pelcovits, and A. Sudbo, Phys. Rev. B **40**, 6763 (1989).

27 L. I. Glazman and A. E. Koshelev, Phys. Rev. B **43**, 2835 (1991).

28 E. H. Brandt, Journal of Low Temperature Physics **26**, 709 (1977).

29 D. S. Fisher, M. P. A. Fisher, and D. A. Huse, Phys. Rev. B **43**, 130 (1991).

30 D. R. Nelson, Phys. Rev. Lett. **60**, 1973 (1988).

31 H. Safar, P. L. Gammel, D. A. Huse, *et al.*, Phys. Rev. Lett. **72**, 1272 (1994).

32 W. K. Kwok, S. Fleshler, U. Welp, *et al.*, Phys. Rev. Lett. **69**, 3370 (1992).

33 A. B. Pippard, Philosophical Magazine **19**, 217 (1969).

34 W. K. Kwok, J. A. Fendrich, C. J. v. d. Beek, *et al.*, Phys. Rev. Lett. **73**, 2614 (1994).

35 W. K. Kwok, J. A. Fendrich, V. M. Vinokur, *et al.*, Phys. Rev. Lett. **76**, 4596 (1996).

36 G. Blatter, M. V. Feigel'man, V. B. Geshkenbein, *et al.*, Rev. Mod. Phys. **66**, 1125 (1994).

37 D. López, E. F. Righi, G. Nieva, *et al.*, Phys. Rev. Lett. **76**, 4034 (1996).

38 R. Liang, D. A. Bonn, and W. N. Hardy, Phys. Rev. Lett. **76**, 835 (1996).

39 U. Welp, J. A. Fendrich, W. K. Kwok, *et al.*, Phys. Rev. Lett. **76**, 4809 (1996).

40 J. A. Fendrich, U. Welp, W. K. Kwok, *et al.*, Phys. Rev. Lett. **77**, 2073 (1996).

41 A. Schilling, R. A. Fisher, N. E. Phillips, *et al.*, Nature **382**, 791 (1996).

42 M. Willemin, A. Schilling, H. Keller, *et al.*, Phys. Rev. Lett. **81**, 4236 (1998).

43 A. Schilling, M. Willemin, C. Rossel, *et al.*, Phys. Rev. B **61**, 3592 (2000).

44 L. M. Paulius, J. A. Fendrich, W.-K. Kwok, *et al.*, Phys. Rev. B **56**, 913 (1997).

45 R. E. Hetzel, A. Sudbo, and D. A. Huse, Phys. Rev. Lett. **69**, 518 (1992).

46 R. Sasik and D. Stroud, Phys. Rev. Lett. **75**, 2582 (1995).

47 M. J. W. Dodgson, V. B. Geshkenbein, H. Nordborg, *et al.*, Phy. Rev. B **57**, 14498 (1998).

48 H. Safar, P. L. Gammel, D. A. Huse, *et al.*, Phys. Rev. Lett. **70**, 3800 (1993).

49 D. López, L. Krusin-Elbaum, H. Safar, *et al.*, Phys. Rev. Lett. **80**, 1070 (1998).

50 G. W. Crabtree, W. K. Kwok, U. Welp, *et al.*, in *Physics and Materials Science of Vortex States, Flux Pinning and Dynamics*, edited by R. Kossowsky and S. Bose (Kluwer Academic Publishers, Amsterdam, 1999).

51 C. Marcenat, R. Calemczuk, A. Erb, *et al.*, Physica C **282-287**, 2059 (1997).

52 K. Shibata, T. Nishizaki, T. Naito, *et al.*, Physica C **317-318**, 540 (1999).

53 K. Deligiannis, P. A. J. d. Groot, M. Oussena, *et al.*, Phys. Rev. lett. **79**, 2121 (1997).

54 V. Vinokur, B. Khaykovich, E. Zeldov, *et al.*, Physica C **295**, 209 (1998).

55 G. W. Crabtree and D. R. Nelson, Physics Today **April**, 38-45 (1997).

56 D. Ertas and D. R. Nelson, Physica C **272**, 79 (1996).

57 T. Giamarchi and P. L. Doussal, Phys. Rev. Lett. **72**, 1530 (1994).

58 T. Giamarchi and P. L. Doussal, Phys. Rev. B **52**, 1242 (1995).

59 T. Giamarchi and P. L. Doussal, Phys. Rev. B **55**, 6577 (1997).

60 J. Kierfeld and V. Vinokur, cond-mat/9909190 .

61 R. Cubitt, E. M. Forgan, G. Yang, *et al.*, Nature **365**, 407 (1993).

62 B. Khaykovich, E. Zeldov, D. Majer, *et al.*, Phys. Rev. Lett. **76**, 2555 (1996).

63 B. Khaykovich, M. Konczykowski, E. Zeldov, *et al.*, Phys. Rev. B **56**, 517 (1997).

64 T. Nishizaki, R. Naito, and N. Kobayashi, Phys. Rev. B **58**, 11169 (1998).

65 D. Giller, A. Shaulov, Y. Yeshurun, *et al.*, Phys. Rev. B **60**, 1076 (1999).

66 S. Kokkaliaris, P. A. J. d. Groot, S. N. Gordeev, *et al.*, Phys. Rev. Lett. **82**, 5116 (1999).

67 H. Küpfer, T. Wokf, C. Lessing, *et al.*, Phys. Rev. B **58**, 2886 (1998).

68 D. López and *et al.*, unpublished .

69 D. E. Farrell, J. P. Rice, and D. M. Ginsberg, Phys. Rev. Lett. **67**, 1165 (1991).

70 W. K. Kwok, U. Welp, G. W. Crabtree, *et al.*, Phys. Rev. Lett. **64**, 966 (1990).

71 M. Roulin, A. Junod, A. Erb, *et al.*, Phys. Rev. Lett. **80**, 1722 (1998).

72 A. Schilling, R. A. Fisher, N. E. Phillips, *et al.*, Phys. Rev. Lett. **78**, 4833 (1997).

73 A. K. Kienappel and M. A. Moore, *cond-mat/9804314* (1998).

74 S. Fleshler, W. K. Kwok, U. Welp, *et al.*, Phys. Rev. B **47**, 14448 (1993).

75 M. C. Marchetti and D. R. Nelson, Phys. Rev. B **42**, 9938 (1990).

76 D. López, G. Nieva, and F. d. L. Cruz, Phys. Rev. B **50**, 7219 (1994).

77 D. López, E. J. Righi, G. Nieva, *et al.*, Phys. Rev. B **53**, 8895 (1996).

78 A. Schönenberger, V. Geskenbein, and G. Blatter, Phys. Rev. Lett. **75**, 1380 (1995).

79 C. Carraro and D. S. Fisher, Phys. Rev. B **51**, 534 (1995).

80 M. A. Moore and N. K. Wilkin, Phys. Rev. B **50**, 10294 (1994).

81 W. Jiang, N.-C. Yeh, T. A. Tomgrello, *et al.*, J. Phys. Condens. Mat. **9**, 8085 (1997).

82 A. M. Petrean, L. M. Paulius, W. K. Kwok, *et al.*, accepted by Phys. Rev. Lett., *in press*.

83 C. Reichhardt, A. van Otterlo, and G. T. Zimányi, Phys. Rev. Lett. **84**, 1994 (2000).

84 L. Civale, Supercond. Sci. Technol. **10**, A11 (1997).

85 M. Konczykowski, F. Rullier-Albenque, E. R. Yacoby, *et al.*, Phys. Rev. B **44**, 7167 (1991).

86 D. R. Nelson and V. M. Vinokur, Phys. Rev. Lett. **68**, 2398 (1992).

87 D. R. Nelson and V. M. Vinokur, Phys. Rev. B **48**, 13060 (1993).

88 H. E. Stanley, *Introduction to Phase Transitions and Critical Phenomena* (Oxford Unversity Press, New York, 1971).

89 H. E. Stanley, Rev. Mod. Phys. **71**, 358 (1999).

90 M. P. A. Fisher, P. B. Weichman, B. Grinstein, *et al.*, Phys. Rev. B **40**, 546 (1989).

91 M. Wallin, E. S. Sørensen, S. M. Girvin, *et al.*, Phys. Rev. B **49**, 12115 (1994).

92 J. Lidmar and M. Wallin, *Europhys. Lett.* **47**, 494-500 (1999).

93 T. Hwa, D. R. Nelson, and V. M. Vinokur, Phys. Rev. B **48**, 1167 (1993).

94 Z. Z. Wang, J. Clayhold, and N. P. Ong, Phys. Rev. B **36**, 7222 (1987).

95 M.-H. Whangbo and C. C. Torardi, Science **249**, 1143 (1990).

96 J. Rossat-Mignod *et al.*, in *Frontiers in Solid State Sciences*, edited by L. C. Gupta and M. S. Mutani (World Scientific, Singapore, 1993), Vol. 1.

97 G. Ceder, R. McCormack, and D. Fontaine, Phys. Rev. B **44**, 2377 (1991).

98 T. B. Lindemer, J. F. Hurley, J. E. Gates, *et al.*, J. Am. Ceram. Soc. **72**, 1175 (1989).

99 L. H. Greene and B. G. Bagley, in *Physical Properties of High Temperature Superconductors*, edited by D. M. Ginsberg (World Scientific, Singapore, 1990), Vol. 2.

100 T. Siegrist, S. Sunshine *et al.*, Phys. Rev. B **35**, 7137 (1987).

101 F. Beech, S. Miraglia, A. Santoro, *et al.*, Phys. Rev. B **35**, 8778 (1987).

102 J. Jorgensen, B. W. Veal *et al.*, Phys. Rev. B **41**, 1863 (1990).

103 D. L. Kaiser, F. Holtzberg, M. F. Chisholm, *et al.*, Journal of Crystal Growth **85**, 593 (1987).

104 H. Zheng, M. Jiang, B. W. Veal, *et al.*, Physica C **301**, 147 (1998).

105 U. Welp, M. Grimsditch, H. You, *et al.*, Physica C **161**, 1 (1989).

106 H. Schmid, E. Burkhardt, B. N. Sun, *et al.*, Physica C **157**, 555 (1989).

107 U. Welp, W. K. Kwok, G. W. Crabtree, *et al.*, Phys. Rev. Lett. **62**, 1908 (1989).

108 L. Civale, A. Marwick *et al.*, Phys. Rev. Lett. **67**, 648 (1991).

109 M. Konczykowski, V. M. Vinokur, F. Rullier-Albenque, *et al.*, Physical Review B **47**, 5531 (1993).

110 T. K. Worthington, M. P. A. Fisher, D. A. Huse, *et al.*, Phys. Rev. B **46**, 11854 (1992).

111 W. Jiang, N.-C. Yeh, D. S. Reed, *et al.*, Phys. Rev. Lett. **72**, 550 (1994).

112 J. F. Ziegler, J. P. Biersack, and U. Littlemark, *The Stopping and Range of Ions in Solids* (Pergamon, New York, 1985).

113 J. F. Ziegler, *Ion Implantation Technology* (North-Holland, Amsterdam, 1992).

114 J. P. Biersack and J. F. Ziegler, http://www.research.ibm.com/ionbeams .

115 R. L. Fleischer, P. B. Price, and R. M. Walker, Journal of Applied Physics **36**, 3645 (1965).

116 J. H. O. Varley, Journal of Nuclear Energy **1**, 130-143 (1954).

117 S. A. Durrani and R. K. Bull, *Solid State Track Detection* (Pergamon, New York, 1987).

118 G. Szenes, Phys. Rev. B **54**, 12458 (1996).

119 B. Hensel, B. Roas, S. Henke, *et al.*, Phys. Rev. B **42**, 4135 (1990).

120 V. Hardy, C. Groult, M. Hervieu, *et al.*, Nuclear Instruments and Methods in Physics Research **B54**, 472 (1991).

121 R. Wheeler, M. A. Kirk, R. Brown, *et al.*, in *Materials Research Society Symposium Proceedings*, 1992), p. 683.

122 Y. Yan and M. A. Kirk, Phys. Rev. B **57**, 6152 (1998).

123 G. Schiwietz, in *NATO ASI Series B*, edited by R. A. Baragiola (Plenum Press, New York, 1993), Vol. 306, p. 197-214.

124 Shima and *et al.*, Nucl. Inst. Meth. **200**, 605 (1982).

125 R. Wheeler and M. A. Kirk, unpublished.

126 A. D. Marwick, L. Civale, L. Krusin-Elbaum, *et al.*, Nucl. Inst. Meth. Phys. Res. B **80/81**, 1143 (1993).

127 L. Krusin-Elbaum, L. Civale, G. Blatter, *et al.*, Physical Review Letters **72**, 1914 (1994).

128 Y. Yan, R. A. Doyle, A. M. Campbell, *et al.*, Phil. Mag. Lett. **73**, 299 (1996).

129 Y. Yan and M. A. Kirk, Phil. Mag. Lett. **79**, 841 (1999).

130 M. A. Kirk and Y. Yan, Micron **30**, 507 (1999).

131 H. Safar, P. L. Gammel, D. A. Huse, *et al.*, Phys. Rev. Lett. **69**, 824 (1992).

132 P. L. Gammel, L. F. Schneemeyer, and D. J. Bishop, Physical Review Letters **66**, 953 (1991).

133 W. Jiang, N.-C. Yeh, D. S. Reed, *et al.*, Physical Review B **47**, 8308 (1993).

134 S. A. Grigera, E. Morré, E. Osquiguil, *et al.*, Phys. Rev. Lett. **81**, 2348 (1998).

135 U. Welp, T. Gardiner, D. Gunter, *et al.*, Physica C **235-240**, 241 (1994).

136 M. Oussena, P. A. J. d. Groot *et al.*, Phys. Rev. B **51**, 1389 (1995).

137 A. W. Smith, H. M. Jaeger, T. F. Rosenbaum, *et al.*, Phys. Rev. B **59**, 11665 (1999).

138 A. I. Larkin and V. M. Vinokur, Phys. Rev. Lett. **75**, 4666 (1995).

139 L. Radzihovsky, Phys. Rev. Lett. **74**, 4923 (1995).

140 A. W. Smith, J. M. Jaeger, T. F. Rosenbaum, *et al.*, to be published (2000).

141 W. K. Kwok, J. A. Fendrich, S. Fleshler, *et al.*, in *Proceedings of the 7th International Workshop on Critical Currents in Superconductors*, Alpach, Austria, 1994).

142 H. Küpfer, T. Wolf, C. Lessing, *et al.*, Phys. Rev. B **58**, 2886 (1998).

143 T. Nishizaki, T. Naito, S. Okayasu, *et al.*, Phys. Rev. B **61**, 3649 (2000).

144 S. Kokkaliaris, A. A. Zhukov, P. A. J. d. Groot, *et al.*, Phys. Rev. B **61**, 3655 (2000).

145 T. Nishizaki and N. Kobayashi, Supercon. Sci. Technol. **13**, 1 (2000).

146 A. A. Zhukov, S. Kokkaliaris, P. A. J. d. Groot, *et al.*, Phys. Rev. B **61**, 886 (2000).

147 W. K. Kwok, R. J. Olsson, G. Karapetrov, *et al.*, Phys. Rev. Lett. **84**, 3706 (2000).

148 L. M. Paulius, W. K. Kwok, R. J. Olsson, *et al.*, Phys. Rev. B **61**, *in press*.

149 M. C. Marchetti and D. R. Nelson, Physica **174**, 40 (1991).

150 W. K. Kwok, L. Paulius, D. Lopez, *et al.*, Materials Science Forum **315-317**, 314 (1999).

151 J. Giapintzakis, W. C. Lee, J. P. Rice, *et al.*, Phys. Rev. B **45**, 10677 (1992).